


2015

## Performance optimization of lateral-mode thin-film piezoelectric-on-substrate resonant systems

Hedy Fatemi  
*University of Central Florida*

 Part of the [Electrical and Electronics Commons](#)  
Find similar works at: <https://stars.library.ucf.edu/etd>  
University of Central Florida Libraries <http://library.ucf.edu>

This Doctoral Dissertation (Open Access) is brought to you for free and open access by STARS. It has been accepted for inclusion in Electronic Theses and Dissertations, 2004-2019 by an authorized administrator of STARS. For more information, please contact [STARS@ucf.edu](mailto:STARS@ucf.edu).

---

### STARS Citation

Fatemi, Hedy, "Performance optimization of lateral-mode thin-film piezoelectric-on-substrate resonant systems" (2015). *Electronic Theses and Dissertations, 2004-2019*. 1367.  
<https://stars.library.ucf.edu/etd/1367>

PERFORMANCE OPTIMIZATION OF LATERAL-MODE THIN-FILM  
PIEZOELECTRIC-ON-SUBSTRATE RESONANT SYSTEMS

by

HEDY FATEMI

B.S. University of Tehran, 2009

M.S. Oklahoma State University, 2011

A dissertation submitted in partial fulfillment of the requirements  
for the degree of Doctor of Philosophy  
in the Department of Electrical Engineering and Computer Science  
in the College of Engineering and Computer Science  
at the University of Central Florida  
Orlando, Florida

Fall Term  
2015

Major Professor: Reza Abdolvand

© 2015 Hedy Fatemi

## **ABSTRACT**

The main focus of this dissertation is to characterize and improve the performance of thin-film piezoelectric-on-substrate (TPoS) lateral-mode resonators and filters. TPoS is a class of piezoelectric MEMS devices which benefits from the high coupling coefficient of the piezoelectric transduction mechanism while taking advantage of superior acoustic properties of a substrate. The use of lateral-mode TPoS designs allows for fabrication of dispersed-frequency filters on a single substrate, thus significantly reducing the size and manufacturing cost of devices. TPoS filters also offer a lower temperature coefficient of frequency, and better power handling capability compared to rival technologies all in a very small footprint.

Design and fabrication process of the TPoS devices is discussed. Both silicon and diamond substrates are utilized for fabrication of TPoS devices and results are compared. Specifically, the superior acoustic properties of nanocrystalline diamond in scaling the frequency and energy density of the resonators is highlighted in comparison with silicon. The performance of TPoS devices in a variety of applications is reported. These applications include lateral-mode TPoS filters with record low IL values (as low as 2dB) and fractional bandwidth up to 1%, impedance transformers, very low phase noise oscillators, and passive wireless temperature sensors.

This dissertation is gratefully dedicated to my amazing husband for his support and encouragement during my doctoral journey. He has been my companion through thick and thin.

Thank you for being my rock when the research disasters hit!

I sincerely thank my advisor, Dr. Reza Abdolvand, for providing a positive learning environment to conduct research. I am also very thankful to my parents, Mastan and Behzad, for bringing me up as the person I am and always believing in me.

## **ACKNOWLEDGMENTS**

I would like to acknowledge the National Science Foundation for funding the majority of this project and all my colleagues at the Dynamic Microsystems Lab for their cooperation and the fruitful discussions.

## TABLE OF CONTENTS

LIST OF FIGURES .....	ix
LIST OF TABLES .....	xviii
LIST OF ABBREVIATIONS .....	xix
CHAPTER ONE: INTRODUCTION .....	1
CHAPTER TWO: BACKGROUND .....	6
2.1. Piezoelectric Resonator .....	6
2.1.1. Quality factor .....	7
2.1.2. Coupling coefficient .....	9
2.2. Thin-Film Piezoelectric-on-Substrate Devices .....	12
2.3. Lateral-Mode Piezoelectric Devices .....	15
2.3.1. Lateral-mode piezoelectric resonators .....	15
2.3.2. Lateral-mode piezoelectric filters .....	19
CHAPTER THREE: FABRICATION OF TPoS DEVICES .....	24
3.1. Preparation of UNCD Films .....	24
3.2. Deposition of AlN on Diamond Films .....	28
3.3. Fabrication Process .....	31
3.3.1. Silicon devices .....	32

3.3.2. Diamond devices.....	33
CHAPTER FOUR: SUBSTRATE CHARACTERIZATION.....	37
4.1. Characterizing UNCD Films.....	37
4.2. Nonlinearity and Power Handling .....	37
4.2.1. Quantifying power handling .....	40
4.2.2. Silicon versus diamond.....	42
CHAPTER FIVE: NARROW-BAND TPoS FILTERS .....	48
5.1. Monolithic TPoS Filter .....	48
5.1.1. Design concept.....	48
5.1.2. FEM model .....	50
5.1.3. Performance optimization of monolithic TPoS filters .....	53
5.1.4. Measurement results .....	57
5.1.5. Best monolithic filter designs .....	64
5.1.6. TCF and Power Handling .....	68
5.2. Novel designs with increased bandwidth.....	70
CHAPTER SIX: TPoS IMPEDANCE TRANSFORMERS.....	79
6.1. Introduction.....	79
6.2. Design Concept.....	80
6.3. Fabrication Process .....	83



6.4. Measurement Results .....	83
6.5. Conclusion .....	89
CHAPTER SEVEN: LOW-NOISE OSCILLATOR USING A TPoS RESONATOR .....	90
7.1. Introduction.....	90
7.2. Resonator Characterization and Oscillator Design .....	92
7.3. Oscillator Phase Noise .....	94
7.4. Verification of the Nonlinear Operation in Closed-Loop .....	98
7.5. Conclusion .....	100
CHAPTER EIGHT: PASSIVE WIRELESS TEMPERATURE SENSOR USING A TPoS RESONATOR.....	101
8.1. Introduction.....	101
8.2. TPoS Resonator .....	103
8.3. Wireless Measurement Setup.....	106
8.4. Experimental Results .....	108
8.5. Discussion .....	110
CHAPTER NINE: CONCLUSION .....	111
9.1. Accomplishments.....	111
9.2. Future Research .....	112
LIST OF REFERENCES .....	115

## LIST OF FIGURES

Figure 1: 3D schematic of thin-film piezoelectric-on-substrate resonator with three electrode fingers and a pair of tethers.....	14
Figure 2: Snapshots from the displacement field of a first order lateral-mode: (a) original shape, (b) fully contracted, (c) fully expanded. ....	15
Figure 3: Direction of the electric field and the strain vectors for a lateral-mode resonator. ....	17
Figure 4: Mode shapes for the first order (left) and the third order harmonics of the TPoS resonator of Figure 1. The areas in red are under tensile stress and areas in blue have compressive stress. The inset is the schematic of the TPoS resonators with three interdigitated electrode fingers.....	18
Figure 5: (a) Ladder filter topology [13], (b) higher order filter by electrical coupling of three contour-mode resonators [42, ], and (c) second order filter by mechanical coupling of two contour-mode resonators [43].....	20
Figure 6: Cross-section of a monolithic crystal filter which consists of a quartz crystal plate sandwiched between a solid bottom metal plate and top electrodes.....	22
Figure 7: (a) The rough surface of ZnO directly sputtered on nanocrystalline diamond, (b) Polished oxide was deposited as a buffer layer before the deposition of ZnO in order to reduce the surface roughness [9].....	25
Figure 8: Effect of buffer oxide layer on the frequency and mode-shape of the lateral-extensional resonator [14]: (a) The mode-shape for the device without the buffer oxide layer, (b) Same design with an oxide layer in between the substrate and the piezoelectric layer. ....	26
Figure 9: Dependency of the Young's modulus of the UNCD film on the deposition temperature. ....	28

Figure 10: AFM image of high Young's modulus (950 GPa) diamond film surface (a) before and (b) after chemical mechanical polishing showing less than 1nm final rms roughness. ....	28
Figure 11: Cross-section of a broken device showing the stack of Mo/AlN/Mo directly sputtered on UNCD. ....	30
Figure 12: Two-dimensional x-ray diffraction frames collected from a 500nm AlN film deposited directly on polished (a) and unpolished (b) ultrananocrystalline diamond films. ....	30
Figure 13: SEM of the smooth surface of AluminumNitride directly sputtered on polished UNCD film. ....	31
Figure 14: Rocking curve of the AlN film deposited on polished UNCD film with full-width half-maximum of 3°. ....	31
Figure 15: Fabrication process flow: (a) Silicon-on-insulator substrate, (b) Deposition and patterning the bottom metal layer, (c) Deposition of AlN and top metal layers, (d) Patterning Top metal to form the electrodes, (e) Wet-etching the AlN to gain access to the bottom metal, (f) Sputtering gold on the contact areas, (g) Etching of the stack, AlN in Cl <sub>2</sub> and silicon in SF <sub>6</sub> respectively, (h) Etching the handle silicon from the backside, (i) Final release of the structure by wet-etching the box oxide layer. ....	35
Figure 16: Fabrication process flow: (a) Patterning the bottom metal layer, (b) Deposition of AlN and top metal layer, followed by patterning the top metal, (c) Wet-etching the AlN to gain access to the bottom metal, (d) Sputtering gold on the contact areas, (e) Etching the stack (f) followed by releasing the device by etching the handle silicon from the backside. ....	36

Figure 17: Frequency response of a multi-tethered 21 <sup>st</sup> order TPoS resonator fabricated on silicon (a), UNCD with $E$ of 650GPa (b), 491GPa (c), and 933GPa (d). The insets on (a) and (b) show the SEM of the resonators fabricated on SOI and UNCD respectively.....	38
Figure 18: (a) SEM and (b) mode-shape showing the stress field of a third-order harmonic TPoS resonator.....	39
Figure 19: ADS model to measure the stored energy and dissipated power of the resonator. ....	41
Figure 20: Simplified equivalent BVD model for a typical resonator.....	42
Figure 21: Transmission response of a typical resonator on diamond substrate at 16.5dBm applied power showing hysteresis for forward and backward frequency sweeps. ....	43
Figure 22: Transmission responses of a typical resonator on silicon showing hysteresis at power levels above the bifurcation. ....	44
Figure 23: Transmission responses of a typical resonator on diamond showing hysteresis at power levels above the bifurcation. ....	44
Figure 24: Statistical data showing the critical energy density of various resonators measured on silicon and diamond substrates. ....	45
Figure 25: SEM of the two typical resonators on silicon and diamond after fracture. ....	46
Figure 26: Statistical data showing the fracture energy density of various resonators measured on silicon and diamond substrates. ....	47
Figure 27: Mode shapes for a 7 <sup>th</sup> order harmonic monolithic filter simulated in COMSOL <sup>®</sup> showing the strain fields for the in-phase mode (a) and the out-of-phase mode (b). The out-of-phase mode has a zero-displacement line (nodal line) at the middle of the length. ....	49

Figure 28: The schematic of a two-port multi-tethered 7 <sup>th</sup> harmonic monolithic filter showing the electrode pattern.....	50
Figure 29: (a) The model build in COMOSL for a 60 $\mu$ m long 7 <sup>th</sup> harmonic filter, (b) Strain field for the in-phase lateral-extensional mode. (c) Strain field for the out-of-phase lateral-extensional mode.....	52
Figure 30: Simulated frequency response of a 60 $\mu$ m long 7 <sup>th</sup> harmonic filter shown in Figure 29-a.....	53
Figure 31: (a) Typical frequency response of a two-pole filter with the 3dB-bandwidths of the two resonance peaks overlapping. (b) Definition of $\Delta f_{3dB}$ in this work, for designs where the 3dB-bandwidths of the two resonance peaks do not overlap.....	55
Figure 32: Simulated frequency responses for 56 $\mu$ m and 60 $\mu$ m long 7 <sup>th</sup> harmonic TPoS filters demonstrating the effect of increasing device length on the frequency separation between the two resonance modes. ....	56
Figure 33: Dependency of the frequency separation between the two resonance modes on the input/output electrode separation for a 7 <sup>th</sup> harmonic monolithic filter. ....	56
Figure 34: Effect of increasing the device length. Frequency responses are for the multi-tethered 33 <sup>rd</sup> harmonic monolithic filters with different length.....	58
Figure 35: Measured results from 33 <sup>rd</sup> harmonic filters with different lengths from all the 12 dies on the fabricated wafer with Young's modulus of 933GPa showing how the insertion loss (a) and the bandwidth (b) reducing on average as the length is increased.....	59
Figure 36: Frequency responses are for a typical 234 $\mu$ m 33 <sup>rd</sup> harmonic filters with different electrode separations between the input and output electrodes. ....	60

Figure 37: Results from 234 $\mu\text{m}$ long, 33 <sup>rd</sup> harmonic filters with different separations between the input and output electrodes measured from all the 12 dies on the fabricated wafer with $E$ of 933GPa showing how the insertion loss (a) and bandwidth (b) are affected. ....	61
Figure 38: Frequency responses for monolithic filters with different order harmonics and approximately same aspect ratios. ....	62
Figure 39: Effect of order of the harmonic on the filter performance. Insertion loss (a) and bandwidth (b) data collected from all the devices measured on the UNCD wafer with Young's modulus of 933GPa.....	63
Figure 40: Effect of different support configurations on insertion loss (a) and bandwidth (b) of a 212.4 $\mu\text{m}$ long 25 <sup>th</sup> harmonic filter. ....	64
Figure 41: The SEM of a 37 <sup>th</sup> harmonic monolithic filter with 19 pairs of tethers along the width and two additional pairs at the two ends of the length.....	65
Figure 42: Frequency responses of the 37 <sup>th</sup> harmonic filters with the lowest insertion loss on the three diamond wafers with Young's modulus of (a) 650GPa, (b) 933GPa, and (c) 491GPa.....	66
Figure 43: (a) The measured and simulated frequency responses of the 37 <sup>th</sup> harmonic TPoD monolithic filter and (b) the equivalent electrical circuit model of the filter.....	67
Figure 44: Wide-span frequency response of the multi-tethered 37 <sup>th</sup> harmonic filter on 933GPa UNCD substrate showing very few spurious modes in the entire frequency range. ....	67
Figure 45: Frequency response of a 25 <sup>th</sup> harmonic design with the largest bandwidth (0.2%) among all the designs of this work. ....	68
Figure 46: The overlapped frequency responses of the 37 <sup>th</sup> harmonic monolithic filter at different temperatures. ....	69

Figure 47: The overlapped frequency responses of the filter at different applied power levels. ..	70
Figure 48: Simulated frequency response of a 7 <sup>th</sup> order (a) rectangular and (b) xylophone monolithic filter. The rectangular monolithic filter is a second order filter with two resonance peaks coupled together. There are at least peaks coupled together for the xylophone design resulting in a larger bandwidth. ....	72
Figure 49: Layout of the 35 <sup>th</sup> order xylophone filter. The length of the filter is decreased linearly from 243 $\mu$ m to 315 $\mu$ m. ....	73
Figure 50: Frequency response of a 35 <sup>th</sup> order xylophone design fabricated on SOI substrate. ..	73
Figure 51: Layout of an hourglass filter design. ....	75
Figure 52: Frequency response of the hourglass design with 31 electrode fingers fabricated on SOI substrate. ....	77
Figure 53: Model built in ADS to simulate the filter design with different terminations. ....	78
Figure 54: Frequency response of the hourglass filter with different terminations. The R represents the resistor and L is the inductor added in parallel to the resistive termination. ....	78
Figure 55: Illustration of a thin-film piezoelectric-on-substrate resonator with eight electrode fingers. ....	80
Figure 56: Butterworth Van Dyke equivalent circuit model of a two-port resonator. ....	81
Figure 57: Simulation results showing the effect of output termination on the voltage gain for a 10 <sup>th</sup> order TPoS resonator. ....	81
Figure 58: (a) Mode shape for an 8 <sup>th</sup> order TPoS resonator. Red shows the tensile stress and blue represents compressive stress. (b) Electrode configuration for a conventional resonator. (c) Electrode configuration for an impedance transformer. ....	82

Figure 59: Fabrication process flow for the thin-film piezoelectric-on-substrate transformers. (a) patterning the bottom metal layer, (b) Etching AlN to access the bottom metal after the deposition of AlN/Mo stack and patterning the top metal, (c) Sputtering gold on the formed vias to make contact between the top and bottom metal layers, etching the device stack from the top and also the handle silicon from the backside followed by releasing the device by etching the oxide layer.	84
Figure 60: SEM showing 10 <sup>th</sup> order TPoS (a) resonator and (b) transformer.	85
Figure 61: Transmission plots for the 10 <sup>th</sup> order resonator and transformer measured with 50Ω terminations.	86
Figure 62: Z11 and Z22 parameters for the resonator (a) and transformer (b) designs.	87
Figure 63: The transmission response of the transformer with different termination loads at the output.	88
Figure 64: Input and output waveforms for the 10 <sup>th</sup> order transformer at the resonance frequency with 2.3μH inductive termination at the output port.	89
Figure 65: Frequency response of the TPoS resonator of this work at different applied powers. Inset: SEM of the resonator signifying the ports in colors.	93
Figure 66: Schematic of the oscillator circuit. The inset on the right shows the output waveform with ±5.5 supply voltage.	94
Figure 67: Voltages on the input and output ports of the resonator in closed-loop versus the positive supply voltage, showing a steady increase as the supply voltage is increased.	95
Figure 68: (a) Oscillation frequency and (b) Phase noise at 1KHz and 1MHz offset frequencies from the carrier versus the oscillator output voltage showing a noticeable drop at 7.2V <sub>pk-pk</sub> .	96



Figure 69: Phase noise plots for supply voltages greater than 4V showing a steady decrease as the voltage is increased. ....	97
Figure 70: Measured and normalized (to 10MHz) phase noise plots of the oscillator with oscillation voltage of $7.2V_{pk-pk}$ . The square and circle represent the best normalized phase noise values reported in literature for MEMS piezoelectric [79] and capacitive [80] oscillators respectively. ....	97
Figure 71: (a) Schematic of the one-port measurement setup. (b) $S_{11}$ plots in linear region and at the edge of bifurcation measured with $50\Omega$ and open termination. Note the slight frequency difference between the two cases indicated at 10dBm input power. ....	99
Figure 72: Normalized frequency shift ( $\Delta f/f_0$ ) vs. the output voltage (the voltage on the two-fingered port) of the resonator. ....	100
Figure 73: (a) The schematic of a 5 <sup>th</sup> order TPoS resonator and (b) the stress profile of a silicon slab with two pairs of fixed tethers at the 5 <sup>th</sup> order width-extensional mode. ....	104
Figure 74: (a) Frequency characteristics and (b) the equivalent circuit model of the one-port TPoS resonator. ....	105
Figure 75: Measurement setup of the wireless temperature sensor. The MEMS resonator on the right is a 21 <sup>st</sup> order multi-tether design and is directly connected to an antenna. ....	107
Figure 76: Waveform as received by the oscilloscope showing the interrogation signal and the resonator response. The measurement was performed at room temperature and transmit power of 0.5W at 10cm sensing distance. The inset shows the portion of the signal that is time gated for further processing. ....	107
Figure 77: The spectral density of the resonator decay response after taking Fourier transform of the time-gated waveform of Figure 76-b. ....	108

Figure 78: The resonance frequency vs. the resonator's temperature measured in direct and wireless configurations with TCF of -30ppm/°C. The slight frequency shift between the two cases is due to different loading on the resonator. ....	109
Figure 79: Histogram of 2000 temperature samples collected at room temperature. ....	109
Figure 80: The cross-section of the proposed pressure sensor to measure the absolute value of the pressure. The resonant disk is suspended by forming a cavity in the substrate. ....	113
Figure 81: A proposed MEMS sensor platform with passive temperature and pressure sensors. Both sensors are directly connected to a patch antenna and send/receive the signal. ....	114

## LIST OF TABLES

Table 1: Characteristics of the diamond films used for fabrication of TPoD resonators. ....	29
Table 2: Experimental results of two typical TPoS devices fabricated on diamond and silicon right before hysteresis.....	45
Table 3: Experimental results of two typical TPoS devices fabricated on diamond and silicon right before fracture. ....	46
Table 4: The insertion loss and bandwidth of typical 33 <sup>rd</sup> harmonic monolithic filters with different lengths. ....	59
Table 5: Performance characteristics of the resonator and transformer when measured with 50 $\Omega$ terminations.....	85

## **LIST OF ABBREVIATIONS**

ADS: Advanced Design System

AlN: Aluminum Nitride

BOE: Buffered Oxide Etchant

DUT: Device Under Test

FBAR: Film Bulk Acoustic Resonator

FEM: Finite Element Model

FFT: Fast Fourier Transform

IC: Integrated Circuit

IDT: Interdigitated Electrodes

IF: Intermediate Frequency

IL: Insertion Loss

MCF: Monolithic Crystal Filter

MEMS: Micro ElectroMechanical Systems

Mo: Molybdenum

LNA: Low-Noise Amplifier

PCB: Printed Circuit Board

PML: Perfect Matching Layer

Q: Quality factor

RF: Radio Frequency

SAW: Surface Acoustic Wave

SEM: Scanning Electron Micrograph

SOI: Silicon On Insulator

SOLT: Short-Open-Load-Through

STD: Standard Deviation

TCF: Temperature Coefficient of Frequency

TMAH: TetraMethylAmmonium Hydroxide

TPoD: Thin-film Piezoelectric-On-Diamond

TPoS: Thin-film Piezoelectric-On-Substrate

UNCD: Ultra Nano Crystalline Diamond

ZnO: Zinc Oxide

## CHAPTER ONE: INTRODUCTION

As mobile electronics industry pushes forward, their products demand lower power, smaller components, and greater integration. Reference oscillators are demanded in almost every electronic system for timing and frequency control in various applications. At the heart of every oscillator is a mechanically vibrating element with high quality factor (Q) and very low-spurious profile to provide an accurate frequency synthesis and stability. Filters are incorporated in a vast majority of electrical applications to perform frequency selection and transmit certain frequency bands and block the rest of the frequencies depending on the application. High performance filters with small size are highly desired for mobile communication systems in a wide frequency spectrum. Bluetooth<sup>®</sup> and WLAN at 2.4GHz, and the 850MHz and 1.9GHz bands for GSM and CDMA carriers respectively are examples of such applications. As the frequency spectrum becomes more and more populated due to the rise of new applications, the constraints on the filter performance get tighter in order to use the spectrum more efficiently. These constraints are higher out-of-band rejection, sharper roll-off, and precise bandwidth requirements. On the other hand, battery-powered applications impose an additional constraint on the insertion loss (IL) of both resonators and filters demanding near 0dB energy loss. The size of the resonators and filters also becomes critical as designers attempt to fit more components on a smaller chip area.

Quartz crystal resonators exhibit very high Q and have been utilized in oscillators with very low phase noise (PN) values and excellent temperature stability for high performance applications [1, and for a brief history refer to 2]. The drawback however is their relatively large size and the fact that their fabrication process is incompatible with the mature silicon micro-fabrication

technology. High-Q micromachined resonators, on the other hand can potentially be integrated with CMOS and offer a competing alternative for the bulky quartz resonators in a wide variety of consumer electronics where size and cost are critical factors. Microelectromechanical system (MEMS) is an emerging technology that has grown to become a competitive alternative for low cost, small size, and high performance solutions for various timing and frequency control applications. However, there are still critical shortcomings such as relatively large temperature coefficient of frequency (TCF), low power handling, and large insertion loss (IL) [3] that are yet to be overcome before MEMS can meet the demanding specifications of RF systems.

There are two main transduction methods that have been explored to build on-chip micromachined resonators: electrostatic and piezoelectric. Numerous capacitive resonators based on electrostatic actuation have been developed and demonstrated with some of the highest quality factors reported for MEMS resonators. However, these resonators commonly suffer from large motional resistances in the range of a few  $k\Omega$  which increases at higher frequencies [4, 5, 6]. In order to reduce such large motional resistances, DC bias voltages larger than 5 V is typically required which renders them undesirable in IC technologies [7]. In addition, achieving higher frequency in capacitive resonators requires very small gaps (few tens of nanometers) between the resonator and the electrodes which complicates the fabrication process [8]. Plus, the capacitive resonators exhibit poor linearity, especially at higher frequencies with smaller gaps.

On the other hand, piezoelectric transducers offer larger electromechanical coupling coefficient relative to that of electrostatic transduction, which plays an important role in achieving low-impedance resonators and low insertion loss filters [9, 10, 11]. While lateral-mode (or

contour-mode) piezoelectric resonators benefit from the relatively large coupling coefficient of the piezoelectric material, they also enable dispersed-frequency resonators on a single substrate. Such piezoelectric resonators have been reported with high quality factors and resonance frequencies in the range of tens of KHz to several GHz [9, 12, 13, 14]. Thin-film piezoelectric-on-substrate (TPoS) resonators developed by our group exhibit superior power handling capability and robustness compared to lateral-mode resonators without substrate [15]. A few applications incorporating high-Q TPoS resonators are presented in this work. Also, as a part of this work, diamond is evaluated as the substrate for fabricating TPoS devices. The power handling and temperature sensitivity of TPoS resonators fabricated on diamond substrates are compared with devices fabricated on silicon.

Conventionally, filters have been realized by integrated circuit (IC) technology using LC tanks. However, the inductors take up a lot of room on the chip and the purely electronic filters become very lossy and inefficient at higher frequencies. Today, one of the most common filtering technologies is based on the surface acoustic wave (SAW) devices [16]. Despite their desirable performance, SAW devices cannot be integrated with other circuitries and could suffer from a relatively large temperature coefficient of frequency [17, 18, 19, 20]. More recently, filters using film bulk acoustic resonators (FBAR) are successfully manufactured and utilized for a broad range of applications [21, 22, 23]. These filters offer large bandwidth and very low insertion loss in addition to considerable size/cost benefits. However, with the FBAR technology being based on the thickness-mode piezoelectric resonators, it cannot be readily exploited to realize multi-band filtering on a single chip.



This work discusses the design procedure of the lateral-mode TPoS filters and describes the effect of different geometric features and physical parameters on the performance of the monolithic filters with the focus being on minimizing the IL and increasing the bandwidth of such filters. The discussions are then evaluated by the measurement results. IL values as low as 2dB and bandwidth as large as 1% are demonstrated. Furthermore, the nonlinear behavior of these filters is examined for input powers up to +35dBm.

This dissertation is prepared in 9 chapters. The current chapter is a brief introduction to the current technologies for realizing high performance oscillators and filters. Advantages of resonators based on piezoelectric transduction over the rival technologies are concisely discussed. Chapter two reviews the theory and concept of operation of piezoelectric resonant devices. Filter topologies based on lateral-mode piezoelectric devices are reviewed and the limit on the achievable bandwidth is examined in this chapter. Monolithic TPoS filters are also introduced as a new class offering low-loss and narrow-band frequency selection. The work done to deposit thin diamond films with optimum characteristics and the fabrication process of high frequency TPoS devices is thoroughly explained in chapter three. Chapter four compares the performance of TPoS resonators fabricated on UNCD with those fabricated on silicon in terms of Q, TCF, and power handling. A general method is presented to evaluate the power handling of resonators. Monolithic TPoS filters are thoroughly discussed in chapter five and methods to improve their performance are evaluated by finite element model (FEM) simulations and by the experimental results from designs with different configurations and various geometries. A filter with a record low insertion loss at 900 MHz and low TCF value is demonstrated followed by novel designs with 1% fractional bandwidth. Chapters 6, 7, and 8 showcase a few applications employing TPoS resonators. A piezoelectric

transformer is introduced in chapter six which is realized by modifying the electrode configuration of a high order TPoS resonator. This piezoelectric impedance transformer exhibits an impedance transformation ratio of 19:1 in a very small footprint. Chapters seven demonstrates a very low phase noise 27MHz oscillator employing a TPoS resonator. The passive wireless temperature sensor presented in chapter eight utilizes a 900MHz TPoS resonator and has a temperature resolution of less than 0.1°C at 1m distance. Lastly, the accomplishments of this dissertation are summarized in chapter nine and the future research is outlined.

## CHAPTER TWO: BACKGROUND

This chapter will first briefly discuss the concept of operation of piezoelectric resonators, and define the quality factor and electromechanical coupling coefficient. Two classes of piezoelectric devices will be introduced. Then the lateral-mode piezoelectric resonators will be described. After presenting some of the current work on both contour-mode resonators (CMR) and TPoS resonators, different filter topologies will be introduced.

### 2.1. Piezoelectric Resonator

In general, a piezoelectric material deforms when subjected to an electric field. The general constitutive equations of piezoelectricity are as follows:

$$D = d T + \epsilon^T E \quad (1)$$

$$S = s^E T + d^t E \quad (2)$$

where vectors  $D_{3 \times 1}$  ( $\frac{C}{m^2}$ ),  $T_{6 \times 1}$  ( $\frac{N}{m^2}$ ),  $E_{3 \times 1}$  ( $\frac{N}{C}$ ), and  $S_{6 \times 1}$  ( $\frac{m}{m}$ ) represent electric displacement field, stress, electric field, and strain respectively. The coefficient matrixes are compliance matrix ( $s_{6 \times 6}$ ), piezoelectric strain constants ( $d_{3 \times 6}$ ), and dielectric constant ( $\epsilon_{3 \times 3}$ ). Expanding the above equations:

$$\begin{bmatrix} D_1 \\ D_2 \\ D_3 \end{bmatrix} = \begin{bmatrix} d_{11} & d_{12} & d_{13} & d_{14} & d_{15} & d_{16} \\ d_{21} & d_{22} & d_{23} & d_{24} & d_{25} & d_{26} \\ d_{31} & d_{32} & d_{33} & d_{34} & d_{35} & d_{36} \end{bmatrix} \begin{bmatrix} T_1 \\ T_2 \\ T_3 \\ T_4 \\ T_5 \\ T_6 \end{bmatrix} + \begin{bmatrix} \epsilon_{11} & \epsilon_{12} & \epsilon_{13} \\ \epsilon_{21} & \epsilon_{22} & \epsilon_{23} \\ \epsilon_{31} & \epsilon_{32} & \epsilon_{33} \end{bmatrix} \begin{bmatrix} E_1 \\ E_2 \\ E_3 \end{bmatrix} \quad (3)$$

$$\begin{bmatrix} S_1 \\ S_2 \\ S_3 \\ S_4 \\ S_5 \\ S_6 \end{bmatrix} = \begin{bmatrix} s_{11} & s_{12} & s_{13} & s_{14} & s_{15} & s_{16} \\ s_{21} & s_{22} & s_{23} & s_{24} & s_{25} & s_{26} \\ s_{31} & s_{32} & s_{33} & s_{34} & s_{35} & s_{36} \\ s_{41} & s_{42} & s_{43} & s_{44} & s_{45} & s_{46} \\ s_{51} & s_{52} & s_{53} & s_{54} & s_{55} & s_{56} \\ s_{61} & s_{62} & s_{63} & s_{64} & s_{65} & s_{66} \end{bmatrix} \begin{bmatrix} T_1 \\ T_2 \\ T_3 \\ T_4 \\ T_5 \\ T_6 \end{bmatrix} + \begin{bmatrix} d_{11} & d_{21} & d_{31} \\ d_{12} & d_{22} & d_{32} \\ d_{13} & d_{23} & d_{33} \\ d_{14} & d_{24} & d_{34} \\ d_{15} & d_{25} & d_{35} \\ d_{16} & d_{26} & d_{36} \end{bmatrix} \begin{bmatrix} E_1 \\ E_2 \\ E_3 \end{bmatrix} \quad (4)$$

By applying an alternating electric field to a structure comprising a piezoelectric material, a stress field is generated. When the frequency of the electric field is equal to one of the natural resonance frequencies of the structure, it will force the structure into resonance.

A piezoelectric resonator is an electromechanical device in which electrical and mechanical energies are reciprocally converted to each other at a certain frequency (i.e. the resonance frequency of the resonator). The resonance frequency is a function of material properties and the device geometry. The overall performance of the resonator is governed by the efficiency of the energy conversion between electrical and mechanical domains. To quantify the performance, there are two specific parameters defined as *electromechanical coupling* and *quality factor (Q)* which are discussed below.

### 2.1.1. Quality factor

The resonator Q is a measure of the confinement of the input energy in the resonant structure. As in any non-ideal system, there are several inherent loss mechanisms in the piezoelectric transformation. Hence, not all of the applied energy is confined in the resonator structure at resonance, resulting in a limited Q. Some of the dissipation mechanisms are intrinsic to the resonator and some are extrinsic. An example of extrinsic loss mechanisms is the support loss which refers to part of the elastic energy leaking out of the resonator to the rest of the substrate

through the tethers as the acoustic wave travels within the resonator [24, 66]. Another portion of the energy is lost as heat due to the electrical resistance of the metal electrodes, leads, and contacts pads, known as electrical loss. There is also air damping or viscous loss which is present when the resonator operates in air and is inversely proportional to frequency becoming a dominant source of loss at lower frequencies. An intrinsic source of loss is the portion of the applied energy that is irreversibly transformed into heat as the structure vibrates. It is usually denoted as the material damping or the thermoelastic damping.

. In this work the targeted frequencies are in the range of 400MHz-1.2GHz and the primary loss mechanisms in this frequency range are the electrical and the support loss with the latter being more substantial.

The quality factor of a system is generally defined as [24]:

$$Q = 2\pi \frac{\text{peak energy stored}}{\text{energy dissipated per cycle}} \quad (5)$$

Thus, the overall quality factor of a system can be found by summing up the dissipated energies:

$$Q_{total} = 2\pi \frac{E_{stored}}{\sum_i E_{dissipated_i} / cycle} = \sum_i \frac{1}{Q_i} \quad (6)$$

As a result the overall quality factor would be smaller than the quality factor associated with any of the dissipation mechanisms.

The  $Q$  of a resonator can be extracted from the slope of the impedance phase response by  $Q = \frac{f_s}{2} \frac{\partial \angle Z}{\partial f} \big|_{f_s}$ . For resonators  $Q$  can also be approximated by the ratio of the center frequency and the 3dB-bandwidth of the resonator:

$$Q = \frac{f_0}{\Delta f_{3dB}} \quad (7)$$

### 2.1.2. Coupling coefficient

The piezoelectric coupling coefficient ( $K^2$ ) represents the ability of a piezoelectric material to transform electrical energy to mechanical energy and vice versa, thus it is defined as the ratio of the electrical energy to mechanical energy. The stored electrical and mechanical energies are calculated by the below equations:

$$U_E = \frac{1}{2} \epsilon^S E^2 \quad (8)$$

$$U_m = \frac{1}{2} c^E S^2 \quad (9)$$

The piezoelectric coupling can be represented in terms of material properties as follows (given the stress is only non-zero in one direction):

$$K^2 = \frac{U_E}{U_M} = \frac{e^2}{c^E \epsilon^S} \quad (10)$$

The proportionality of the coupling factor with the second power of piezoelectric coefficient is trivial as the same piezoelectric coefficient that relates stress from mechanical domain to electric field in the electrical domain. The inverse proportionality to the stiffness could be understood by

the smaller mechanical displacement for a unit applied electric field that is realized as the stiffness of the piezoelectric material increases. Finally, the inverse proportionality to the dielectric constant could be intuitively described by the larger portion of the total energy that is conserved in the electrical domain (i.e. not converted to mechanical energy) for a piezoelectric material with larger dielectric constant. The above equation in terms of the piezoelectric constants is equivalent to:

$$K_{ij}^2 = \frac{d_{ij}^2}{s_{ij}^E \epsilon_{ii}^T} \quad (11)$$

Subscripts i and j represent the direction of the applied electric field and the induced stress respectively [25].

$$\text{The electromechanical coupling coefficient is: } k^2 = \frac{U_E}{U_E + U_M} = \frac{K^2}{1 + K^2} = \frac{e^2}{c^E \epsilon^S + e^2} \quad (12)$$

Any resonant system exhibits a resonance ( $f_r$ ) and an anti-resonance ( $f_a$ ). From an electrical standpoint, the input impedance exhibits its minimum and maximum values at the resonance and anti-resonance respectively. The frequency separation between the resonance and anti-resonance is a function of the electromechanical coupling coefficient ( $k^2$ ). For a thickness-mode loss-less single-layer resonator (with a single piezoelectric layer and ignoring the effect of electrodes) the electromechanical coupling coefficient is [26]:

$$k_t^2 = \left(\frac{\pi}{2}\right) \frac{f_s}{f_p} \tan \frac{\pi}{2} \left(\frac{f_p - f_s}{f_p}\right) \quad (13)$$

where t denotes the thickness. For small values of  $k_t^2$ , this equation simplifies to:

$$k_t^2 = \left(\frac{\pi^2}{4}\right) \frac{f_s}{f_p} \frac{f_p - f_s}{f_p} \quad (14)$$

For a multi-layer lossy resonator or when a simple one-dimensional approximation does not fully describe the resonator's behavior, it is not straightforward to find a closed-form equation for  $k^2$ . Thus, an *effective* electromechanical coupling coefficient is defined according to IEEE standard on piezoelectricity [27]:

$$k_{eff}^2 = \frac{f_p^2 - f_s^2}{f_p^2} \quad (15)$$

Based on this standard, the figure of merit for resonators is defined as:

$$M = \frac{k_{eff}^2 \cdot Q}{1 - k_{eff}^2} \quad (16)$$

However, the anti-resonance of longitudinal and thickness mode resonators are usually obscured by the unwanted spurious modes, especially as the resonators get larger [28]. Onoe introduces a new method to extract the coupling coefficient and claims  $\tan X = X/k^2$  where  $X = \omega t/2V$  with  $\omega$  being the angular frequency,  $t$  the thickness, and  $V$  the phase velocity to be the governing relation between the electromechanical coupling and the fundamental or overtone frequencies of a thickness-mode piezoelectric resonator (either the thickness-dilatational or thickness-shear modes). For lateral-extensional resonators, like the ones in this work, there is no such approximation in the literature. Thus, equation (19) is used to estimate the effective coupling for resonators of this work.

In order to improve the effective coupling of a resonator, piezoelectric materials with higher piezoelectric coupling coefficient are desired. ZnO, AlN, PZT, and LN are such piezoelectric materials. Even though, AlN has a slightly smaller coupling coefficient compared to ZnO, its high



electrical resistance, high breakdown voltage, small dielectric constant, as well as its compatibility with CMOS fabrication process makes it a suitable candidate for microelectromechanical piezoelectric resonators [29].

In general, the effective electromechanical coupling is lower for overtuned resonators [30]. Also, it is shown that the piezoelectric-on-substrate resonators have an inferior effective electromechanical coupling coefficient compared to purely piezoelectric resonators [31].

Generally, higher coupling coefficient reduces the insertion loss and increases the filter bandwidth. The thicker the substrate, the higher the Q but also the larger the insertion loss due to a lower electromechanical coupling coefficient [32]. Increasing the electrode width reduces the IL as well, again due to a higher coupling.

## 2.2. Thin-Film Piezoelectric-on-Substrate Devices

In general, a piezoelectric material deforms when subjected to an electric field. The general constitutive equations of piezoelectricity are as follows:

$$D = d T + \epsilon^T E \quad (17)$$

$$S = s^E T + d^t E \quad (18)$$

where vectors  $D_{3 \times 1}$  ( $\frac{C}{m^2}$ ),  $T_{6 \times 1}$  ( $\frac{N}{m^2}$ ),  $E_{3 \times 1}$  ( $\frac{N}{C}$ ), and  $S_{6 \times 1}$  ( $\frac{m}{m}$ ) represent electric displacement field, stress, electric field, and strain respectively. The coefficient matrixes are compliance matrix ( $s_{6 \times 6}$ ), piezoelectric strain constants ( $d_{3 \times 6}$ ), and dielectric constant ( $\epsilon_{3 \times 3}$ ). Expanding the above equations:

$$\begin{bmatrix} D_1 \\ D_2 \\ D_3 \end{bmatrix} = \begin{bmatrix} d_{11} & d_{12} & d_{13} & d_{14} & d_{15} & d_{16} \\ d_{21} & d_{22} & d_{23} & d_{24} & d_{25} & d_{26} \\ d_{31} & d_{32} & d_{33} & d_{34} & d_{35} & d_{36} \end{bmatrix} \begin{bmatrix} T_1 \\ T_2 \\ T_3 \\ T_4 \\ T_5 \\ T_6 \end{bmatrix} + \begin{bmatrix} \epsilon_{11} & \epsilon_{12} & \epsilon_{13} \\ \epsilon_{21} & \epsilon_{22} & \epsilon_{23} \\ \epsilon_{31} & \epsilon_{32} & \epsilon_{33} \end{bmatrix} \begin{bmatrix} E_1 \\ E_2 \\ E_3 \end{bmatrix} \quad (19)$$

$$\begin{bmatrix} S_1 \\ S_2 \\ S_3 \\ S_4 \\ S_5 \\ S_6 \end{bmatrix} = \begin{bmatrix} s_{11} & s_{12} & s_{13} & s_{14} & s_{15} & s_{16} \\ s_{21} & s_{22} & s_{23} & s_{24} & s_{25} & s_{26} \\ s_{31} & s_{32} & s_{33} & s_{34} & s_{35} & s_{36} \\ s_{41} & s_{42} & s_{43} & s_{44} & s_{45} & s_{46} \\ s_{51} & s_{52} & s_{53} & s_{54} & s_{55} & s_{56} \\ s_{61} & s_{62} & s_{63} & s_{64} & s_{65} & s_{66} \end{bmatrix} \begin{bmatrix} T_1 \\ T_2 \\ T_3 \\ T_4 \\ T_5 \\ T_6 \end{bmatrix} + \begin{bmatrix} d_{11} & d_{21} & d_{31} \\ d_{12} & d_{22} & d_{32} \\ d_{13} & d_{23} & d_{33} \\ d_{14} & d_{24} & d_{34} \\ d_{15} & d_{25} & d_{35} \\ d_{16} & d_{26} & d_{36} \end{bmatrix} \begin{bmatrix} E_1 \\ E_2 \\ E_3 \end{bmatrix} \quad (20)$$

When a piezoelectric structure is subjected to an alternating electric field, a stress field is generated deforming the structure. If the frequency of the applied electric field is equal to one of the natural resonance frequencies of the structure, it will be forced into resonance.

As indicated in the introduction of this dissertation, The piezoelectric resonators and filters can be classified into two categories: those that are comprised of only a thin piezoelectric layer [5, 6, 7] and those with the piezoelectric layer stacked on a relatively thicker substrate which forms the bulk of the device and are referred to as the thin-film piezoelectric-on-substrate (TPoS) devices [8, 14, 15]. The substrate is chosen to have low acoustic loss, high acoustic velocity, and high energy density or in other words high Q. TPoS devices which are the focus of this work can potentially offer better power handling and smaller TCF [15, 33, 34]. The schematic of a two-port TPoS resonator with three interdigitated electrodes (IDT) is displayed in Figure 1. The piezoelectric film is sandwiched between two metal layers and is actuated by the applied electric field. The TPoS device depicted in Figure 1 is a two-port configuration where the electric field is applied between the input electrodes and the bottom ground plate and the generated charge is harvested from the output electrode(s). Nonetheless, TPoS devices can be configured in a one-port fashion depending

on the application.

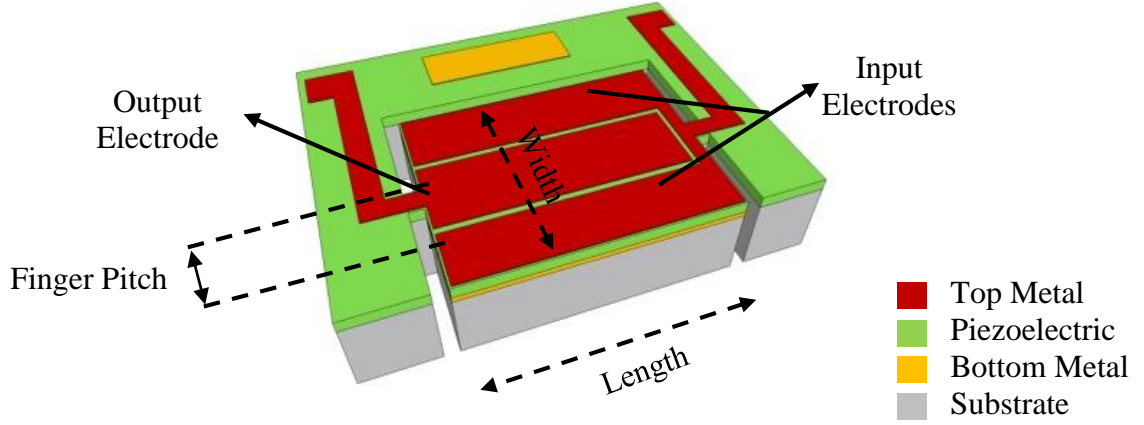


Figure 1: 3D schematic of thin-film piezoelectric-on-substrate resonator with three electrode fingers and a pair of tethers.

The resonance frequency of TPoS devices is a function of device geometries and the overall stiffness of the structure or in other words the overall Young's modulus. For thickness-mode resonators, the frequency is defined by the thickness of the piezoelectric film and for lateral-mode devices it is a function of device length. One advantage of TPoS technology is the possibility of extending the center frequency by incorporating a material with large Young's modulus, e.g. diamond, as the structural body of the device. This enables achieving higher frequencies without the need for extremely small feature sizes. In addition, the freedom in choosing the stack material allows for engineering the TCF of the resonant devices for different applications.

The performance of piezoelectric resonators strongly depends on the quality of the piezoelectric film. To deposit piezoelectric films with large piezoelectric coefficient, the surface roughness of the substrate has to be reduced in order for the piezoelectric grains to grow in a certain crystalline orientation. The TPoS devices of this work incorporate Aluminumnitride (AlN) as the

piezoelectric material and both silicon and diamond substrates are utilized as the substrate for realization of these TPoS devices.

## 2.3. Lateral-Mode Piezoelectric Devices

### 2.3.1. Lateral-mode piezoelectric resonators

In a lateral-mode resonator, the acoustic wave travels in the bulk of the structure inducing in-plane vibrations in the resonator. The displacement field of a first order lateral mode at  $t = 0$ ,  $t = \frac{T}{4}$ , and  $t = \frac{3T}{4}$  is displayed in Figure 2 ( $T = \frac{1}{f}$  is the period of vibrations). During the first half of the resonance period, the resonant structure contracts to a minimum length and then expands to a maximum during the second half and then back to its original shape. The free-standing structure is usually suspended by a few tethers connected to the nodal points to minimize the distortion of the mode-shape.

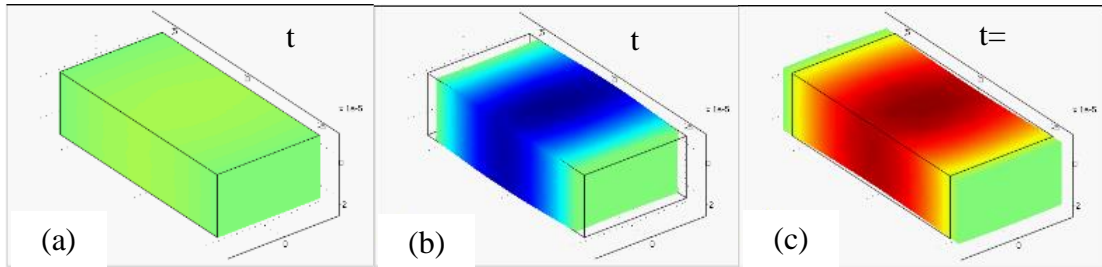


Figure 2: Snapshots from the displacement field of a first order lateral-mode: (a) original shape, (b) fully contracted, (c) fully expanded.

The frequency of the vibrations ( $f$ ) is a function of the acoustic velocity ( $v_a$ ) and the lateral dimensions of the structure e.g. for the first harmonic the wavelength ( $\lambda$ ) is twice the length of the structure. Generally,

$$f = \frac{v_a}{\lambda} = n \frac{v_a}{2L} \quad (21)$$

where  $n$  is the order of the harmonic.

The material acoustic velocity is equal to:

$$v_a = \sqrt{\frac{c^E}{\rho}} \quad (22)$$

with  $\rho$  ( $\frac{kg}{m^3}$ ) being the material density and  $c^E$  the stiffness in the direction of propagation (or the elastic constant with the unit of  $N/m^2$ ) in the absence of an electric field. Applying an electric field to the material modifies the effective stiffness:  $c^D = c^E + \frac{e^2}{\epsilon^2}$ , where  $e$  ( $\frac{C}{N}$ ) is the piezoelectric constant and  $\epsilon$  ( $\frac{F}{m} = \frac{C}{V.m}$ ) is the dielectric constant, and thus the acoustic velocity changes to:

$$v_a' = \sqrt{\frac{c^E + e^2/\epsilon^2}{\rho}} = v_a \sqrt{1 + K^2} \quad (23)$$

In order to excite such lateral modes in a structure, various actuation mechanisms e.g. piezoelectric or capacitive, can be employed. Here, our focus is on lateral-mode piezoelectric resonators.

For lateral-mode piezoelectric resonators, the direction of the applied electric field is perpendicular to that of the induced stress as shown in Figure 3. This configuration is also referred

to as the transverse mode versus the longitudinal mode where the electric field and stress vectors are in parallel [35].

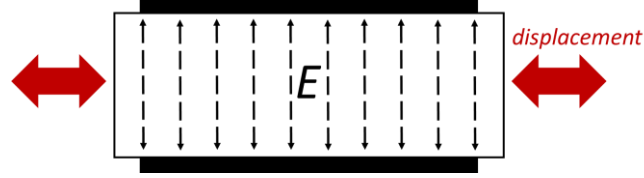


Figure 3: Direction of the electric field and the strain vectors for a lateral-mode resonator.

Assuming that the electric field is applied in the  $z$  direction across the piezoelectric material with no mechanical loading on the resonator ( $T = 0$ ), equations (4) and (5) for a transverse mode can be simplified to:

$$D_3 = \epsilon_{33}E_3 \quad (24)$$

$$S = d^t E_3 \quad (25)$$

Taking the piezoelectric coefficient matrix for AlN [36]:

$$d_{ij} = \begin{bmatrix} 0 & 0 & 0 & 0 & 4 & 0 \\ 0 & 0 & 0 & 4 & 0 & 0 \\ -2 & -2 & 5 & 0 & 0 & 0 \end{bmatrix} \frac{pC}{N}$$

the shear components of the strain tensor ( $S_4, S_5$ , and  $S_6$ ) become zero.

Figure 4 shows the mode shape for the first and third harmonics of the TPoS resonator displayed in Figure 1. For the first order harmonic, the width of the structure is equal to half wavelength at the resonance frequency. For higher harmonics, the electrode pattern is designed to match the strain field developed in the structure at a targeted mode shape and therefore appears as

interdigitated electrodes where the electrode finger pitch defines the resonance frequency of the resonator. The finger pitch of the electrodes which is the center-to-center distance of two adjacent electrodes (Figure 1) is equal to half the wavelength at the target resonance frequency. A resonator designed with  $n$  electrode fingers patterned on the top metal layer is called an  $n^{\text{th}}$  order resonator in this work. The support tethers are placed at the nodal points where the displacement is near zero in order to minimize the distortion of the strain field and therefore, minimize the anchor loss.

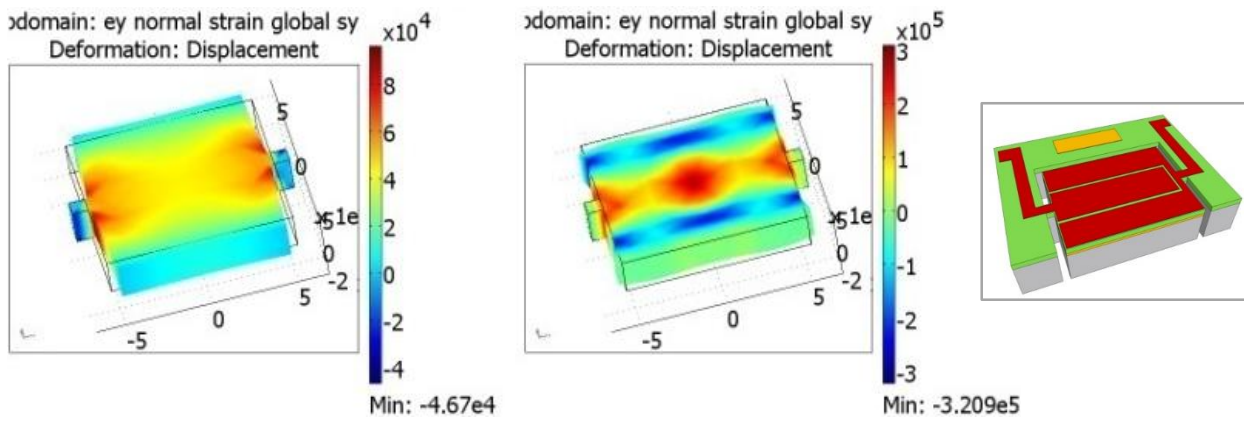


Figure 4: Mode shapes for the first order (left) and the third order harmonics of the TPoS resonator of Figure 1. The areas in red are under tensile stress and areas in blue have compressive stress. The inset is the schematic of the TPoS resonators with three interdigitated electrode fingers.

One class of lateral-mode piezoelectric resonators are known as contour-mode resonators (CMR) which comprise an AlN layer sandwiched between two metal layers. CMRs have been realized with various configurations and geometries with  $Q$ s up to a few thousand at 1GHz frequencies [37, 40, 41].

Lateral-mode resonators based on TPoS technology have also been reported with high quality factors and resonance frequencies in the range of tens of KHz to several GHz and exhibit superior power handling capability and robustness compared to CMRs [12, 15, 33].

### 2.3.2. Lateral-mode piezoelectric filters

Employing high quality factor (Q) lateral-mode piezoelectric resonators is a plausible solution for fabrication of multi-frequency filters on the same substrate. Taking advantage of high-Q resonators, filters with sharp roll-off and narrow bandwidth for direct channel selection can be realized [38, 39]. Such lateral-mode filters have been realized by electrical coupling of multiple resonators

Various filter configurations have been reported that utilize CMRs as their building blocks. Some of these topologies are pictured in Figure 5. Similar to FBAR technology, ladder topology has been used to realize high order filters. However, low IL values are achieved when filters are terminated with large resistances of a few  $K\Omega$  [40]. Another way to realize higher order systems is to electrically couple two or more resonators using the intrinsic capacitor of the CMRs [41]. The cascading of multiple two-port CMRs eliminates the need for coupling elements. IL of 2.3dB with fractional bandwidth as large as 0.5% have been reported for such third-order filter [42]. Another approach is the mechanical coupling of the resonators [43, 44]. The largest fractional bandwidth (up to 3%) were reported for an array of mechanically coupled CMRs [43]. Filters were reported to yield low IL with smaller termination resistance ( $300\Omega$ ) by stacking two layers of AlN and re-designing the electrode configuration [45].



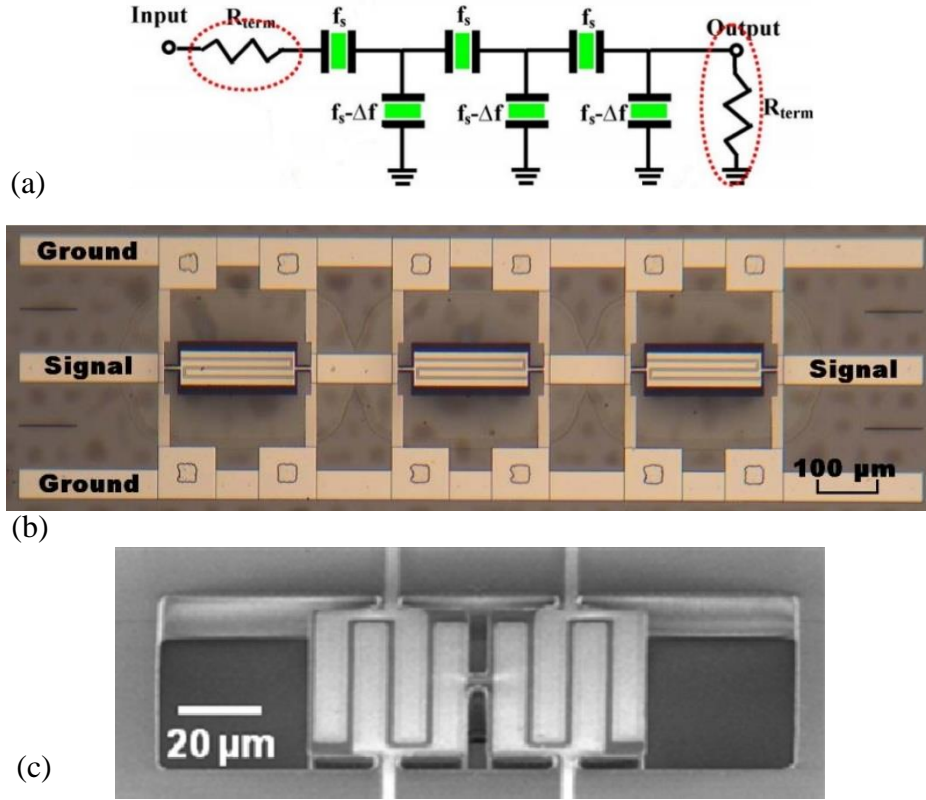


Figure 5: (a) Ladder filter topology [13], (b) higher order filter by electrical coupling of three contour-mode resonators [42, 46], and (c) second order filter by mechanical coupling of two contour-mode resonators [43].

But none of these filters have been reported to yield low insertion loss (IL) values ( $<5\text{dB}$ ) with the standard  $50\Omega$  termination mainly because of their large equivalent motional resistance compared to their thickness-mode counterparts. The channel-select filters will be placed between the antenna and the rest of the ICs, e.g. amplifier. The antennas generally have a small characteristic impedance of  $50\Omega$  or  $75\Omega$  in RF systems. To match the antenna to the filter, external matching networks have to be used which increases the power consumption. On the other hand, terminating the resonators with large impedances reduces the loaded quality factor which deteriorates the roll-off skirt of the filter as a consequence. Hence, methods to improve the IL of

the piezoelectric MEMS filters by design were sought. Reducing the IL becomes more challenging especially at high frequencies, where the feature sizes reduce considerably.

A sub-category of mechanically-coupled filters is a second order monolithic filter realized by coupling two different resonance modes of a single structure together. This type of filters was first introduced by Beaver for thickness-mode crystal devices [47, 48] and has been explored by others ever since [49, 50]. The lateral-mode monolithic filters have been formerly explored by Abdolvand *et al* [51, 52]. The latter class of filters are demonstrated with IL values as small as 3.7dB at ~900MHz in a 50 $\Omega$  network, which is the lowest value reported till present for the lateral-mode piezoelectric filters [11].

Another class of lateral-mode piezoelectric filters are monolithic filters. The idea behind a monolithic filter can be attributed to monolithic crystal filters (MCF). MCFs covering lower frequencies in the range of few to few hundred MHz, consist of a quartz crystal slab with two or more electrode plates on top and one larger plate at the bottom (Figure 6). Each section with one top electrode plate forms a separate resonator. The resonators are acoustically coupled via the elastic quartz medium [47]. The number of natural resonances of the structure define the zeros of the transmission plot when the output is short circuited. Thus, the degree of the system is equal to the number of the electrode plates on top.

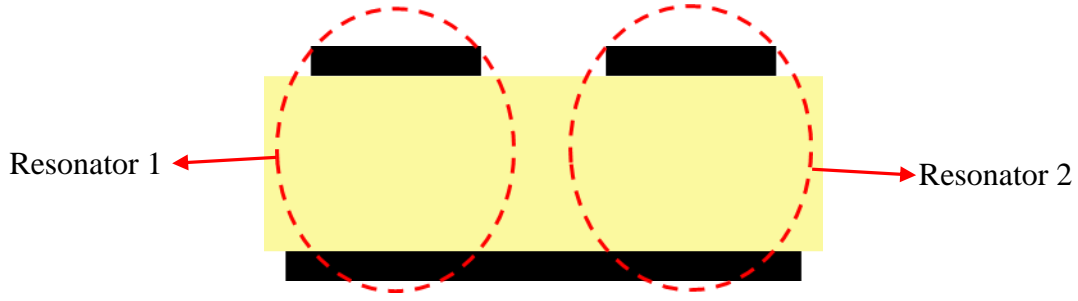


Figure 6: Cross-section of a monolithic crystal filter which consists of a quartz crystal plate sandwiched between a solid bottom metal plate and top electrodes.

The MEMS monolithic filters were first demonstrated on TPoS platform [51, 52], however the same concept can be applied to build purely piezoelectric filters perhaps with a larger bandwidth due to the larger effective electromechanical coupling but at the expense of poor power handling. A lateral-mode monolithic filter is realized by acoustic coupling of two resonance modes in a single resonant structure. The two-pole lateral-mode filters were designed for intermediate frequency (IF) bands and exhibit IL of about 7dB and fractional bandwidth as large as 0.2% [51]. The details of the design will be discussed in the chapter 5. The goal in this work is to improve the IL and to increase the bandwidth of lateral-mode monolithic TPoS filters to meet the requirements for mobile communication e.g. LTE bands. In addition, diamond is explored as the substrate for such TPoS devices.

The maximum achievable bandwidth in a piezoelectric filter is a function of the electromechanical coupling coefficient. For small coupling values and assuming very high  $Q$  for the resonator,  $k^2 = \frac{\pi^2}{4} \frac{f_s - f_p}{f_s}$ . For a second order ladder filter constituting two resonators with very high  $Q$ , the 3dB bandwidth is approximately equal to twice the difference between the series and parallel resonance frequencies:

$$BW_{3dB} = 2 * (f_p - f_s) \quad (26)$$

Hence, the maximum achievable fractional bandwidth is related to the electromechanical coupling coefficient by:

$$FBW_{3dB} = \frac{8}{\pi^2} k^2 \quad (27)$$

Using the values provided in [53] and equation (11), the piezoelectric coupling coefficient for lateral-mode piezoelectric resonators with AlN is approximately:

$$K^2 = \frac{e_{31}^2}{c_{11}^E \epsilon_{33}^S} = \frac{0.58^2}{8.5 * 8.85 * 10^{-12} * 3.45 * 10^{11}} = \sim 1.3\%$$

resulting in  $k^2$  of 1.28%. Thus, the maximum  $FBW_{3dB}$  would be 1.04% according to equation (27).

## **CHAPTER THREE: FABRICATION OF TPoS DEVICES**

This chapter discusses the work to optimize the properties of the ultrananocrystalline diamond (UNCD) films used to make the thin-film piezoelectric-on-diamond (TPoD) devices as well as the integration of high-quality AlN films on smooth (~1nm rms roughness) UNCD films achieved via wafer-scale polishing. After that the process for fabrication of TPoS devices on both UNCD and silicon-on-insulator (SOI) substrates will be explained.

### **3.1. Preparation of UNCD Films**

Materials with high energy density, low dissipation, high acoustic velocity, and low temperature coefficient of frequency are desired as the substrate for fabricating TPoS resonators. In recent years, diamond has gained much popularity in MEMS community essentially due to the advantages it offers. Some of these advantages are the high Young's modulus, bio-compatibility, low wear-rate, low dissipation properties, etc. [54]. Because of its high Young's modulus, diamond has a great potential to extend the frequency above the limits achievable by silicon (up to 2x increase in frequency) [13, 14, 15]. In this work, ultrananocrystalline diamond was used to build thin-film piezoelectric-on-diamond (TPoD) resonators. TPoD bulk-lateral-mode resonators with 80% higher frequency compared to the same devices fabricated on silicon have shown much promise in scaling the resonance frequency beyond the limits achievable by silicon [55, 33]. However, the orientation of the piezoelectric film is critical to retain the low insertion loss performance of the resonators. In the earlier work, a polished oxide layer was deposited on the nanocrystalline diamond substrate to promote the growth of a highly-oriented piezoelectric film

on the rough surface of the substrate [9]. As shown in SEMs of Figure 7, the surface of the ZnO deposited on oxide is much smoother than the one directly deposited on nanocrystalline diamond (NCD) leading to a better film quality and hence, a higher coupling coefficient. This oxide layer also helps reduce the TCF of the resonator [56]. However, this was the bottleneck for realization of very high frequency resonators since the presence of the oxide would significantly alter the mode shape and lower the quality factor and the frequency. According to the mode shapes in Figure 8, the resonance frequency has decreased by 15% and the displacement is distorted for the design with the buffer oxide layer [55].

In this work the surface roughness of diamond substrate is substantially reduced by depositing ultrananocrystalline diamond (UNCD) films with very small grain size followed by a standard chemical mechanical planarization (CMP) process. Such smooth surfaces allow for direct sputtering of metal/ piezoelectric/ metal heterostructures with a large coupling coefficient that enable monolithic integration of dispersed-frequency resonators.

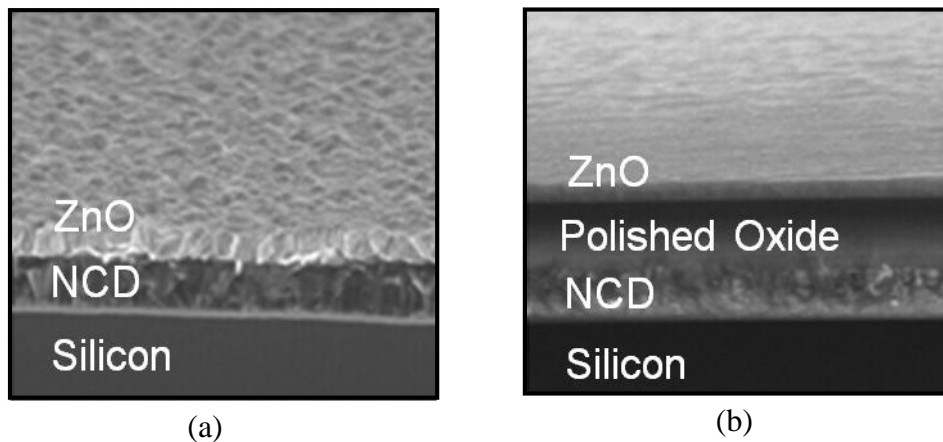


Figure 7: (a) The rough surface of ZnO directly sputtered on nanocrystalline diamond, (b) Polished oxide was deposited as a buffer layer before the deposition of ZnO in order to reduce the surface roughness [9].

The material acoustic velocity ( $\alpha$ ) is a function of Young's modulus (E) and mass density ( $\rho$ ) as follows:

$$\alpha = \sqrt{\frac{E}{\rho}} \quad (28)$$

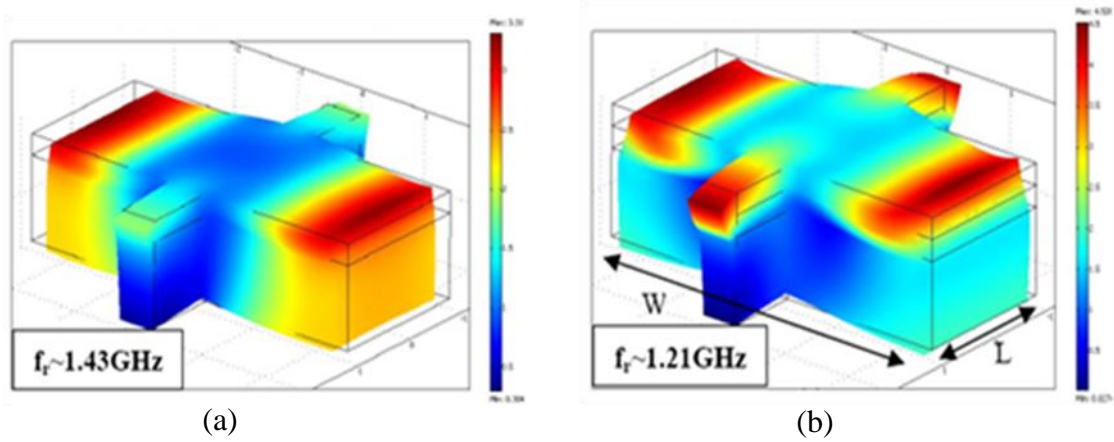


Figure 8: Effect of buffer oxide layer on the frequency and mode-shape of the lateral-extensional resonator [14]: (a) The mode-shape for the device without the buffer oxide layer, (b) Same design with an oxide layer in between the substrate and the piezoelectric layer.

The frequency of a piezoelectric resonator is directly proportional to  $\alpha$  of the substrate material. Standard UNCD films have Young's modulus from 650 GPa to 750 GPa, yielding up to 1.6 times increase in frequency compared to silicon-based devices designed with the same lateral dimensions. The challenge in increasing the modulus closer to the largest theoretical value possible ( $\sim 1200 \text{ GPa}$ ) is maintaining as small of a grain size as possible to retain the as-deposited smoothness of the material so that CMP processing is still capable of reducing the rms roughness to about 1 nm. It is also critical that the Young's modulus of the UNCD be consistently high and uniform across the wafer.

Three diamond substrates with different Young's modulus were prepared to fabricate TPoD resonators. UNCD was deposited using hot filament chemical vapor deposition (HFCVD) technique. The very small size of the UNCD grains warrant very smooth surfaces which allow for deposition of highly oriented piezoelectric thin films e. g. AlN. In order to increase the Young's modulus of the diamond films close to the theoretical values, the deposition temperature was increased from 660 °C to 810 °C by increasing the temperature of the filaments [33]. Figure 9 shows the dependency of the Young's modulus on the filament temperature as well as the film thickness. Increasing the deposition temperature also reduces the residual stress in the film from 300-400 MPa compressive to about 100 MPa tensile even for films as thick as 5-6 microns which is more desirable for deposition of the metal/ piezoelectric/ metal stack and the operation of TPoS devices. However, the average grain size of UNCD films grows at higher temperatures, resulting in films with rougher surfaces. The rms roughness was measured with atomic force microscope (AFM) to be around 60nm as presented in Figure 10-a. Such high rms roughness values make the integration of high quality AlN films on the diamond very challenging due to the crystallographic orientation disorder that occurs at the AlN/diamond interface. A highly disordered AlN film results in a very poor average piezoelectric coefficient and therefore an inferior IL for the resonators. This issue was resolved by adding an additional polishing step during which a more aggressive slurry and a greater applied force was used initially to bring the roughness down to about 15 nm, after which the conventional chemical mechanical polishing process was performed to further reduce the roughness to less than 1nm (Figure 10-b). The characteristics of the three UNCD wafers are listed in Table 1.



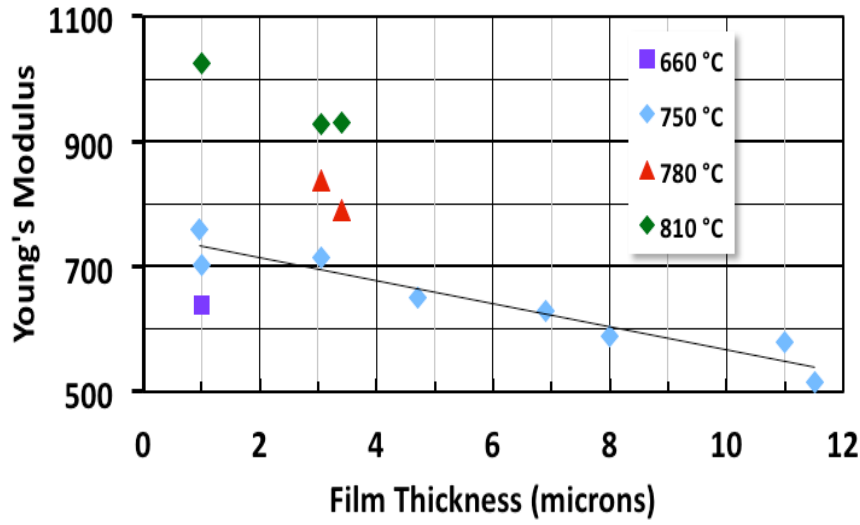


Figure 9: Dependency of the Young's modulus of the UNCD film on the deposition temperature.

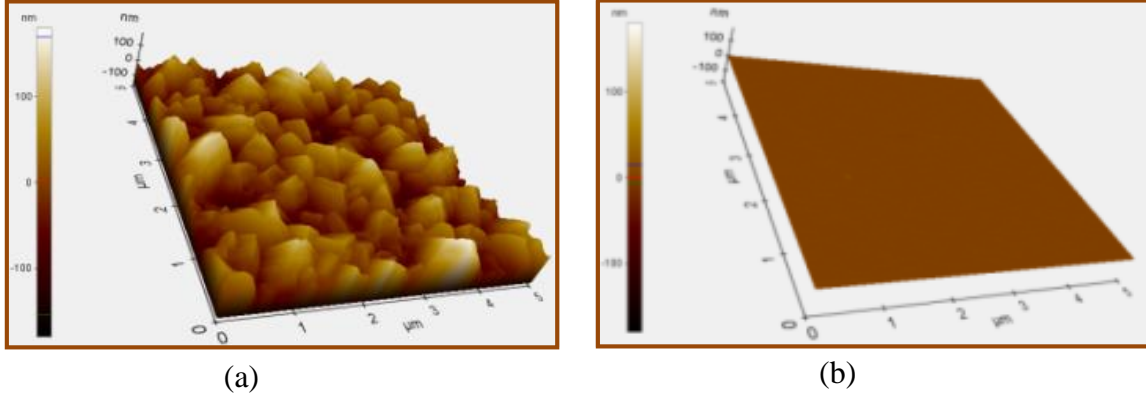


Figure 10: AFM image of high Young's modulus (950 GPa) diamond film surface (a) before and (b) after chemical mechanical polishing showing less than 1nm final rms roughness.

### 3.2. Deposition of AlN on Diamond Films

After UNCD deposition and polishing, the stack of metal/ piezoelectric/ metal was sputtered (Figure 11). AluminumNitride (AlN) is used as the piezoelectric layer due to superior process compatibility, relatively high acoustic velocity and high electrical resistivity. Molybdenum (Mo)

is chosen as the metal layer because it has a small lattice and thermal expansion coefficient mismatch with AlN in addition to low acoustic-loss. The AlN thickness varies from 0.5 $\mu$ m up to 1 $\mu$ m and Mo thickness is 100nm throughout this dissertation.

Table 1: Characteristics of the diamond films used for fabrication of TPoD resonators.

Wafer	UNCD	Young's	Surface	AlN	AlN
	Thickness	Modulus	Roughness	Thickness	FWHM
A	~3	491	0.4-0.5	0.5	4.07°
B	~3	650	0.4-0.5	0.5	3.05°
C	~3	933	1.0-1.8	0.5	3.19°

The two-dimensional X-ray diffraction (XRD) frames from AlN film deposited on both polished and unpolished UNCD is illustrated in Figure 12 for comparison. If the grains are more aligned in a certain direction, the diffraction will be denser in that specific angle thus, the associated X-ray rings would be brighter. The AlN deposited on polished diamond film exhibits a higher intensity at specific values of chi which confirms the existence of highly textured AlN. Figure 13 shows a SEM from the smooth surface of the AlN sputtered on polished UNCD compared to the rough surface of ZnO deposited on NCD in Figure 27. Figure 14 represents the X-ray rocking curve of the AlN film on polished UNCD with a full-width half maximum (FWHM) of about 3 degrees. The quality of the film is very close to that of the c-axis aligned AlN deposited on polished single crystal silicon substrates for which the typical FWHM is in the range of 2.0°-2.5°.

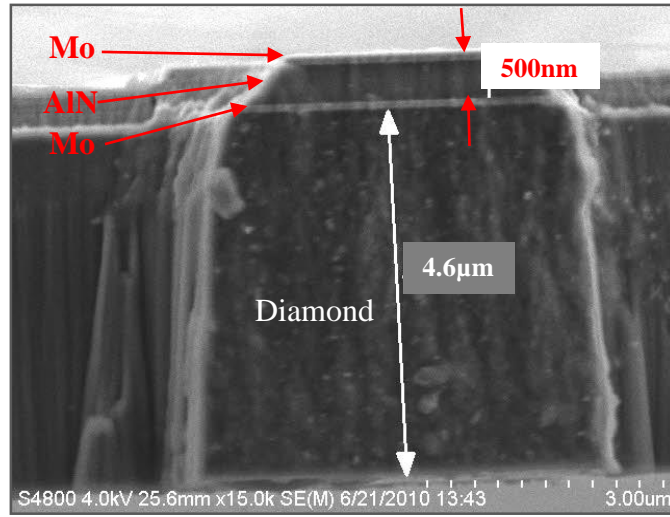


Figure 11: Cross-section of a broken device showing the stack of Mo/AlN/Mo directly sputtered on UNCD.

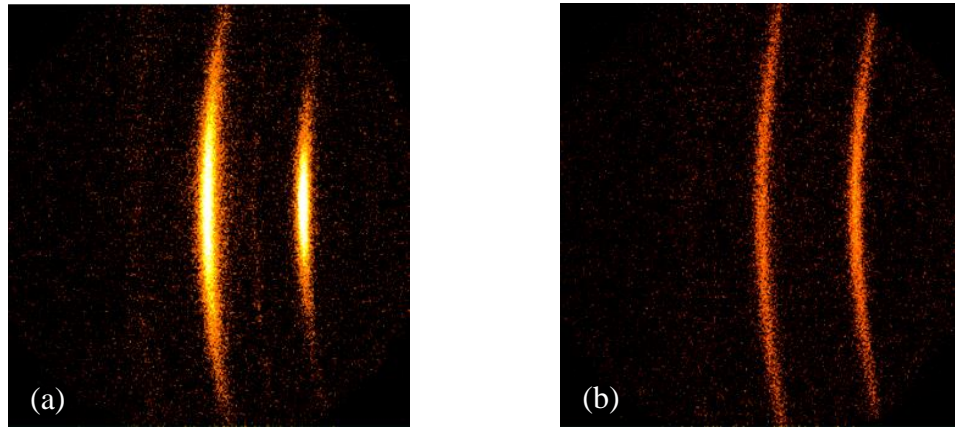


Figure 12: Two-dimensional x-ray diffraction frames collected from a 500nm AlN film deposited directly on polished (a) and unpolished (b) ultrananocrystalline diamond films.

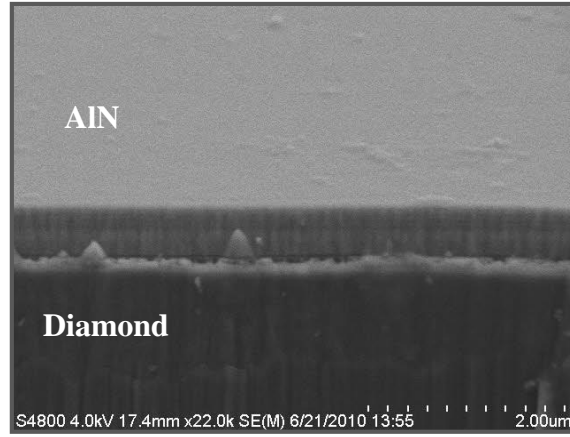


Figure 13: SEM of the smooth surface of AluminumNitride directly sputtered on polished UNCD film.

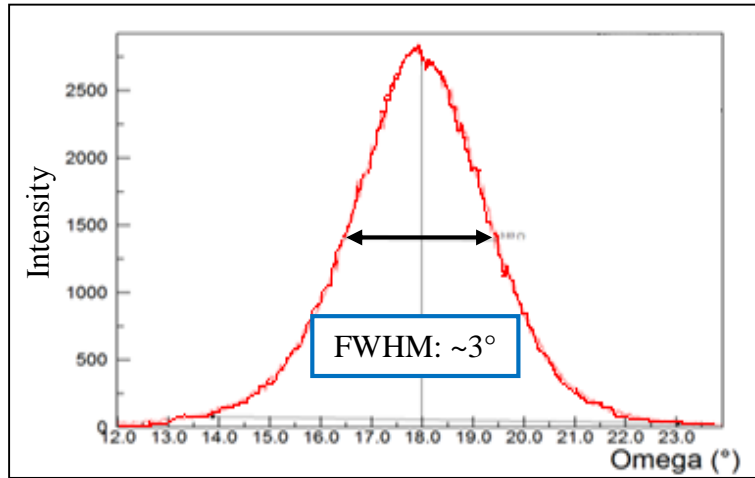


Figure 14: Rocking curve of the AlN film deposited on polished UNCD film with full-width half-maximum of 3°.

### 3.3. Fabrication Process

Materials with high energy density, low dissipation, high acoustic velocity, and low temperature coefficient of elastic moduli are desired as the substrate for fabricating TPoS resonators such as single crystalline silicon or diamond. Silicon as the starting substrate for

fabrication of integrated circuits (IC) is cheap and widely available. The high quality factor of silicon enables realizing resonant structures with very good performance. On the other hand, some of the unique advantages of diamond are the highest Young's modulus in nature, very low wear-rate, and low acoustic dissipation [54]. Because of its high  $E$ , diamond has a great potential to extend the frequency of MEMS resonators beyond the limits achievable by silicon [55, 56, 57, 58, 59]. Also, the Young's modulus of diamond is less dependent on temperature compared to silicon resulting in resonant devices with a smaller TCF. Both substrates were utilized to fabricate high frequency TPOs devices in this work.

The commonly used piezoelectric materials are Zinc oxide (ZnO), Lead zirconate titanate (PZT), Aluminumnitride (AlN), and Lithium niobate (LiNbO<sub>3</sub>). Despite having very high piezoelectric coefficient, both PZT and LiNbO<sub>3</sub> are cumbersome to fabricate and are not compatible with CMOS process. ZnO on the other hand has a lower dielectric constant compared to AlN which results in leakage currents especially at higher voltages. AlN is used as the piezoelectric layer due to superior process compatibility, relatively high acoustic velocity and high electrical resistivity. Molybdenum (Mo) is chosen as the metal layer because of the small lattice and thermal expansion coefficient mismatch with AlN in addition to low acoustic-loss.

### 3.3.1. Silicon devices

Silicon-on-insulator (SOI) substrates were used to fabricate devices on silicon. The fabrication process is pictured in Figure 15. The bottom Mo layer is first sputtered on the silicon device layer and patterned by dry-etching in  $SF_6$  and  $O_2$  plasma with a photoresist mask to partially remove the metal from underneath the pads in order to reduce parasitic capacitances (Figure 15-b). The

piezoelectric and the top metal layers are respectively sputtered on top as depicted in Figure 15-c. The electrodes are formed by patterning the top metal layer the same way as the bottom metal layer (Figure 15-d). AlN is wet-etched in a Tetramethylammonium hydroxide (TMAH) solution at 80 °C using a  $SiO_2$  mask to gain access to the bottom metal which serves as the ground plate (Figure 15-e). A layer of gold (about 100nm) is then deposited on the contact pads, both signal and ground, to reduce the ohmic losses (Figure 15-f). However, gold alone can undergo de-lamination; therefore to improve the adhesion of the gold layer to Mo, a very thin layer of Chromium (Cr) in the order of 10nm is deposited prior to the deposition of the gold layer. The Cr/Au layers can be either deposited using sputtering or evaporation techniques. Since these layers are patterned later by lift-off method, the evaporation technique is preferred due to more directional deposition and thus, less sidewall coverage. After deposition and patterning all the layers, trenches are etched all around to form the device structure.  $SiO_2$  is used as the mask due to its lower etch rate compared to photoresist. First, AlN is etched in  $Cl_2$  plasma in an inductively-coupled plasma (ICP) etcher. Next, the silicon device layer is etched down to the box oxide layer in a Bosch process using a low frequency generator to achieve minimal scalloping. In order to release the devices, the handle silicon is etched all the way through from the backside in a Bosch process (Figure 15-h). The final release step involves etching away the box and mask oxide layers in a buffered oxide etchant (BOE) as shown in Figure 15-i.

### 3.3.2. Diamond devices

The fabrication process for diamond devices is very similar to the process for fabricating devices on SOI substrates. The schematic of the process flow is depicted in Figure 16. As

mentioned earlier in this chapter, the UNCD film is directly deposited on the polished surface of a silicon wafer, followed by deposition of the bottom metal layer. The Mo/AlN/Mo stack and also the Cr/Au layers are deposited and patterned the same way as was explained for devices on SOI substrate (Figure 16a-d). After etching the AlN to form the trenches around the device structure, diamond is then dry-etched in  $O_2/CF_4$  plasma.  $CF_4$  was added to etch away the micromask formed around the trenches as a result of oxide mask getting sputtered in the plasma (Figure 16-e). The final step is releasing devices by dry etching the handle silicon from the backside (Figure 16-f).

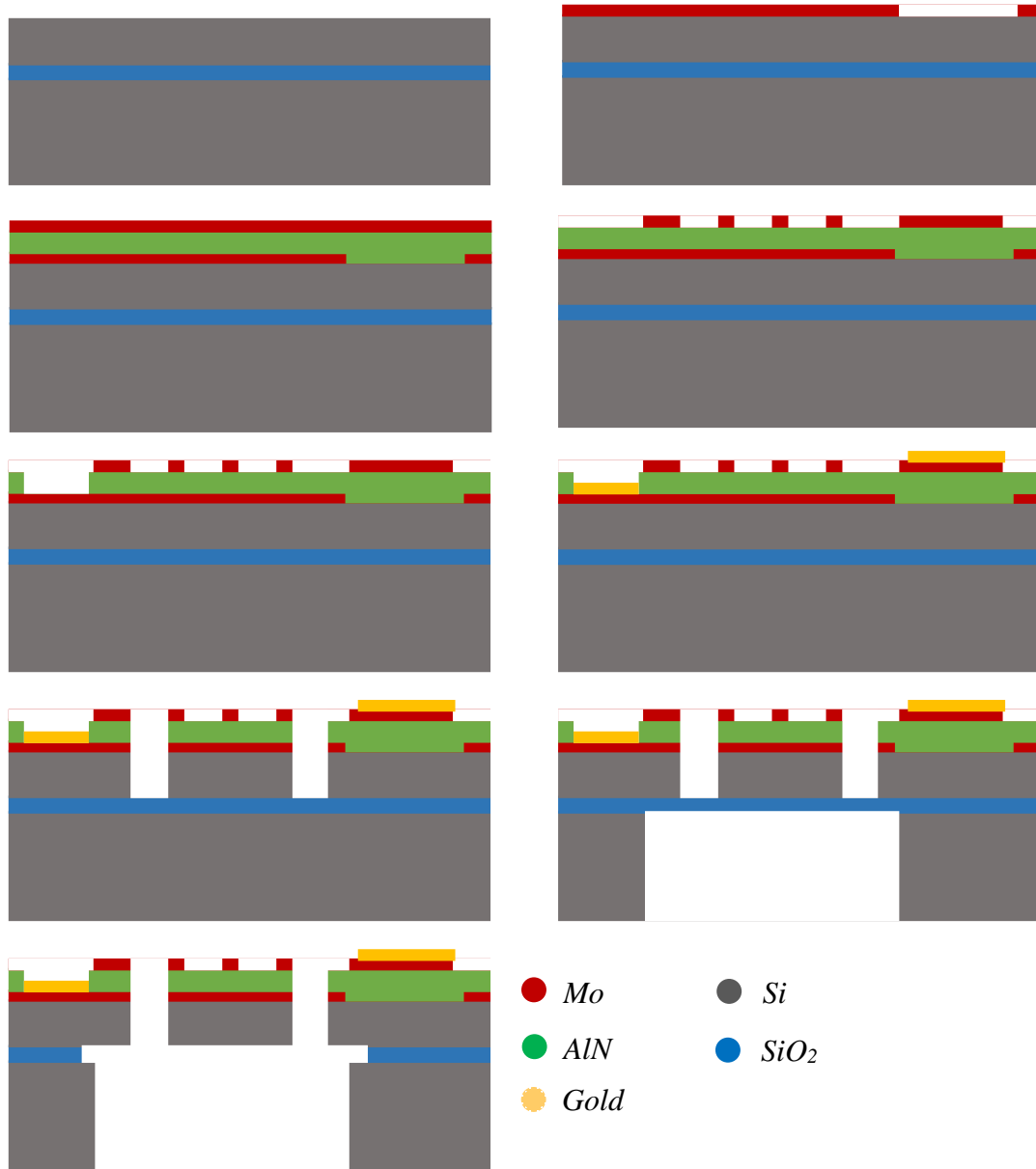


Figure 15: Fabrication process flow: (a) Silicon-on-insulator substrate, (b) Deposition and patterning the bottom metal layer, (c) Deposition of AlN and top metal layers, (d) Patterning Top metal to form the electrodes, (e) Wet-etching the AlN to gain access to the bottom metal, (f) Sputtering gold on the contact areas, (g) Etching of the stack, AlN in  $\text{Cl}_2$  and silicon in  $\text{SF}_6$  respectively, (h) Etching the handle silicon from the backside, (i) Final release of the structure by wet-etching the box oxide layer.



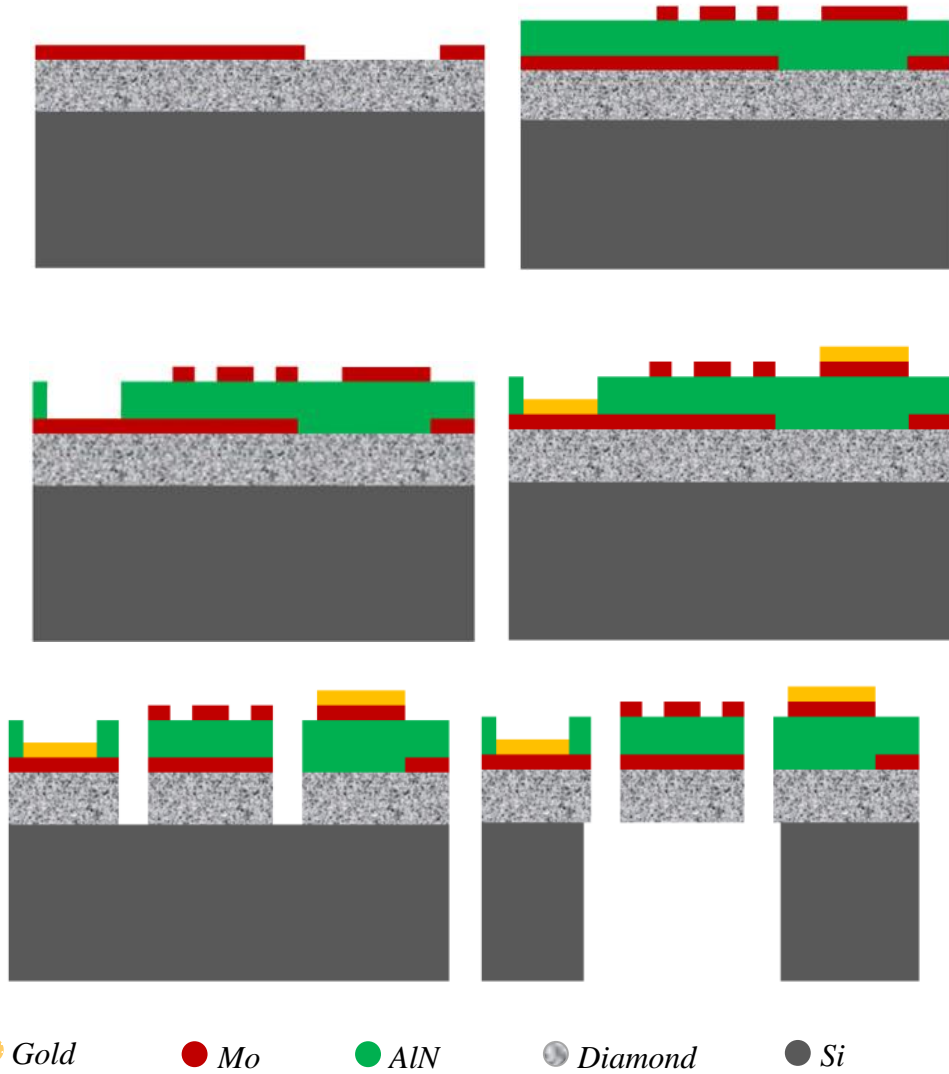


Figure 16: Fabrication process flow: (a) Patterning the bottom metal layer, (b) Deposition of AlN and top metal layer, followed by patterning the top metal, (c) Wet-etching the AlN to gain access to the bottom metal, (d) Sputtering gold on the contact areas, (e) Etching the stack (f) followed by releasing the device by etching the handle silicon from the backside.

## CHAPTER FOUR: SUBSTRATE CHARACTERIZATION

### 4.1. Characterizing UNCD Films

To characterize the quality of the UNCD films, a multi-tethered 21<sup>st</sup> order resonator was fabricated on the three diamond substrates mentioned in Table 1 of section 3.1. and also on an SOI substrate. The transmission responses are plotted in Figure 17. The UNCD thickness is  $\sim 3\mu\text{m}$  for all the three substrates whereas the device layer is  $5\mu\text{m}$  on the SOI substrate. Considering the  $f \cdot Q$  product as the figure of merit for resonators, devices fabricated on diamond show up to 1.5 times improvement compared to the device fabricated on silicon while having a similar  $Q$  and IL. Hence, UNCD substrates can be utilized to attain frequencies beyond the limits achievable by silicon without sacrificing the performance of lateral-mode TPoS devices.

### 4.2. Nonlinearity and Power Handling

The far-from-carrier phase noise in an oscillator is inversely proportional to the carrier power. Thus, it is desired to operate the oscillator at high power levels. Recently, stable oscillators have been reported that drive the resonator into the nonlinear operation range [60, 61]. Preliminary results show that the oscillator noise continues to improve even in the resonator's nonlinear range of operation [61].

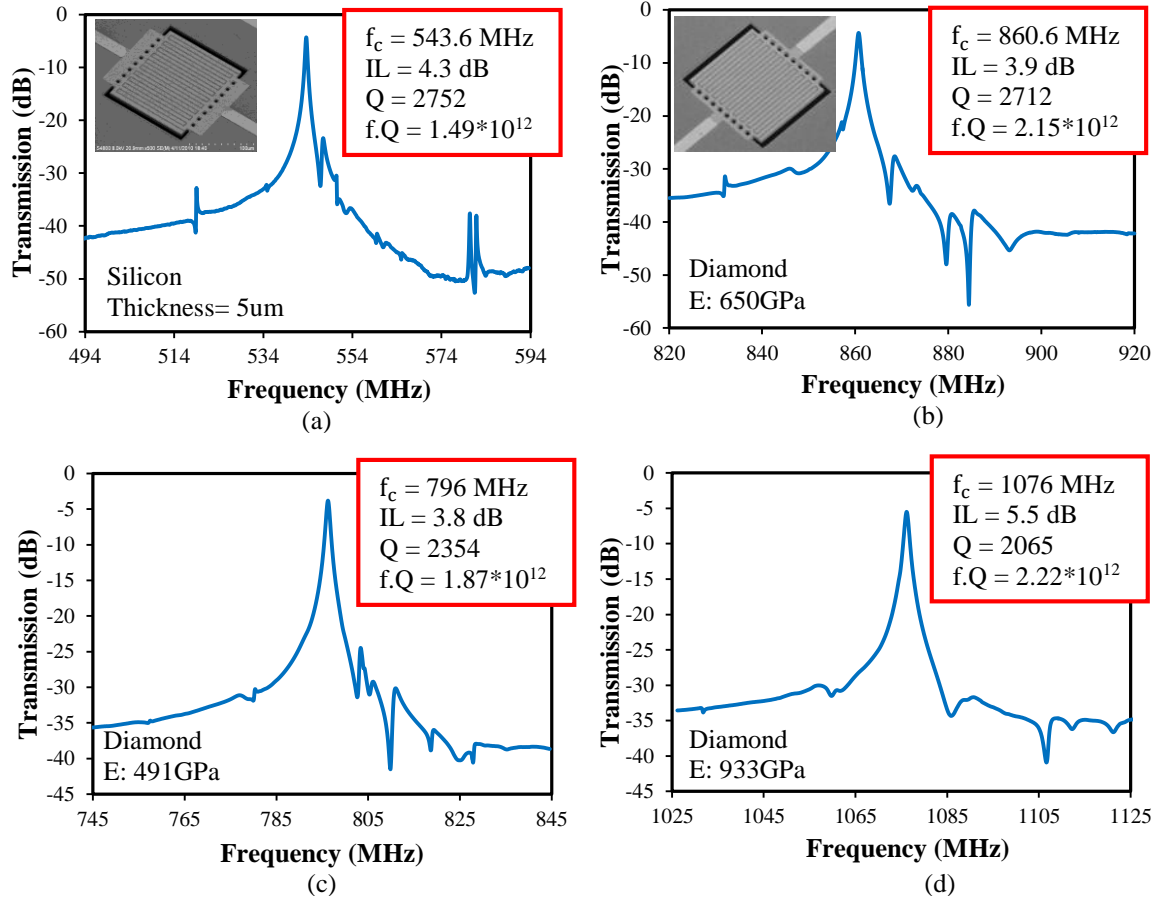


Figure 17: Frequency response of a multi-tethered 21<sup>st</sup> order TPoS resonator fabricated on silicon (a), UNCD with  $E$  of 650 GPa (b), 491 GPa (c), and 933 GPa (d). The insets on (a) and (b) show the SEM of the resonators fabricated on SOI and UNCD respectively.

The maximum energy density of micro-resonators at bifurcation has been studied previously. Kajaakari *et al.* present a relatively accurate method for calculating the energy density of micro-resonators at bifurcation but it requires finding the nonlinear spring constants of the substrate material [62, 63]. Utilization of the aforementioned method becomes more complicated for thin-film piezoelectric-on-substrate (TPoS) devices with a stack of different materials which would involve the complexities related to material boundaries. Conventionally, the power handling capability of resonators has been evaluated by calculating the critical power from  $P_c = R_m i_c^2$

where  $R_m$  is the motional resistance and  $i_c$  is the critical current passing through the mechanical branch of the resonator electrical equivalent circuit [64]. However, it is our understanding that this equation expresses the dissipated power of the resonator rather than the stored energy in the resonant structure. Therefore, it may not be the best figure for comparing the bifurcation or fracture limits of the resonators considering that these limits are the result of certain vibration amplitudes and consequently certain amount of energy stored in the resonant structure.

In this work, a method that does not deal with the material properties, but rather determines the energy density of the device through electrical measurement was sought. The presented method takes advantage of the measured S-parameters of the device and resonator modeling using ADS software.

The primary focus of this work is to compare the critical and maximum energy density of resonators on silicon and diamond substrates. The platform chosen for this work is the lateral-extensional TPoS resonators fabricated on both silicon and diamond wafers.

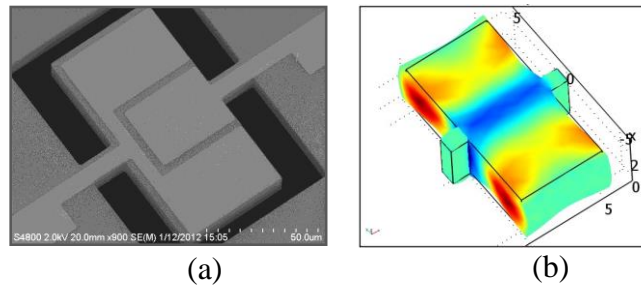


Figure 18: (a) SEM and (b) mode-shape showing the stress field of a third-order harmonic TPoS resonator.

Piezoelectrically-transduced resonators offer larger electromechanical coupling coefficient relative to that of electrostatic resonators, which results in achieving low-insertion loss resonators

and filters [9, 10]. TPoS resonators are a subcategory of piezoelectric resonators which exhibit superior power handling and high quality factors concurrently [15]. This makes the TPoS technology a candidate for implementing very stable oscillators.

Employing the presented method for measuring the energy density, silicon and diamond are compared in terms of energy storage capability both at bifurcation and fracture limits. Although, TPoS devices were chosen as the platform for this work, our proposed method can be applied to any device technology.

#### 4.2.1. Quantifying power handling

A method is presented to measure the stored energy of the resonator at different drive levels. All the S-parameter measurements in this work were performed using an Agilent E8358A PNA network analyzer, a pair of GSG probes, and an RF amplifier while the device under test (DUT) was terminated with the internal  $50\Omega$  impedances of the amplifier and the network analyzer at the input and output ports respectively. Prior to measurements, short-open-load-thru (SOLT) calibration was carried out on a reference substrate to calibrate the measurement setup including the amplifier. All the measurements are performed at atmospheric pressure and ambient temperature. For the energy density measurements, the input power of the resonator was increased from 0dBm by increments of 0.5dBm to the point that hysteresis was observed in the transmission response and beyond that till the resonator mechanically failed and broke.

The measured S-parameters are then fed to a two-port network in ADS software. The utilized model is pictured in Figure 19. The two  $50\Omega$  resistors represent the output resistance of the amplifier and the termination on the network analyzer. The amplitude of the voltage source is

determined by the power set on the network analyzer plus +25dB, which is the gain of the amplifier.

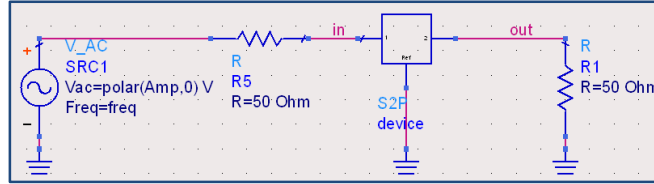


Figure 19: ADS model to measure the stored energy and dissipated power of the resonator.

The ingoing ( $I_{in}$ ) and outgoing ( $I_{out}$ ) currents of the two-port device are then extracted at the resonance frequency using this model. The power delivered to the system including the device and the  $50\Omega$  load impedance ( $R_1$ ) is calculated using equation (1) where  $V_{in}$  is the voltage amplitude at the input of the device and  $\theta$  is the phase difference between the  $I_{in}$  and  $V_{in}$  determined by the impedance of the system at resonance.

$$P_{d,total} = V_{in}I_{in}\cos(\theta) \quad (29)$$

This value includes the power dissipated by the device ( $P_d$ ) and the load. The dissipated power by the  $50\Omega$  load ( $P_{d,load}$ ) is calculated using  $I_{out}$ , which is the outgoing current of the device. Thus, the power dissipated by the resonator is:

$$P_d = P_{d,total} - P_{d,load} \quad (30)$$

Next, using the definition of the quality factor, the stored energy of the device can be calculated (3). Note that to calculate the stored energy, the unloaded quality factor ( $Q_{ul}$ ) of the resonator has to be used. The approximate value of  $Q_{ul}$  is calculated by taking advantage of the simplified Butterworth Van Dyke (BVD) model of the resonator (Figure 20) and equation (4).

$$Q = 2\pi * \frac{\text{Stored Energy}}{\text{Energy dissipated per cycle}} = 2\pi f_r * \frac{\text{Stored Energy}}{\text{Power Loss}} \quad (31)$$

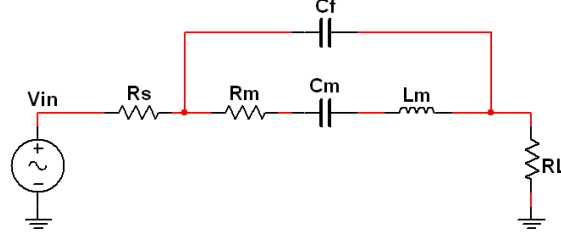


Figure 20: Simplified equivalent BVD model for a typical resonator.

Therefore,

$$Q_{\text{unloaded}} = Q_{\text{loaded}} * \frac{R_s + R_m + R_L}{R_m} \quad (32)$$

To make a fair comparison between different resonators, the energy density or in other words the stored energy per unit volume is then calculated assuming uniform energy distribution in the bulk of the resonator. The results are compiled in the following sections for critical and fracture energy densities of both silicon and diamond resonators.

#### 4.2.2. Silicon versus diamond

In this section, lateral-extensional thin-film piezoelectric-on-substrate (TPoS) resonators, fabricated on both silicon and diamond, are driven beyond their bifurcation point in order to study the maximum allowable energy density before the resonator fractures. The average measured critical energy density of the resonator (the stored energy at bifurcation) on silicon substrate is  $\sim 5.2 \times 10^5 \text{ J/m}^3$  for a specific resonator design while it is  $\sim 2.7 \times 10^5 \text{ J/m}^3$  for a similar device fabricated on ultrananocrystalline diamond. On the other hand, the resonator on diamond withstands energy densities more than 2 times larger than the resonator on silicon before devices fracture and fail

mechanically.

### Comparison of Energy Densities at Bifurcation

The transmission responses of the resonators were measured at different input power levels. The critical stored energy ( $E_{stored,c}$ ) density is measured at the input power level right before the transmission response exhibits frequency hysteresis (bifurcation point). This hysteresis is demonstrated in Figure 21 for a typical resonator on diamond substrate. For both TPoS devices fabricated on silicon and diamond frequency softening was observed as the input power was increased. Measured responses at different power levels are plotted in Figure 22 and Figure 23. At power levels well above the critical applied power the transmission plot of the resonator fabricated on silicon becomes unstable as evident for the forward frequency sweep at 24.5dBm in Figure 22. This behavior is not yet clearly understood and requires further investigation.

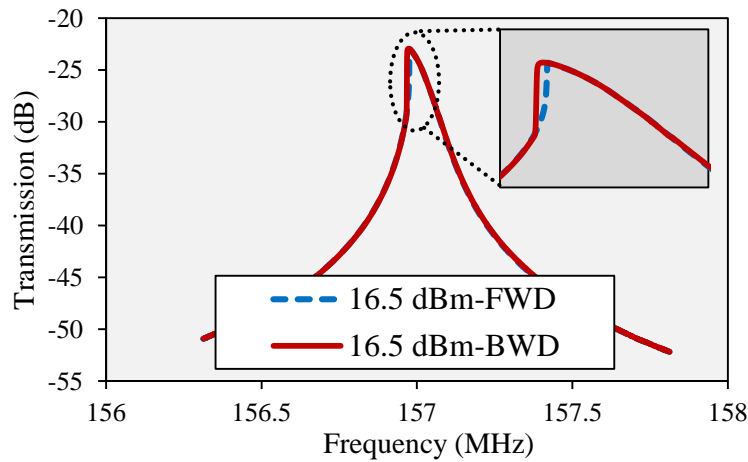


Figure 21: Transmission response of a typical resonator on diamond substrate at 16.5dBm applied power showing hysteresis for forward and backward frequency sweeps.



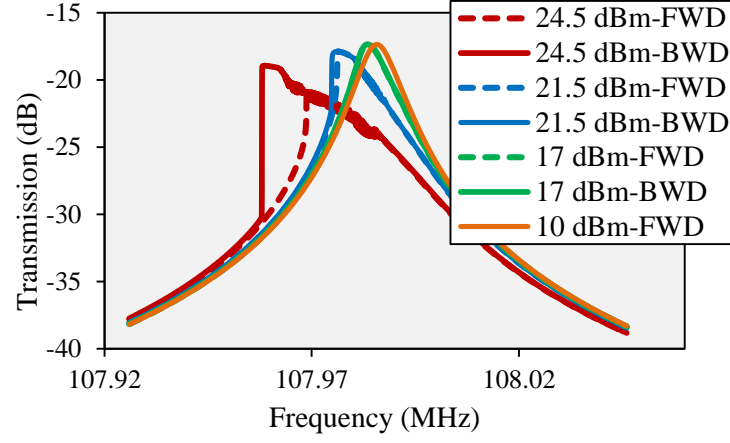


Figure 22: Transmission responses of a typical resonator on silicon showing hysteresis at power levels above the bifurcation.

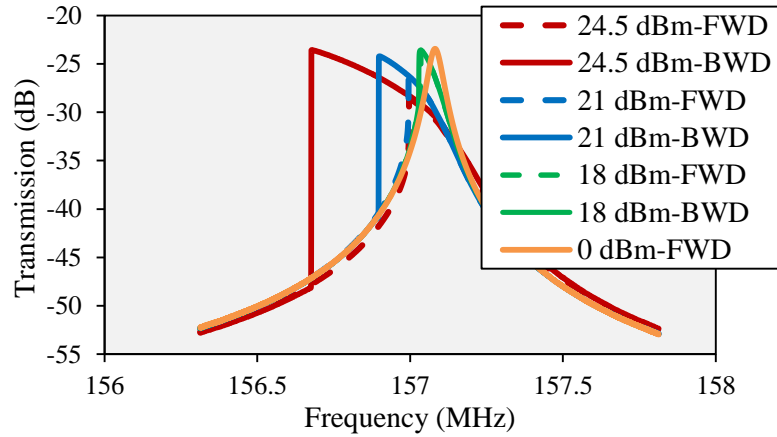


Figure 23: Transmission responses of a typical resonator on diamond showing hysteresis at power levels above the bifurcation.

The extracted experimental values of the stored energy and dissipated power densities for an average device on silicon and diamond are listed in Table 2 for comparison. Although, the lateral dimensions of the two devices are similar, the resonance frequency of the resonator fabricated on diamond is about 45% higher than that of the resonator fabricated on silicon due to higher Young's modulus of diamond. However, the quality factor of the one on silicon is much higher mainly due

to the thicker substrate. The aforementioned resonator shows hysteresis at  $\sim 7$  dBm higher power levels. Even though,  $E_{Stored,c}$  of the resonator on silicon is 15 times larger at hysteresis, the stored energy densities are fairly close. These values can be compared to the values reported in [62] for silicon BAW resonators ( $2.1 \times 10^6 \text{ J/m}^3$ ). Although,  $P_d$  for the resonator on silicon is lower,  $E_{Stored,c}$  is larger than that of the resonator fabricated on diamond which highlights the contrast between  $P_d$  and the stored energy. The stored energy density has been measured for various resonators on both substrates at bifurcation and the statistical data is presented in Figure 24. On average, the resonators fabricated on silicon exhibit energy densities 1.9 times higher than the resonators fabricated on diamond.

Table 2: Experimental results of two typical TPoS devices fabricated on diamond and silicon right before hysteresis.

Substrate	Dimensions (W×L×T)	Resonance Frequency (MHz)	$Q_{unloaded}$	Motional resistance ( $\Omega$ )	$P_{applied}$ (dBm)	$I_{in}$ (mA)	$I_{out}$ (mA)	$P_d$ (mW)	$P_d/V$ ( $\mu\text{W}/\mu\text{m}^3$ )	$E_{stored,c}$ (nJ)	$E_{stored,c}/V$ ( $\times 10^6 \text{ J/m}^3$ )
Silicon	115×58×15	109	9875	913	23	9.7	3.7	3.36	0.03	49	<b>0.47</b>
Diamond	108×54×1.5	158	2637	1565	16	5.9	1.2	1.25	0.1	3.3	<b>0.28</b>

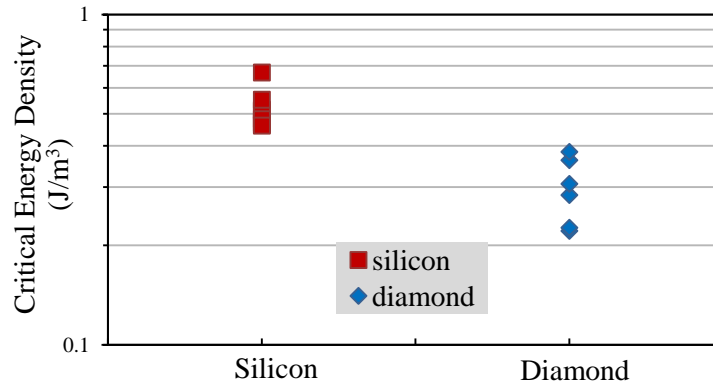


Figure 24: Statistical data showing the critical energy density of various resonators measured on silicon and diamond substrates.

## Comparison of Energy Densities at Fracture

Devices were driven beyond their bifurcation point and deep into the hysteresis by further increasing the applied power. As the induced stress in the resonator reaches the fracture limits of the material by virtue of the large electric fields applied to the piezoelectric layer, the resonators fracture and break. As displayed in the SEMs of Figure 25, the fracture is initiated along the corner of the tether where the stress is maximum (refer to Figure 18-b). The stored energy density of the resonator is measured right before the fracture and is defined as the fracture energy ( $E_{Stored,f}$ ) density. The experimental results for two average devices on silicon and diamond are also listed in Table 3 for comparison. The  $E_{Stored,f}$  was measured for various resonators on both substrates and the statistical data is presented in Figure 26. The resonators fabricated on diamond exhibit fracture energy densities about 2x higher than the resonators fabricated on silicon.

Table 3: Experimental results of two typical TPoS devices fabricated on diamond and silicon right before fracture.

Substrate	Dimensions (W×L×T)	Resonance Frequency (MHz)	$Q_{unloaded}$	Motional resistance ( $\Omega$ )	$P_{applied}$ (dBm)	$I_{in}$ (mA)	$I_{out}$ (mA)	$P_d$ (mW)	$P_d/V$ ( $\mu W/\mu m^3$ )	$E_{stored}$ (nJ)	$E_{stored}/V$ ( $\times 10^6 J/m^3$ )
Silicon	115×58×15	109	9875	913	26	13	4.6	8.8	0.08	128	<b>1.2</b>
Diamond	108×54×1.5	158	2637	1565	27	24	2.3	13.5	1.16	36	<b>3.1</b>

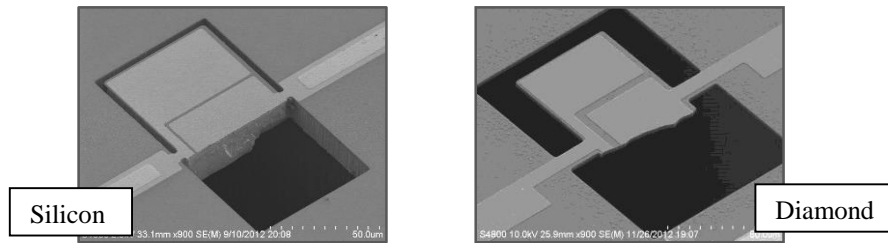


Figure 25: SEM of the two typical resonators on silicon and diamond after fracture.

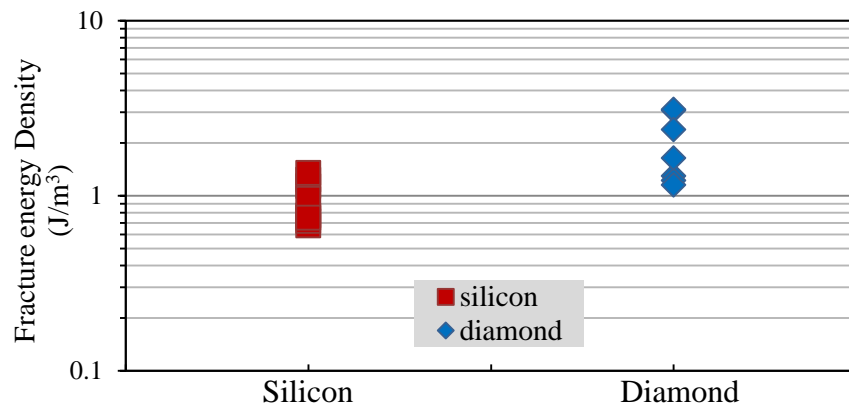


Figure 26: Statistical data showing the fracture energy density of various resonators measured on silicon and diamond substrates.

## CHAPTER FIVE: NARROW-BAND TPoS FILTERS

The first part of this chapter is dedicated to study the performance optimization of lateral-mode monolithic filters. Finite element model (FEM) simulations are carried out to investigate the effect of different design parameters on the performance of the monolithic filters. Simulation results are compared against the actual measurement results to validate the FEM simulations. The best results are presented. A few novel designs with larger bandwidth are presented in the second part of this chapter.

### 5.1. Monolithic TPoS Filter

This section discusses the design procedure of the lateral-mode monolithic filters and describes the effect of different geometric features and physical parameters on the performance of the filter with the focus being on minimizing the IL of such filters while increasing the bandwidth. The discussions are then evaluated by the measurement results. IL values as low as 3.7dB and bandwidth as large as 1% are demonstrated. Furthermore, the nonlinear behavior of these filters is examined for input powers up to +35dBm.

#### 5.1.1. Design concept

The monolithic filters described in this work are two-pole filters based on the acoustic coupling of two resonance modes in a single resonant structure. The two resonance modes utilized to build the filters are the higher harmonic lateral- modes of a rectangular structure. In order for the two modes to couple together and increase the order of the system, there needs to be a  $180^\circ$  phase difference between them. A rectangular structure was simulated in a commercial simulation

software package, COMSOL<sup>®</sup>, to look for the mode shapes of interest. The strain field and the exaggerated volume deformation for the two 7<sup>th</sup> harmonic modes are displayed in Figure 27. Note that for both of the mode-shapes the acoustic wave propagates along the width of the slab. The areas in the same shades of color are under the same strain polarity. In order to excite and sense these modes of vibration, an overlaying piezoelectric film sandwiched between patterned metal layers can be employed.

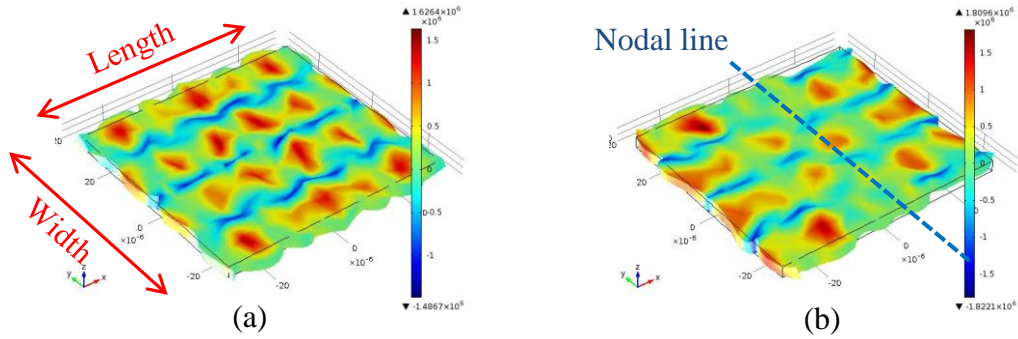


Figure 27: Mode shapes for a 7<sup>th</sup> order harmonic monolithic filter simulated in COMSOL<sup>®</sup> showing the strain fields for the in-phase mode (a) and the out-of-phase mode (b). The out-of-phase mode has a zero-displacement line (nodal line) at the middle of the length.

The proposed electrode configuration that enables excitation of both modes is presented in Figure 28. For the in-phase mode, the electrodes across from each other are covering areas with the same strain polarity as opposed to the out-of-phase mode. As can be seen, for the 7<sup>th</sup> harmonic filter of Figure 28 each of the input and output ports consists of four electrode fingers.

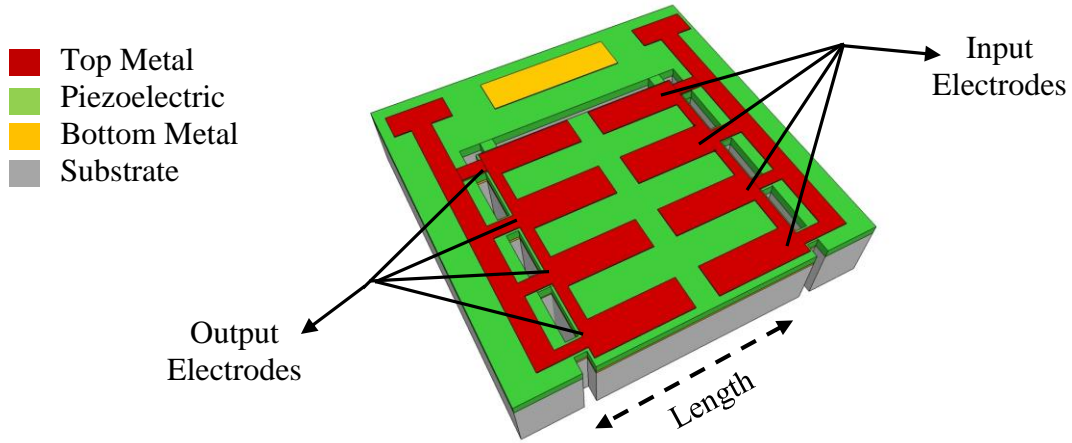


Figure 28: The schematic of a two-port multi-tethered 7<sup>th</sup> harmonic monolithic filter showing the electrode pattern.

It is noteworthy that the resonant structure in our design is anchored to the substrate from several modal (zero-displacement) nodes. It has been previously shown that multi-tethering of the TPoS resonators improves the Q, IL, and power handling while reducing the spurious modes some of which could be very close to the target resonance [12, 38, 65]. Since the operation concept of the monolithic filters is similar to that of TPoS resonators, the same technique is adopted here.

#### 5.1.2. FEM model

The frequency response of the TPoS filters can be predicted by finite element analysis in COMSOL. The developed model incorporates a piezoelectric layer, which couples the stress/strain and the electric fields and includes the support loss as the dominant source of energy loss as explained in chapter two [66]. The support loss which represents part of the acoustic energy radiated from the resonator out to the substrate through the tethers is implemented by embedding a perfect matching layer (PML) in the model [66]. The PML absorbs all the acoustic energy that impinges upon it at the frequency of interest. Diamond is used as the substrate for the simulations

presented in the following and its thickness is set to  $3\mu\text{m}$  and the Young's modulus set to  $650\text{GPa}$ , which is the actual Young's modulus of one of the diamond wafers used for fabricating the thin-film piezoelectric-on-diamond devices. The electrodes are included as a lossless material with finite electrical conductivity to apply the input voltage and extract the output current. Both the input and output ports are terminated with  $50\Omega$  in the model. Instead of adding a thin bottom metal layer which adds complexity and dramatically increases the mesh size, the bottom face of the piezoelectric layer is grounded. Figure 29 shows the model build in COMSOL along with the simulated mode shapes for the in-phase and out-of-phase resonances of a  $60\mu\text{m}$  long 7<sup>th</sup> harmonic filter with four tethers on each side. Careful observation of the mode shapes reveals that at each resonance mode, a portion of the acoustic wave radiates into the surrounding substrate through tethers and creates a relatively small strain field in the substrate.

Even though all the loss mechanisms are not fully captured in this model, the resulting frequency response helps to estimate the center frequency, study the relative effect of device dimensions on filter specifications such as loss and bandwidth, and predict the spurious modes. The simulated frequency response of the model is plotted in Figure 30. A spurious mode close to the in-phase mode is indicated on the plot. Such spurs which are intrinsic to any resonant structure have to be suppressed by design. Adding more tethers to the structure is one way to eliminate the spurs, while it also increases the quality factor of the resonator [12].



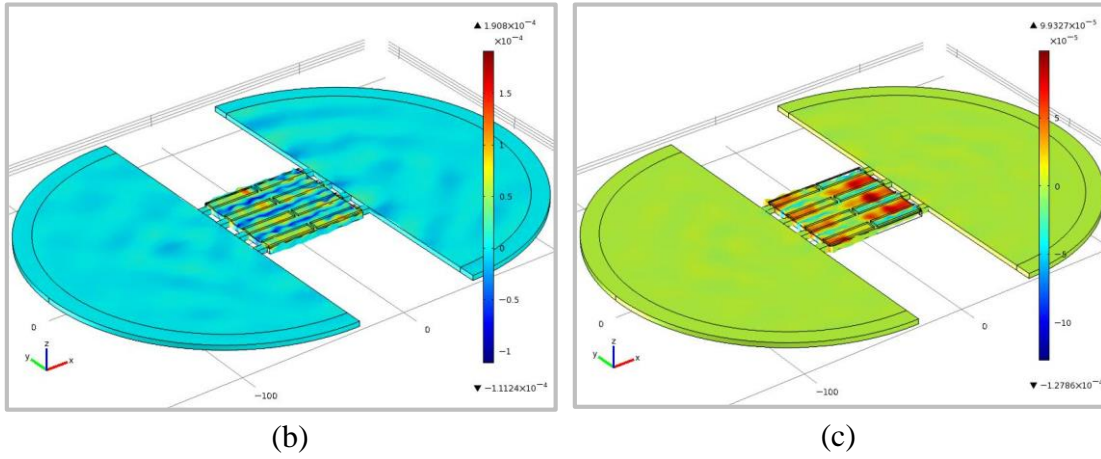
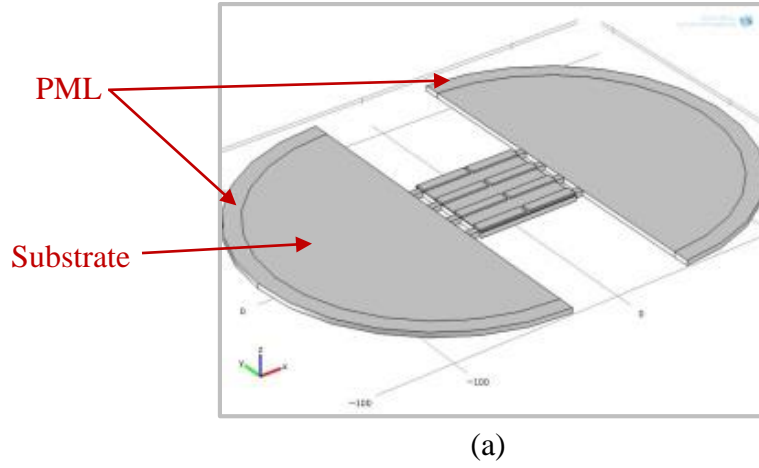


Figure 29: (a) The model build in COMOSL for a 60 $\mu\text{m}$  long 7<sup>th</sup> harmonic filter, (b) Strain field for the in-phase lateral-extensional mode. (c) Strain field for the out-of-phase lateral-extensional mode.

The frequency of the in-phase mode is approximately defined by the finger pitch which is equal to half the wavelength at resonance. The frequency separation between the two modes is set by the device geometries such as the length and the distance between the input and output electrodes. In the following, some of these parameters are evaluated using finite element analysis.

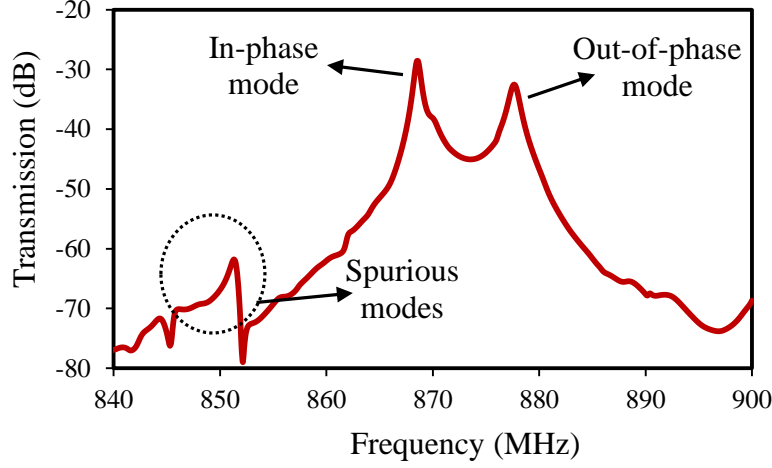


Figure 30: Simulated frequency response of a 60 $\mu\text{m}$  long 7<sup>th</sup> harmonic filter shown in Figure 29-a.

### 5.1.3. Performance optimization of monolithic TPoS filters

#### 5.1.3.1. Reducing the insertion loss

In order to reduce the insertion loss of the lateral-mode resonators, the motional impedance of the resonator has to be decreased. This can be done by increasing the actuation area on the resonator through increasing the lateral dimensions of the structure. Thus, one approach is to increase the length of the resonator. The drawback however, is the rise in the number of spurious modes. This issue can be resolved to some extent by adding support tethers to the structure [12]. Also, for longer devices, the resonance frequency decreases slightly due to the decrease in the overall stiffness associated with larger structures. It was shown in our earlier work that lower IL and higher Q values are obtained for lengths equal to odd multiples of  $\lambda/2$  and  $\lambda/4$  [65]. Another approach to increase the actuation area is to excite the higher harmonics in the resonator. In other words, increase the number of the fingers by repeating the structure along its width [33].

As mentioned earlier, there are more spurious modes associated with larger structures. In order to suppress the spurs the resonant body has to be aggressively anchored to the surrounding substrate by adding tethers [12, 15]. Multi-tethering of TPoS resonators also improves the resonator Q besides the cleaner near-resonance frequency response which is believed to be due to the refinement of energy into the desired resonance mode by bounding the structure to resonate in the target mode-shape and preventing the an-harmonic mode-coupling.

On the other hand, the tether length alters the performance of the resonator by changing the acoustic impedance seen by the wave traveling from the resonator to the substrate through the tethers. As explicitly explained in [66],  $\lambda/8$  tether length would improve the performance of high frequency resonators.

Considering that the filter structure is identical to the resonator except for the top electrode pattern, same techniques can be employed to improve the filter IL. In summary, these techniques comprise multi-tethering and increasing the actuation area by increasing the length and the mode number. The optimum design would have support length of  $(2n + 1) \lambda/8$  and a length equal to  $(2n + 1) * \lambda/2$ . Depending on the desired characteristics, there is an optimum aspect ratio for the lateral dimensions of the resonator.

#### *5.1.3.2. Increasing the bandwidth*

In order to realize a two-pole filter, the 3dB-bandwidths of the two resonance peaks should overlap (Figure 31-a). To study the effect of different design parameters on the bandwidth of the filter and compare different designs, a parameter called  $\Delta f_{3dB}$  is defined as demonstrated in Figure

31-b. This definition is only for the sake of comparison between the different designs where the 3dB-bandwidths of the two resonance peaks do not overlap and it does not have a practical use.

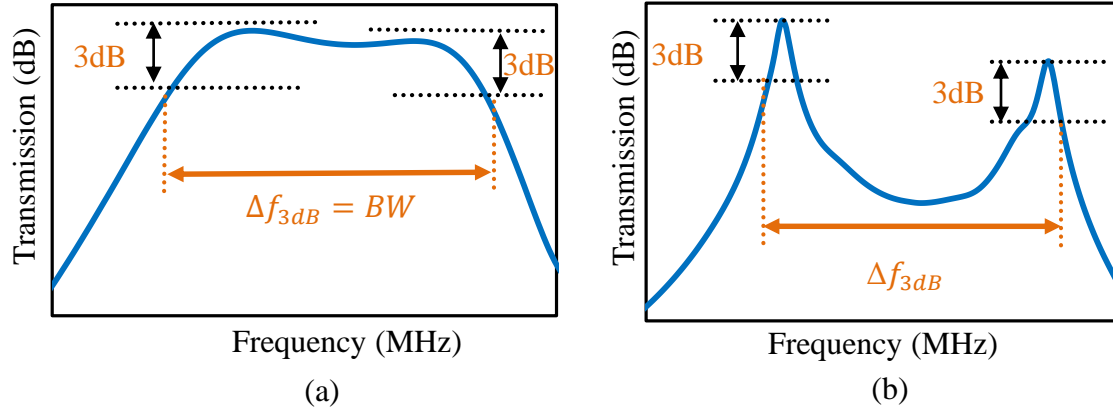


Figure 31: (a) Typical frequency response of a two-pole filter with the 3dB-bandwidths of the two resonance peaks overlapping. (b) Definition of  $\Delta f_{3dB}$  in this work, for designs where the 3dB-bandwidths of the two resonance peaks do not overlap.

The simulated frequency responses for two 7<sup>th</sup> harmonic filters with two different lengths are plotted in Figure 32. As clear from the plots, in order to decrease the frequency separation between the two resonance modes, length of the filter should be increased.

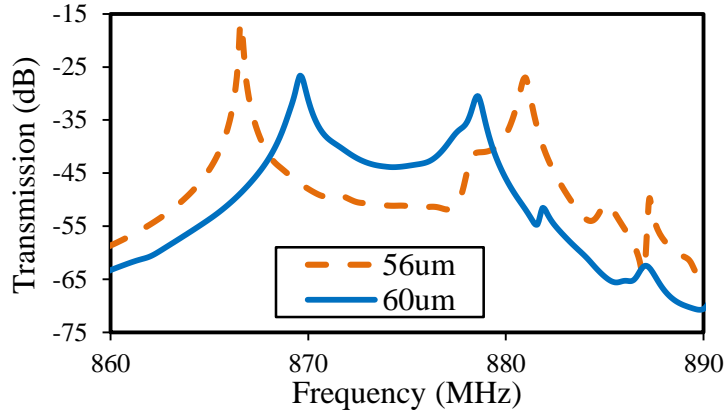


Figure 32: Simulated frequency responses for 56 $\mu\text{m}$  and 60 $\mu\text{m}$  long 7<sup>th</sup> harmonic TPoS filters demonstrating the effect of increasing device length on the frequency separation between the two resonance modes.

The input/output electrode separation was varied from 2 $\mu\text{m}$  to 8 $\mu\text{m}$  for the 60 $\mu\text{m}$  long 7<sup>th</sup> harmonic filter and the frequency responses were simulated (Figure 33). In general, the frequency separation reduces as the distance between the input and output electrodes increases due to the weaker coupling between the two modes. However, the length of the electrodes thus, the actuation area decreases as the electrode separation is increased resulting in an inefficient excitation of the modes and hence larger IL and more spurious modes [65].

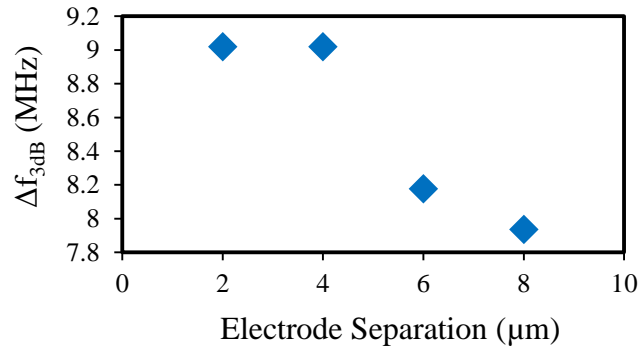


Figure 33: Dependency of the frequency separation between the two resonance modes on the input/output electrode separation for a 7<sup>th</sup> harmonic monolithic filter.

#### 5.1.4. Measurement results

FEM simulations assist us in determining how different design parameters affect the filter performance. In order to achieve very low insertion loss values, the device size has to be increased either by increasing the length or designing higher order devices. For such larger devices, it is not possible to simulate the frequency response in a reasonable time. To evaluate the guidelines and also minimize the IL and increase the filter bandwidth, several filters have been designed and fabricated with various lengths, electrode separation, and mode number in addition to different tether configurations. The filters presented in the following are fabricated on UNCD substrates. To better characterize the designs, devices are measured from all of the dies on one of the UNCD wafers with the highest Young's modulus. Also, to compare the three UNCD substrates the filter design with the lowest IL is measured on all the three wafers.

The measurements in this section were performed using an Agilent E8358A PNA Network Analyzer and a pair of GSG probes while terminated with the internal  $50\Omega$  impedance of the network analyzer. Prior to measurements, short-open-load-thru (SOLT) calibration was carried out on a reference substrate. The measurements are performed at atmospheric pressure and ambient temperature, except for the measurement of the TCF which was performed in a vacuum probe station, again with  $50\Omega$  terminations.

All the filters of this work are designed based on the multi-tethering concept which has been shown to improve the performance of the TPoS resonators such as quality factor, IL, and power handling while suppressing multiple spurious modes some of which are very close to the target mode. In order to improve the out-of-band rejection, the parasitic capacitances were reduced by removing the bottom metal layer underneath the contact pads before the deposition of AlN/Mo

stack as explained in section 4.3.

First parameter that is studied here is the length of the filter. 33<sup>rd</sup> harmonic monolithic filters with 15 pairs of tether were designed and fabricated with their length varying from 133 $\mu\text{m}$  to 234 $\mu\text{m}$ . The frequency responses of typical designs are plotted in Figure 34 and the filter parameters are summarized in Table 4 for comparison. For the 133.2 $\mu\text{m}$  design, the mode separation is such that the coupling between the two modes is not strong enough and the second resonance peak is hardly distinguishable. For devices longer than 133.2 $\mu\text{m}$ , the two peaks get closer as the length is increased such that for 212.4 $\mu\text{m}$  and 234 $\mu\text{m}$  long designs the  $\Delta f_{3dB}$  is equal to the BW of the filter. The first set of analytical data presented in Figure 35 demonstrate the effect of increasing the length on the bandwidth and insertion loss of the filters measured on the fabricated wafer with  $E$  of 933GPa. Note that the data for the 133.2 $\mu\text{m}$  designs is excluded from these plots due to the very weak coupling of the two resonance modes. As expected, the IL reduces on average as the length of the device is increased, and so does the  $\Delta f_{3dB}$ .

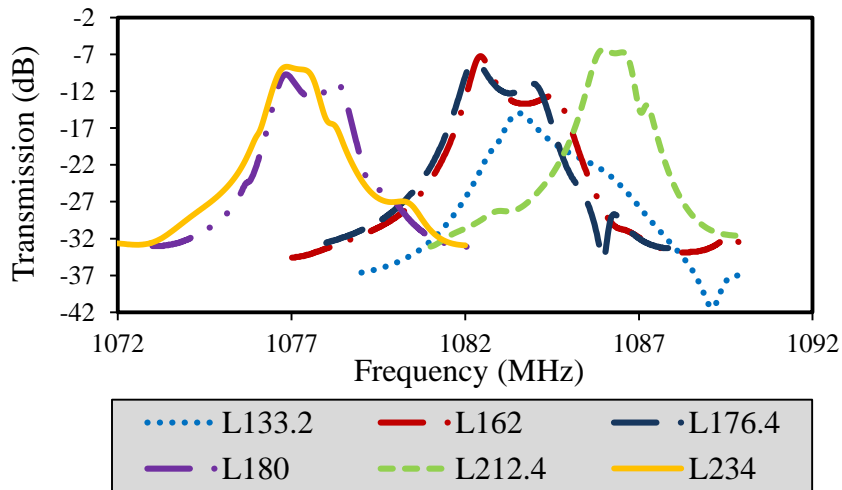


Figure 34: Effect of increasing the device length. Frequency responses are for the multi-tethered 33<sup>rd</sup> harmonic monolithic filters with different length.

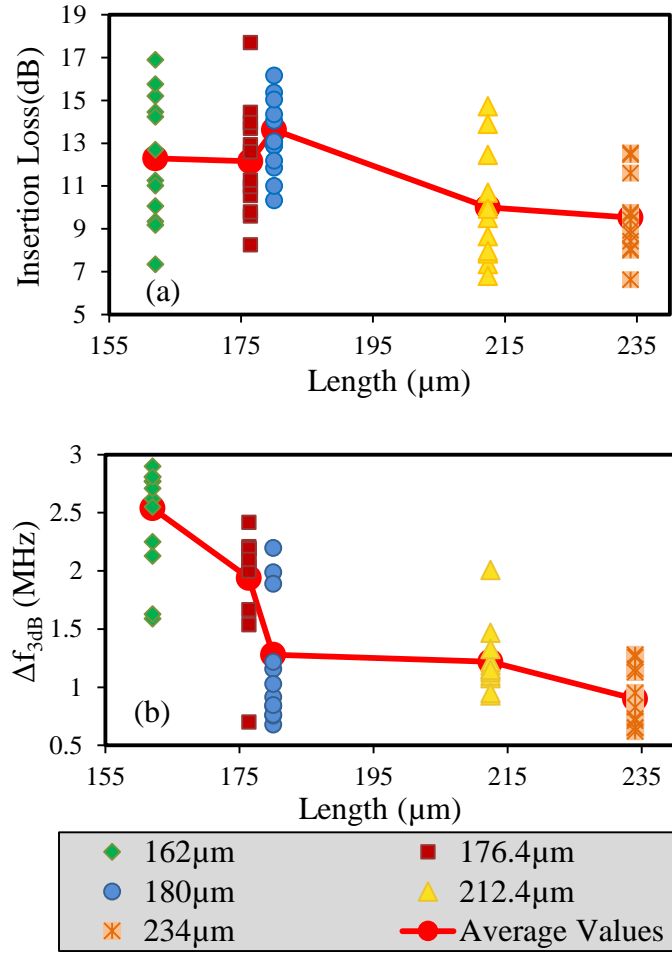


Figure 35: Measured results from 33<sup>rd</sup> harmonic filters with different lengths from all the 12 dies on the fabricated wafer with Young's modulus of 933GPa showing how the insertion loss (a) and the bandwidth (b) reducing on average as the length is increased.

Table 4: The insertion loss and bandwidth of typical 33<sup>rd</sup> harmonic monolithic filters with different lengths.

Length (μm)	133.2	162	176.4	180	212.4	234
IL (dB)	15.2	7.3	8.2	10.3	6.8	8.9
$\Delta f_{3dB}$ (MHz)	3	2.77	2.42	2.05	1.16	1.26



The second parameter that was experimentally studied was the distance between the input and output electrodes, which is referred to as the electrode separation. The  $234\mu\text{m}$  long  $33^{\text{rd}}$  harmonic filter was designed with four different electrode separations. The corresponding frequency responses for typical designs are plotted in Figure 36. From the simulation results of Figure 33, it was observed that increasing the electrode separation would push the two peaks further from each other. This trend holds true for electrode separations smaller than one wavelength ( $=14.4\mu\text{m}$ ) as displayed by the measured statistical data in Figure 37-a. For these three designs, the IL is almost constant on average. The larger BW for  $14.4\mu\text{m}$  separation between the input/output electrodes is achieved at the expense of larger insertion loss ( $\sim 2\text{dB}$  larger) which is due to the weaker excitation of the resonance modes caused by smaller electrode area (Figure 37-b). Thus, in order to increase the bandwidth of the filter while maintaining the lowest insertion loss possible, it is best to reduce the electrode separation between the input and output electrodes as much as the fabrication technology allows.

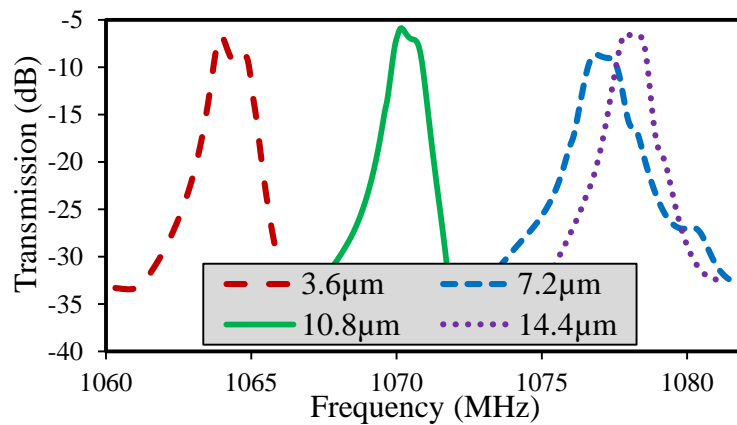


Figure 36: Frequency responses are for a typical  $234\mu\text{m}$   $33^{\text{rd}}$  harmonic filters with different electrode separations between the input and output electrodes.

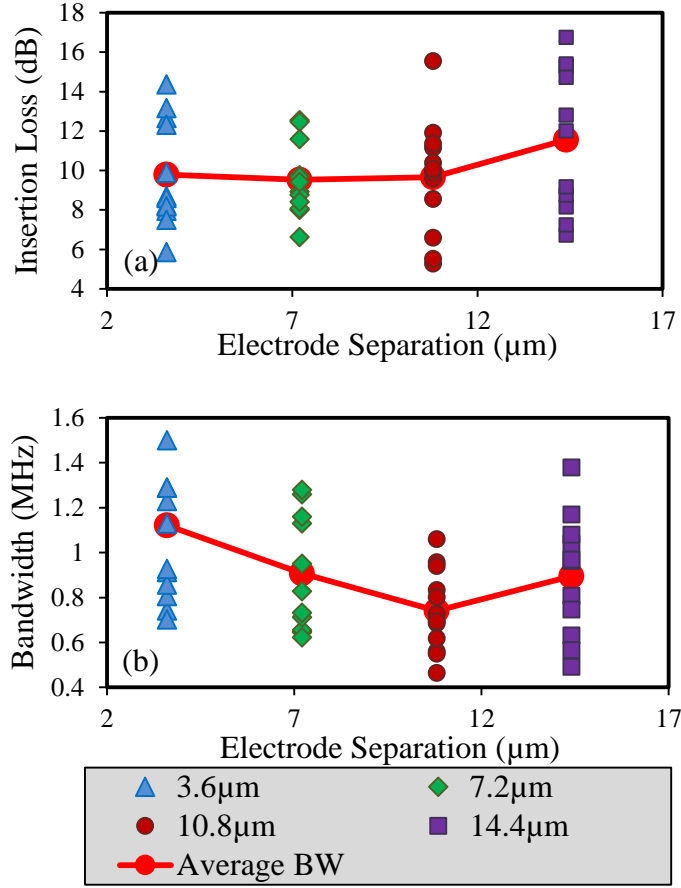


Figure 37: Results from 234  $\mu\text{m}$  long, 33<sup>rd</sup> harmonic filters with different separations between the input and output electrodes measured from all the 12 dies on the fabricated wafer with  $E$  of 933 GPa showing how the insertion loss (a) and bandwidth (b) are affected.

As shown in [65], increasing mode number generally improves the IL of the TPoS resonator. Hence, monolithic filters were designed in four different harmonic orders while keeping the aspect ratio of the device almost constant. Typical frequency responses of such designs are plotted in Figure 38. For the 21<sup>st</sup> order filter, the frequency separation between the two modes is large and thus, the coupling between them is very weak. As the order of the filter is increased, the two resonance modes get closer to form a two-pole filter but the drawback is the decrease in the filter out-of-band rejection which is due to the increase in the parasitic capacitance between the input

and output ports. These devices were measured all over one of the UNCD substrates with  $E$  of 933GPs (Figure 39). The insertion loss does not change considerably on average for the higher order harmonics. However, the frequency separation between the two resonance peaks decreases.

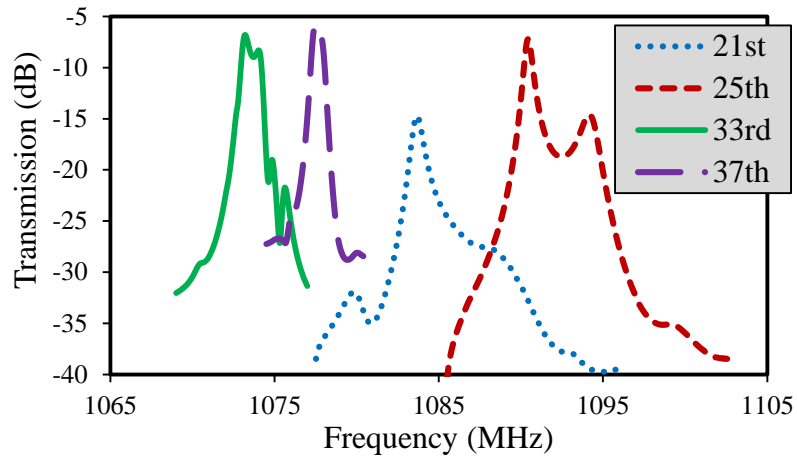


Figure 38: Frequency responses for monolithic filters with different order harmonics and approximately same aspect ratios.

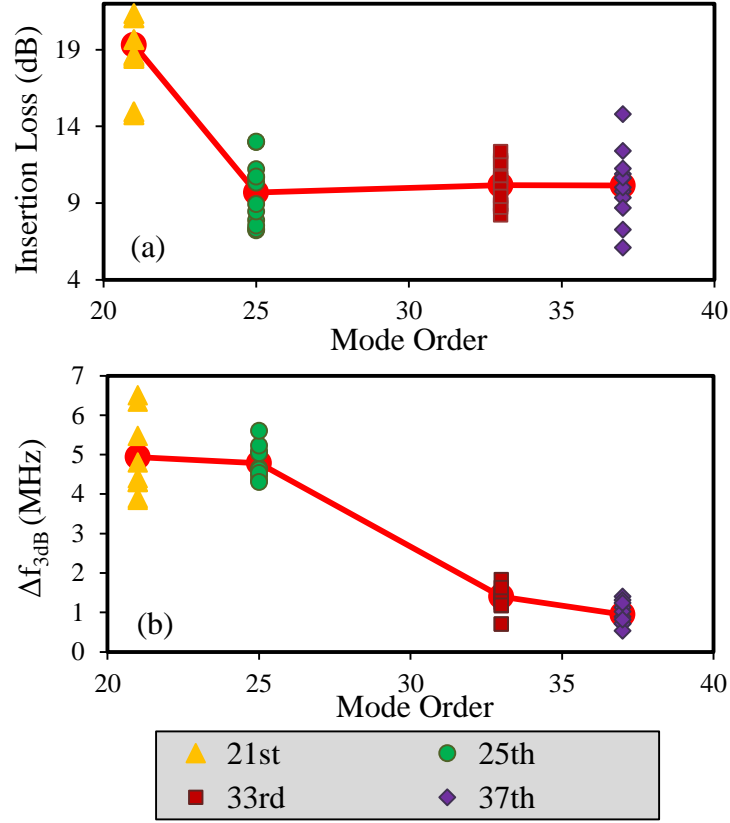


Figure 39: Effect of order of the harmonic on the filter performance. Insertion loss (a) and bandwidth (b) data collected from all the devices measured on the UNCD wafer with Young's modulus of 933GPa.

In addition, 212.4 $\mu$ m long 25<sup>th</sup> harmonic filters were fabricated with different support configurations. Besides the designs with tethers along the width, devices were designed having an additional pair of tethers in the middle of the length at the nodal line of the out-of-phase mode (Figure 27-b). Also, tethers were added at the two ends of the length to minimize the out-of-plane displacement at the edges. The statistical results are compiled in Figure 40. Adding a pair of tethers in the middle of the length deteriorates the IL. On the other hand, larger bandwidths were achieved for both designs with the additional tethers at the two ends of the length while the IL did not change noticeably.

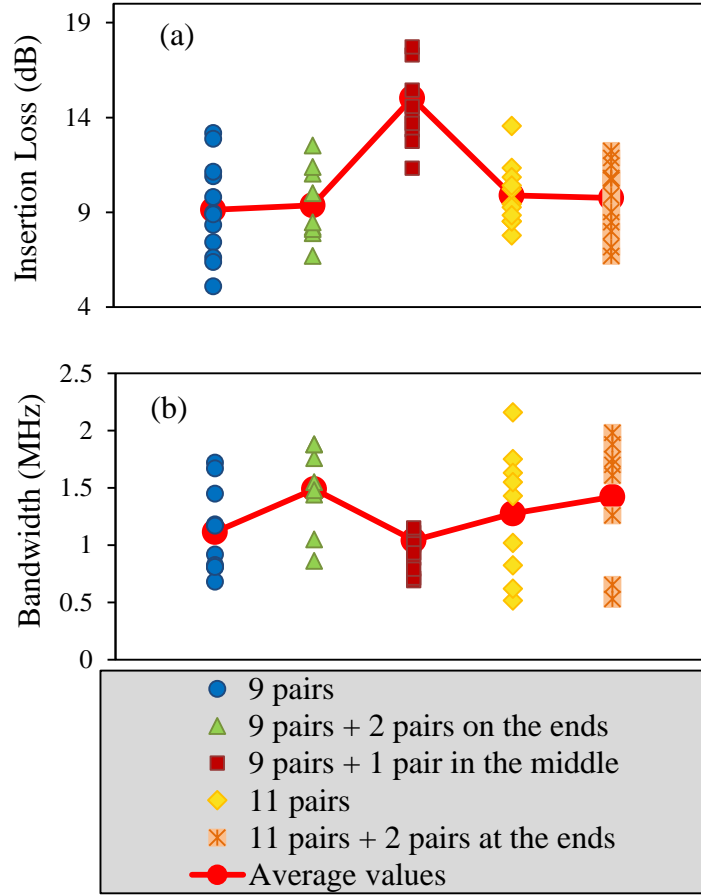


Figure 40: Effect of different support configurations on insertion loss (a) and bandwidth (b) of a 212.4 $\mu\text{m}$  long 25<sup>th</sup> harmonic filter.

#### 5.1.5. Best monolithic filter designs

Among the various designs, a 37<sup>th</sup> harmonic filter rigidly supported with 19 pairs of tethers along the width and an additional pair on the length has the lowest insertion loss reported to date for lateral-extensional filters with 50 $\Omega$  terminations. Direct termination with 50 $\Omega$  impedance eliminates the need for on-chip impedance matching networks. The SEM of the device is shown in Figure 41 and frequency responses are plotted in Figure 42 for the aforementioned device fabricated on the three UNCD substrates.

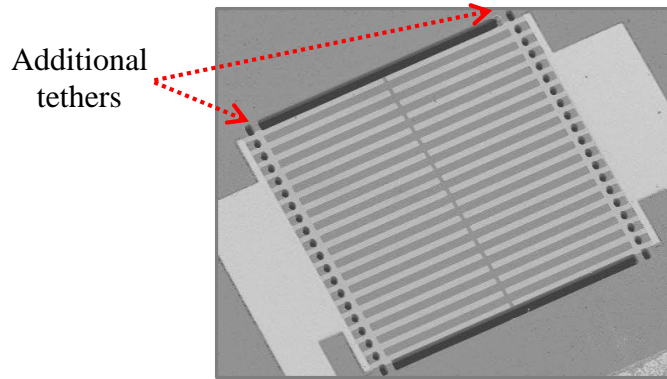


Figure 41: The SEM of a 37<sup>th</sup> harmonic monolithic filter with 19 pairs of tethers along the width and two additional pairs at the two ends of the length.

The filter on the substrate with  $E$  of 650GPa exhibits a record low insertion loss of 3.7dB at ~900MHz and has 0.09% fractional bandwidth (~800 kHz) with a 20dB-shape factor of 2.5 and out-of-band rejection of 34dB while maintaining a very small footprint (~266 $\mu$ m x266 $\mu$ m). This filter was modeled by the 4<sup>th</sup>-order system shown in Figure 43 using Multisim. In this equivalent circuit, the motional resistance of each of the comprising LC tanks is as small as 8 $\Omega$ .

The wide-span transmission plot for this low-loss filter is shown in Figure 44 for a typical device on 650GPa UNCD substrate. This multi-tethered filter has no spurious mode in a large vicinity of the passband, and only a few strong spurs from 300KHz to 2GHz (at 356MHz) which is another superior property of the multi-tethering approach.

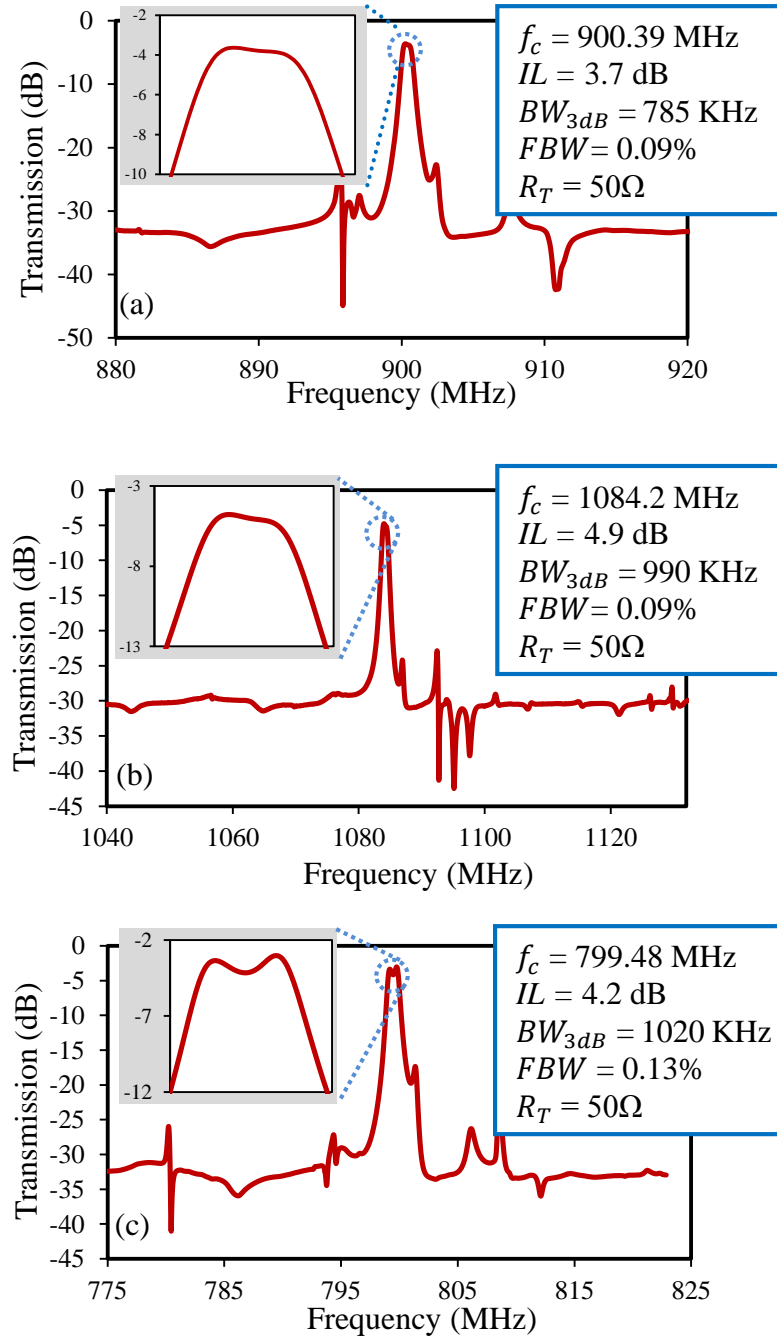


Figure 42: Frequency responses of the 37<sup>th</sup> harmonic filters with the lowest insertion loss on the three diamond wafers with Young's modulus of (a) 650GPa, (b) 933GPa, and (c) 491GPa.

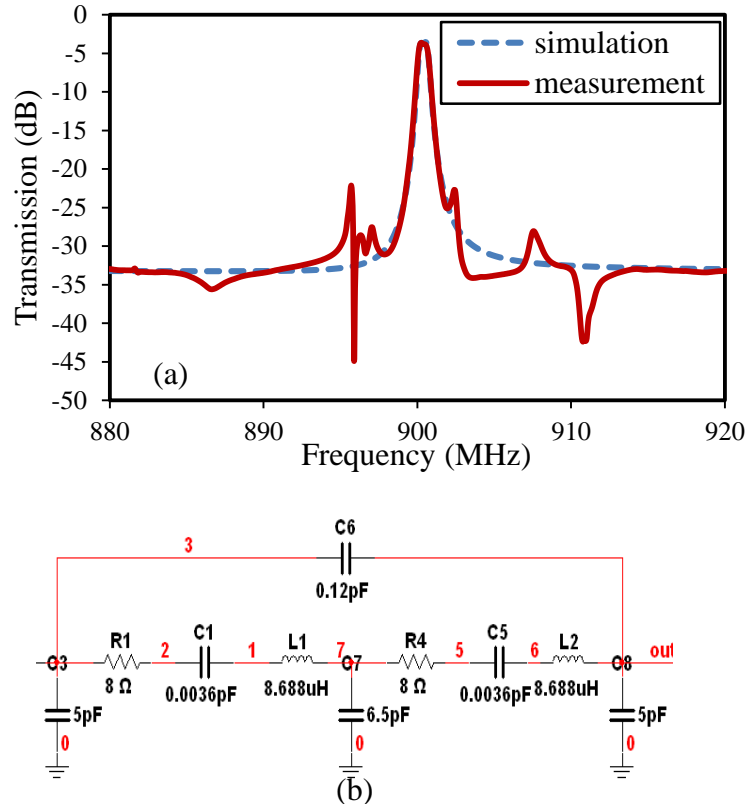


Figure 43: (a) The measured and simulated frequency responses of the 37<sup>th</sup> harmonic TPoD monolithic filter and (b) the equivalent electrical circuit model of the filter.

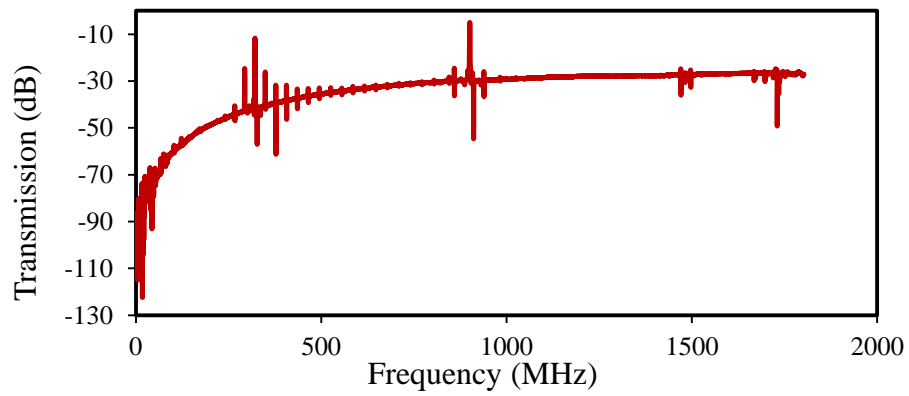


Figure 44: Wide-span frequency response of the multi-tethered 37<sup>th</sup> harmonic filter on 933GPa UNCD substrate showing very few spurious modes in the entire frequency range.



The largest bandwidth for the monolithic TPoD filters was measured for a 212.4 $\mu\text{m}$  long 25<sup>th</sup> harmonic design with 11 pairs of tethers. This filter exhibits a fractional bandwidth of 0.2% which is equivalent to 2.2MHz at 1.08GHz (Figure 45).

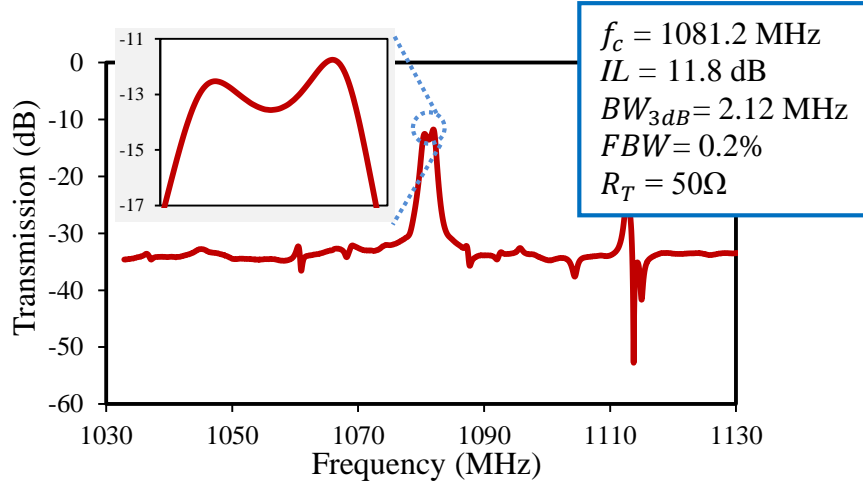


Figure 45: Frequency response of a 25<sup>th</sup> harmonic design with the largest bandwidth (0.2%) among all the designs of this work.

#### 5.1.6. TCF and Power Handling

The TCF was measured for the low-loss filter on 933GPa UNCD substrate of Figure 42(b) for temperatures ranging from -20°C to 80°C to be linear and equal to -11 ppm/°C (Figure 46), which is reasonably smaller than the values reported previously for lateral-mode filters based on AlN [40, 44]. TPoS devices fabricated on silicon exhibit a TCF is in the range of -20 to -30 ppm/°C [15, 67].

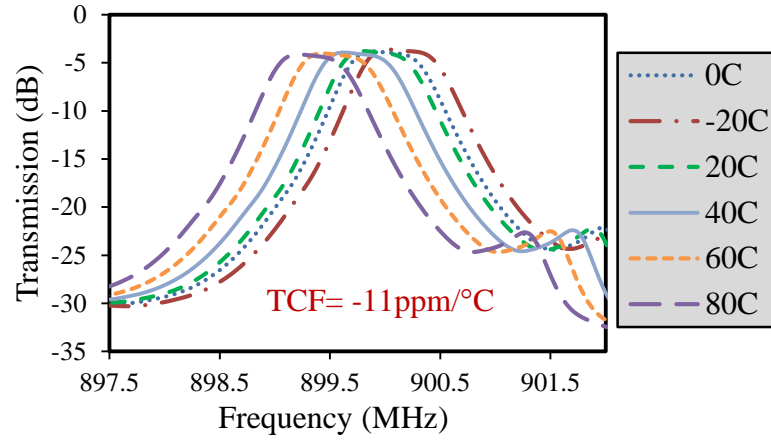


Figure 46: The overlapped frequency responses of the 37<sup>th</sup> harmonic monolithic filter at different temperatures.

To evaluate the power handling of the low-loss monolithic filter, an RF amplifier was used to enable reaching input powers above the limit achievable by the network analyzer (+15 dBm). So, prior to measurements another SOLT calibration was carried out in order to calibrate the measurement setup including the RF amplifier. The frequency response at different power levels is plotted for the filter on 933GPa UNCD substrate in Figure 47. No considerable change is observed in the frequency response of the filter and it shows a very good linearity for input powers up to +20dBm.

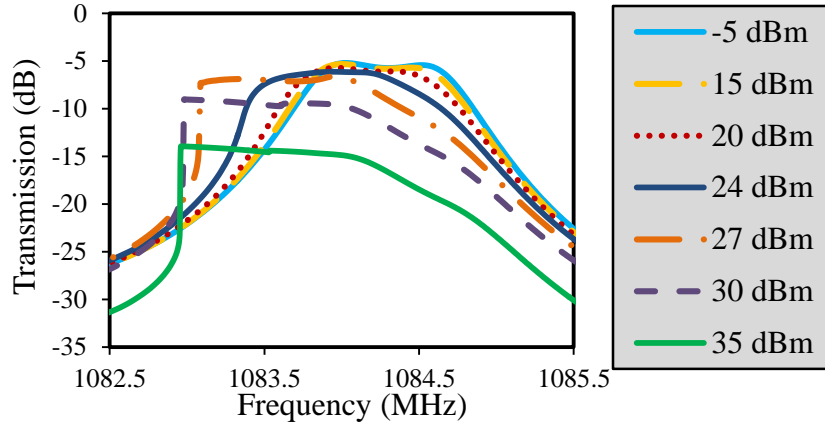


Figure 47. The overlapped frequency responses of the filter at different applied power levels.

## 5.2. Novel designs with increased bandwidth

As explained in section 5.1.3, the longer the length of the resonant device, the lower the center frequency due to reduced overall stiffness of the structure. This concept was exploited to increase the bandwidth of the filters. Hence, filters were designed with the length increasing gradually from one end to the other creating a xylophone-like structure. This results in the dispersion of the acoustic velocity over different regions of the resonator causing the bandwidth to widen. A 7<sup>th</sup> order monolithic filter was built in COMSOL<sup>®</sup> once with a fixed length (inset of Figure 48-a) and then with the length varying linearly from 52 $\mu$ m to 56 $\mu$ m (inset of Figure 48-b). The length and placement of the tethers are the same in both cases. The simulated frequency responses are plotted in Figure 48. Comparing Figure 48 (a) and (b), there are three resonance modes that are coupled together to form a third order filter response around the frequency of interest for the xylophone filter. It has to be noted that due to the computation limits, only small structures could be simulated to prove the concept of the idea. However, as thoroughly discussed in section 5.3.1, in order to achieve low insertion loss values the size of the resonant structure has to be considerably larger

than the simulated structure. Figure 49 shows a SEM of such 35<sup>th</sup> order xylophone design with 18 electrode pairs. The length starts from  $243\mu m$  which is  $27x\frac{\lambda}{2}$  and increases linearly to  $35x\frac{\lambda}{2} = 315\mu m$ . The measured frequency response is plotted in Figure 50. This device was fabricated on a 6 $\mu m$  SOI substrate with a center frequency of 475MHz and exhibits a very low IL of 2dB with 50 $\Omega$  terminations. Although, the modes cannot be easily distinguished from each other since they are very close in frequency, the fractional bandwidth is 0.26% which is almost thrice the value reported previously for the low-loss second order monolithic filter of this work.

The SEM of the sinc-apodized resonator is presented in Figure 52. This design features an apodized resonator in the form of a sinc function where the length of the resonator is modulated by a sinc function along its width. The idea was adopted from the electrode apodization for SAW devices where it is used to achieve an arbitrary frequency response [68]. A spatial sinc apodization on the interdigitated electrodes of a resonator in the direction of propagation would translate into convolving its frequency response by a rect function [69]. Hence, an infinitely long sinc-shaped resonator would theoretically be an ideal filter. In practice, a sinc-shaped resonator with a finite width would have a trapezoid frequency response.

A few differently apodized resonators were designed and fabricated on the 6 $\mu m$  SOI substrate. Figure 52 shows the layout and Figure 53 shows the SEM for the two modifications of the sinc resonator. The corresponding frequency responses for all three designs are plotted in Figure 54 for comparison. The sinc resonator (shown in Figure 51) exhibits a single strong resonance at 477MHz with Q of 500. The hourglass designs on the other hand are two half-sinc resonators connected at one end. As evident

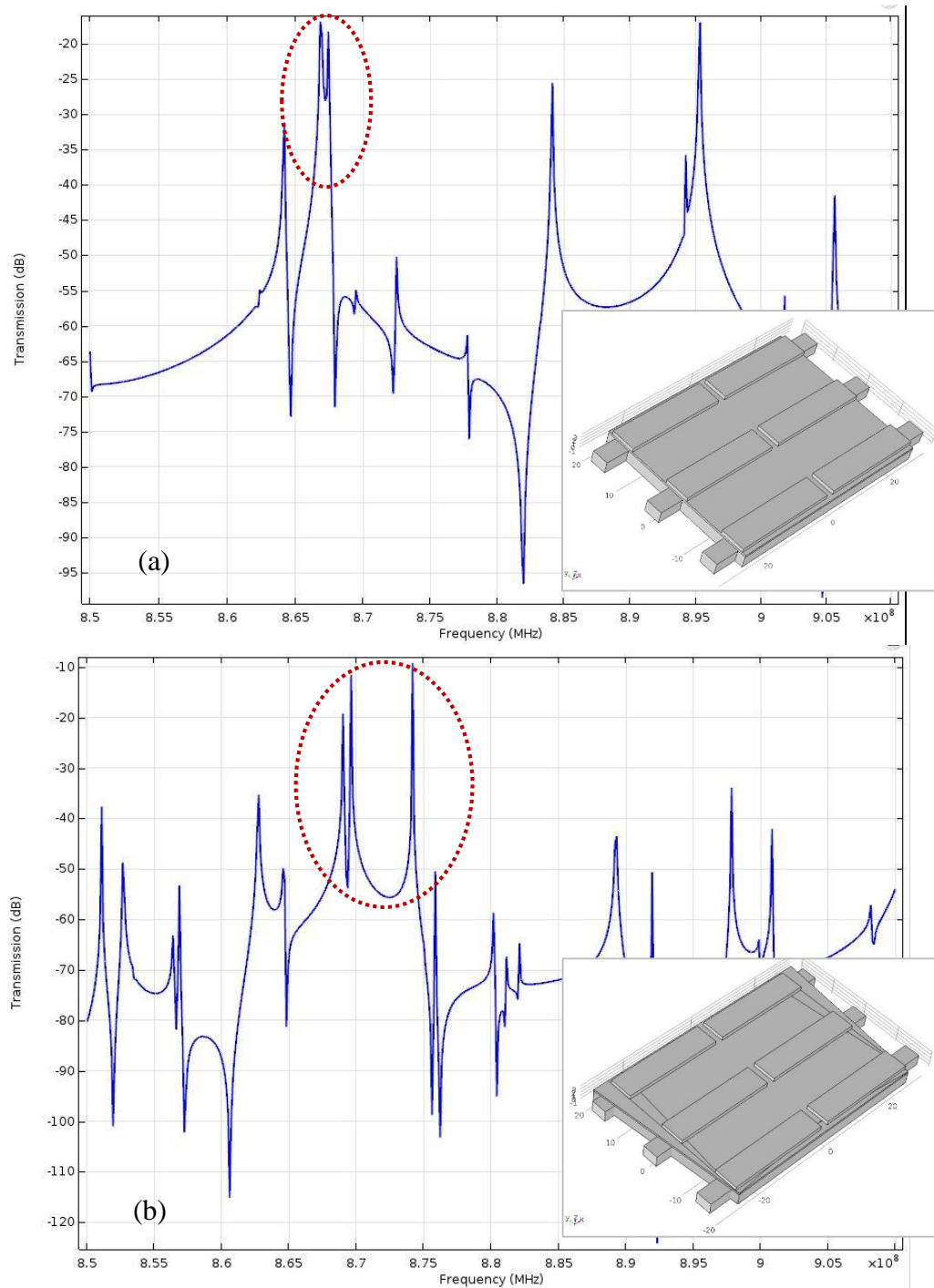


Figure 48: Simulated frequency response of a 7<sup>th</sup> order (a) rectangular and (b) xylophone monolithic filter. The rectangular monolithic filter is a second order filter with two resonance peaks coupled together. There are at least peaks coupled together for the xylophone design resulting in a larger bandwidth.

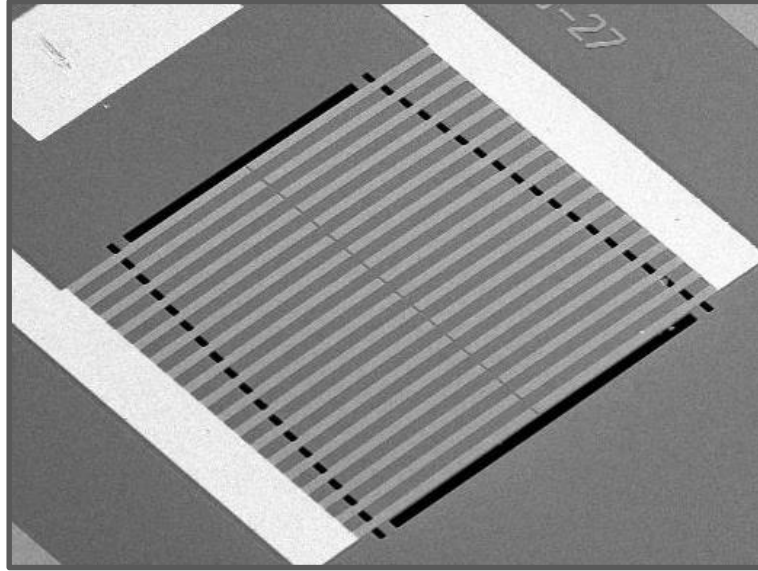


Figure 49: Layout of the 35<sup>th</sup> order xylophone filter. The length of the filter is decreased linearly from 243 $\mu\text{m}$  to 315 $\mu\text{m}$ .

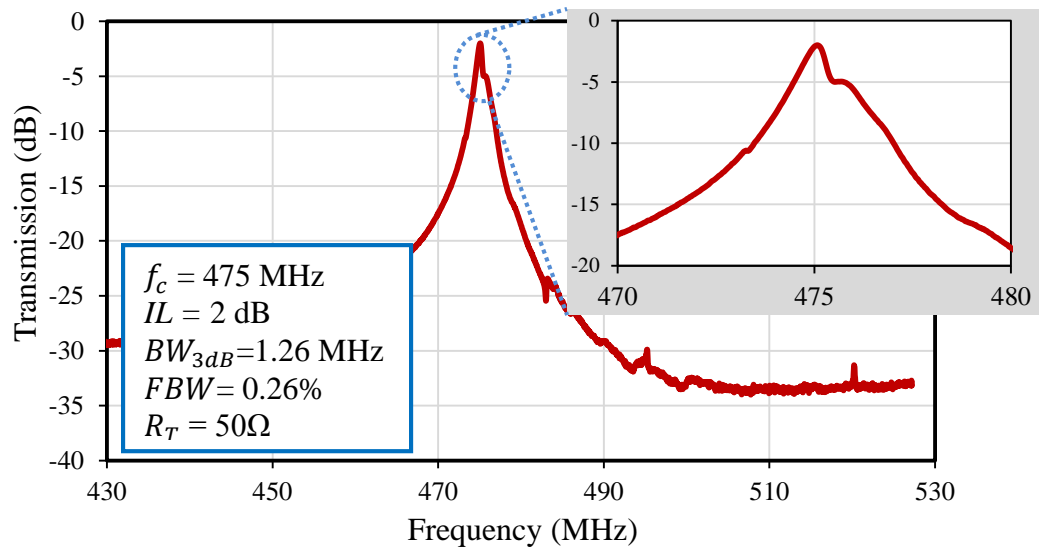


Figure 50: Frequency response of a 35<sup>th</sup> order xylophone design fabricated on SOI substrate.

in Figure 54-b, the HG1 design is a second order system with two very close peaks coupled together at the peak which is speculated to be the result of mechanical coupling of the two resonant structures. The HG1 design exhibits a low IL (4dB) and BW of 1.2MHz equivalent to  $FBW_{3dB}$  of 0.26% at 476MHz. The HG2 design is the one where the two halves of the structure are joint at two narrow areas and are mechanically coupled. The coupling of the two structures results in a higher order system, thus a larger bandwidth. This hourglass filter exhibits a relatively large fractional bandwidth of about 1% (Figure 55). However, the IL of the hourglass design has notably increased from a few dB to more than 13dB. This is partially due to the overall smaller structure which can be compensated for by increasing both the length and the number of fingers of the device as explained in section 5.1.3. On the other hand, a notable amount of the acoustic energy escapes the resonant structure, through the paths marked in Figure 52(c), as the wave travels along the width resulting in more loss. This can be mitigated by placing acoustic reflectors around the device [66].

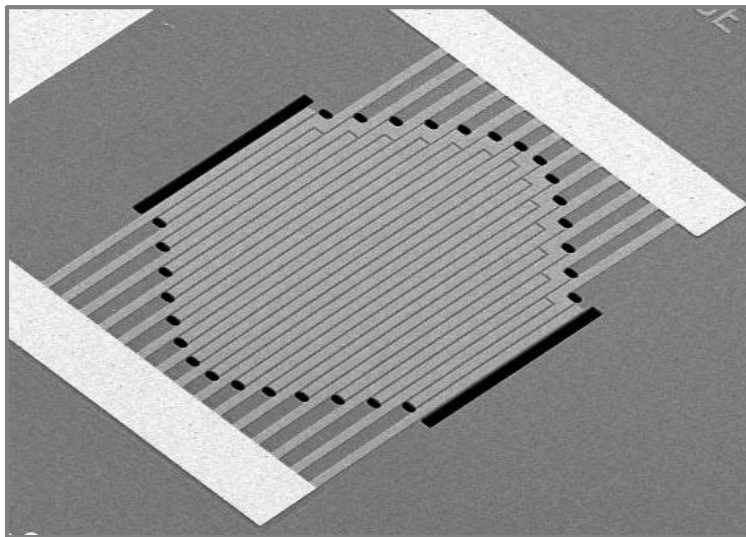


Figure 51: Layout of a sinc-shaped apodized resonator.



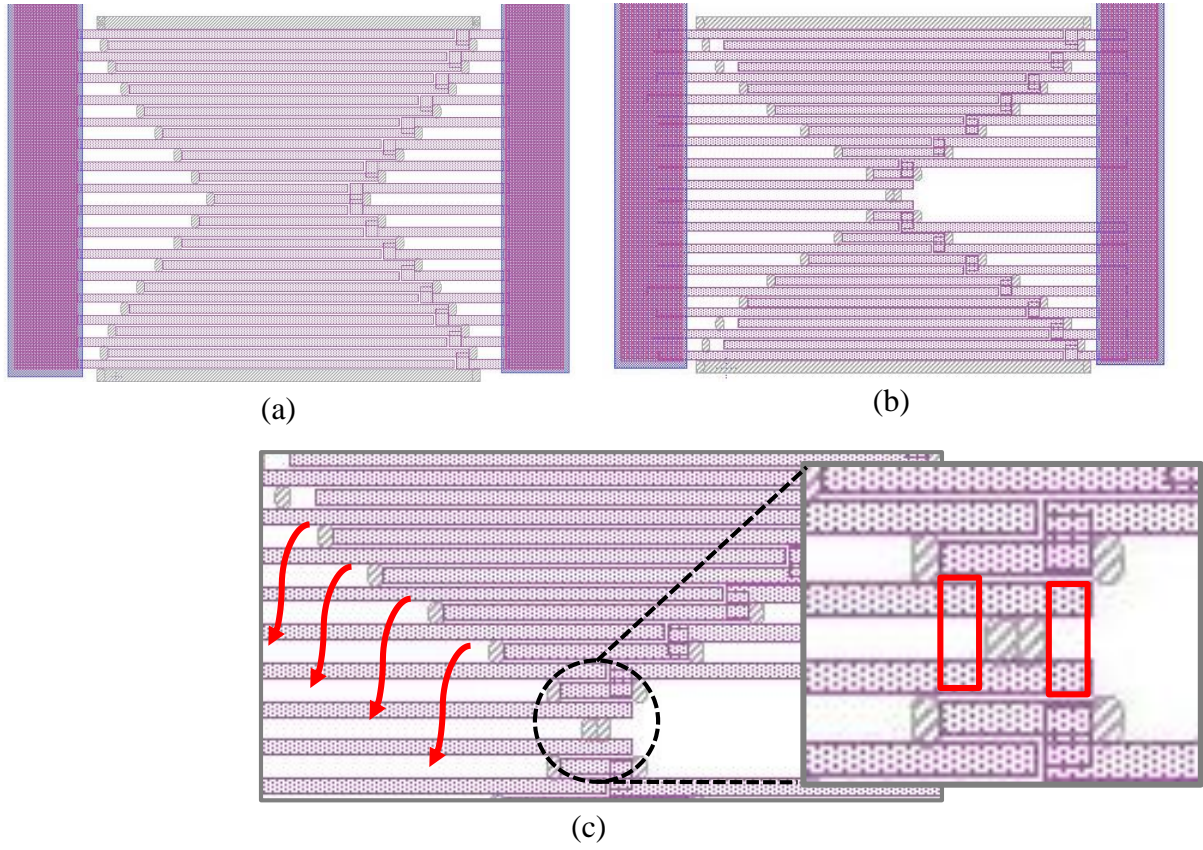


Figure 52: Layout of hourglass filters. (a)HG1, (b) HG2. (c) Close-up of the HG2 design showing the routes through which the acoustic energy escapes the resonant structure leading to a higher loss. The inset is the area where the two half of the structure connect resulting in their mechanical coupling and realization of a fourth order system.

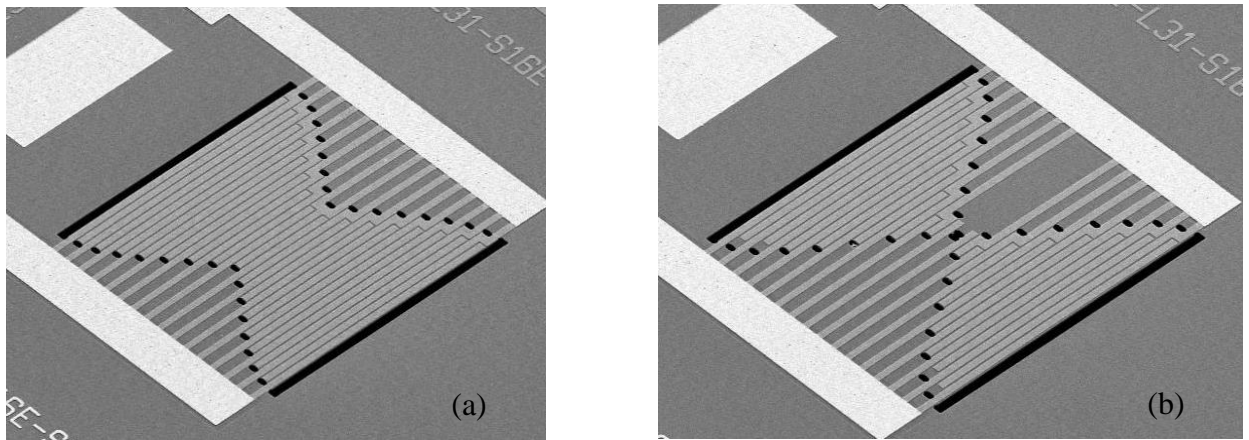


Figure 53: SEM of the fabricated (a) HG1 and (b) HG2 designs.



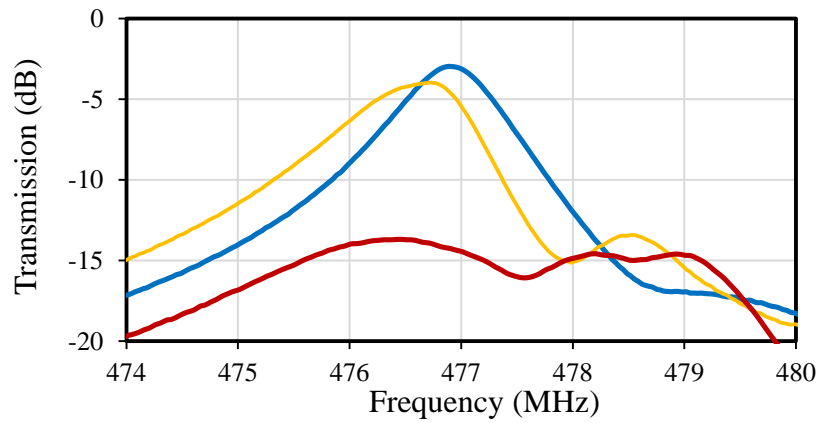
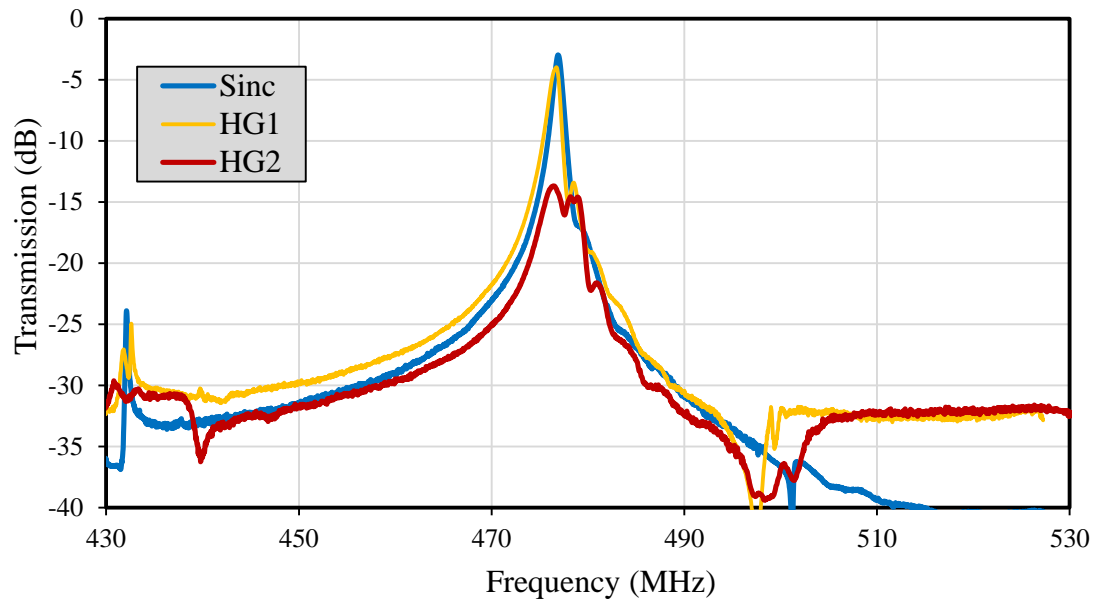


Figure 54: Frequency responses of the sinc-shaped resonator and the two hour glass designs, HG1 and HG2.

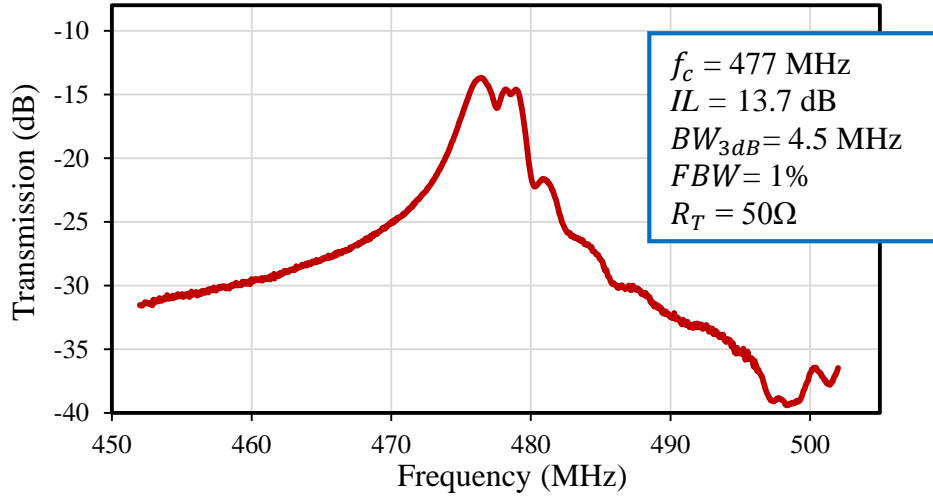


Figure 55: Frequency response of the HG2 design with 31 electrode fingers fabricated on SOI substrate.

The filter response can be improved in terms of rejection, IL, and bandwidth if it is terminated with the right impedance which almost always has a complex value. In order to change the terminations of the filter, the measured S-parameters were imported in ADS software using a two-port data element which was then terminated with an inductor and a resistor in parallel (Figure 56). The values of both the inductor and the resistor were then tuned to improve the IL and increase the bandwidth. As can be seen in Figure 57, increasing the termination resistance to  $70\Omega$  levels out the peaks in the passband. The 3dB bandwidth was increased by 7% after adding 60nH inductors. Further increasing the termination resistance to  $100\Omega$  reduces the IL to 10.8dB.

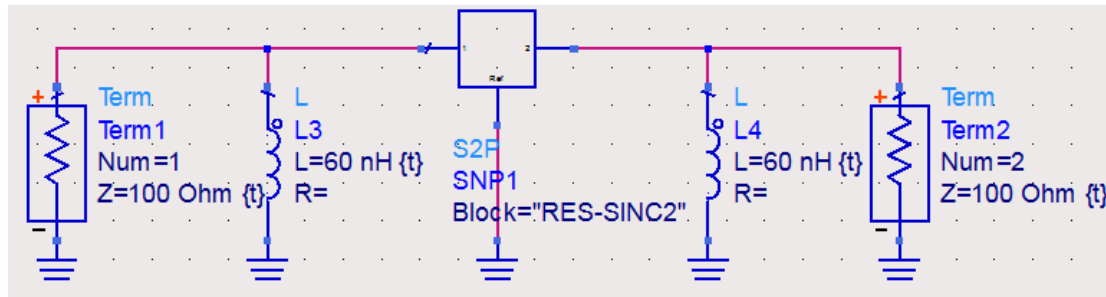


Figure 56: Model built in ADS to simulate the filter design with different terminations.

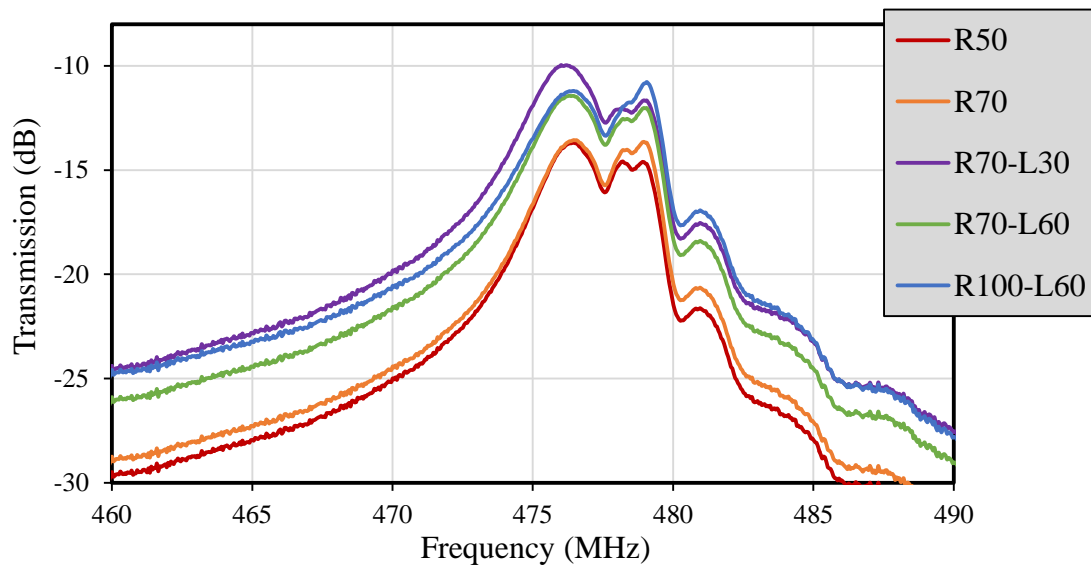


Figure 57: Frequency response of the hourglass filter with different terminations. The R represents the resistor and L is the inductor added in parallel to the resistive termination.

## CHAPTER SIX: TPoS IMPEDANCE TRANSFORMERS

### 6.1. Introduction

Lateral-extensional mode piezoelectric MEMS resonators have become of interest in recent years due to the advantages they offer such as low motional resistance, small size, and multi-frequency operation on a single chip. These resonators have been employed to build oscillators [61, 70] and high performance filters [11, 46]. One less-explored application for such resonators is impedance transformation that could be used in a transceiver architecture where impedance matching between high frequency components such as the front-end filter and the low-noise amplifier (LNA) is of interest. Impedance transformers in RF applications are commonly realized by using inductive coils, transmission lines, and lumped LC circuits. Piezoelectric transformers have some advantages over these techniques including voltage isolation, small size, better performance especially at higher frequencies, and that they do not introduce electromagnetic noise. Single ended to differential transformers have been previously realized through FBAR resonators with 4:1 impedance transformation [71]. Some work has also been done to develop lateral-extensional resonators as piezoelectric transformers [72, 73, 74].

This chapter focuses on developing lateral-mode (or contour-mode) thin-film piezoelectric resonant transformers with high impedance ratios. A 19:1 impedance transformation ratio will be demonstrated, however, the basic design method is easily extendable to enable higher ratios. The platform used to implement the primary idea is the TPoS technology discussed in previous chapters nevertheless purely piezoelectric transformers can also be designed using the same technique.

## 6.2. Design Concept

The TPoS resonator used in this work is a two-port high-order design as shown in Figure 58. The two-port TPoS resonator can be modeled by the BVD equivalent circuit shown in Figure 59 [75, 76]. In this model, the motional resistance ( $R_m$ ) captures the resonator insertion loss. The parasitic feed-through capacitances are denoted by  $C_f$ . The two shunt capacitors are the static capacitances formed at the input and output ports by the parallel plates of the top electrode fingers, the ground plate, and the piezoelectric dielectric layer in between. Thus, for a resonator with even number of interdigitated fingers, the input and output shunt capacitances would be equal. Also, the circuit would be completely symmetric if looked into from the input or output port leading to equal input and output impedances.

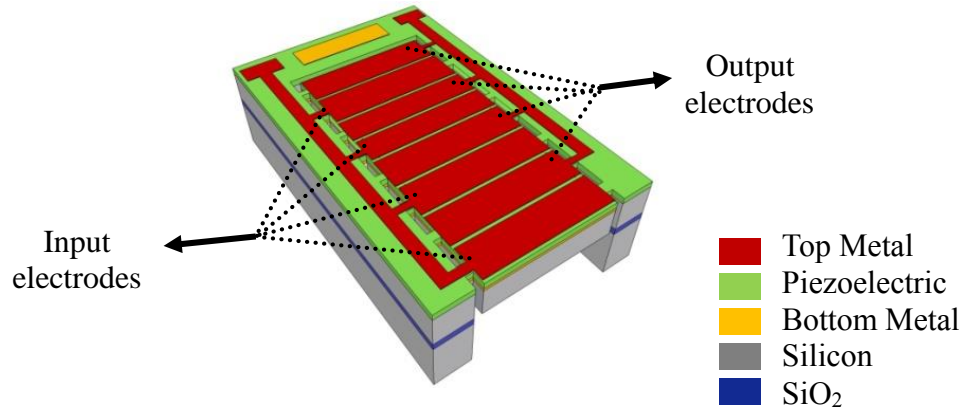


Figure 58: Illustration of a thin-film piezoelectric-on-substrate resonator with eight electrode fingers.

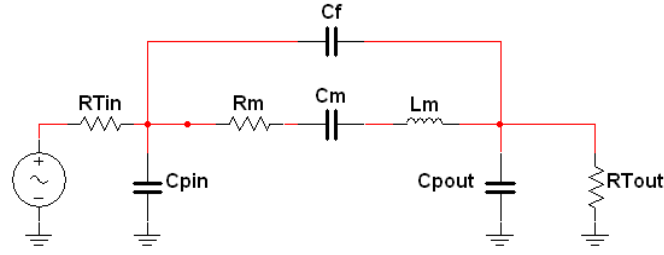


Figure 59: Butterworth Van Dyke equivalent circuit model of a two-port resonator.

According to the BVD model of the TPoS resonators, the output voltage hence, the voltage gain depends on the termination resistance. A 10<sup>th</sup> order TPoS resonator was modeled using Multisim and then the termination resistance was varied to study the effect on voltage gain. Simulation results are plotted in Figure 60. As the output termination increases from 50 $\Omega$  to 500K $\Omega$ , the voltage gain rises to almost +20dB. However, the gain is limited by the value of the shunt capacitor at the output port and it saturates for larger terminations.

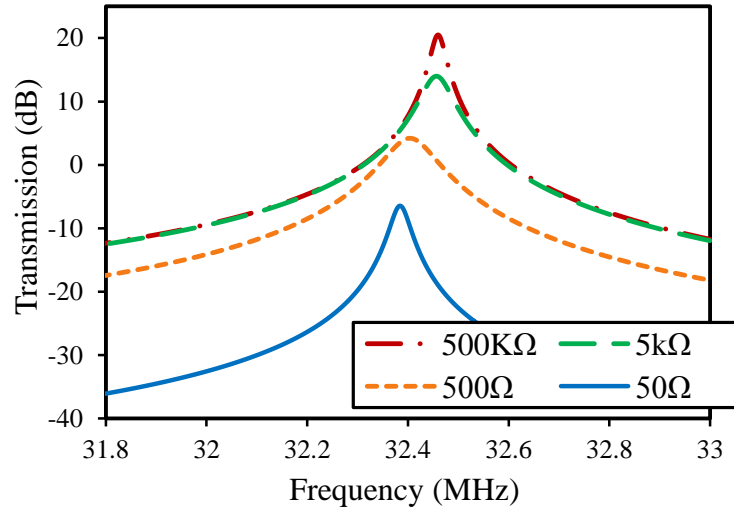


Figure 60: Simulation results showing the effect of output termination on the voltage gain for a 10<sup>th</sup> order TPoS resonator.

In order to realize the resonator as an impedance transformer, the capacitors on either port could be altered. In order to have voltage amplification, the output shunt capacitor should be reduced. As mentioned earlier, the shunt capacitors in a two-port TPoS resonator are comprised of the parallel capacitances formed under each electrode finger. In the case of Figure 58, there are four electrodes at each port covering the areas with similar strain polarity according to the mode shape shown in Figure 61-a. These four individual capacitors are connected in parallel as depicted in the cross section of Figure 61-b. To achieve the maximum attainable gain for the transformer configuration, the idea is to minimize the output shunt capacitor by connecting the four capacitors in series. Thus, the bottom metal layer is patterned to isolate the bottom electrode for each finger. Based on the induced electric field in the piezoelectric film, each bottom electrode finger has the opposite polarity of the top electrode finger covering the same stress area as depicted in Figure 61-c.

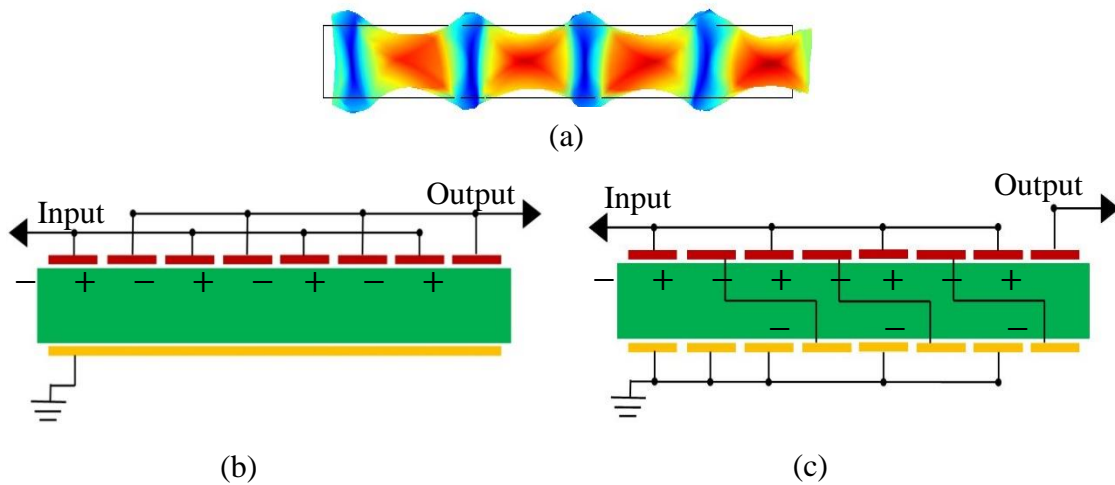


Figure 61: (a) Mode shape for an 8<sup>th</sup> order TPoS resonator. Red shows the tensile stress and blue represents compressive stress. (b) Electrode configuration for a conventional resonator. (c) Electrode configuration for an impedance transformer.

Hence, by alternately connecting the bottom electrode to the next top electrode, the series connection of the capacitors is realized at the output port while the input configuration is kept intact. As a result, the output parallel capacitor would be 16 times less than the input. In general, if the resonator is comprised of  $2 \times n$  fingers, this novel electrode configuration is expected to result in  $1:n^2$  impedance transformation ratio, and hence a voltage gain equal to  $n$ .

### **6.3. Fabrication Process**

Figure 62 illustrates the fabrication process step to form vias connecting the top electrode to the bottom electrode. For the fabrication of TPoS transformers a SOI wafer was used with a  $5\mu\text{m}$  thick device layer. The fabrication process is as described in section 3.3.1.

### **6.4. Measurement Results**

Frequency response measurements were performed using an Agilent E8358A PNA Network Analyzer and a pair of GSG probes while both ports were terminated with  $50\Omega$  resistors. Prior to measurements, a short-open-load-thru (SOLT) calibration was carried out on a reference substrate.

To examine the performance of TPoS transformers, multi-tethered  $10^{\text{th}}$  order resonator and its sister transformer were designed and fabricated. The SEMs for both designs are displayed in Figure 63. For this transformer design, all the output fingers are connected in series. The measured frequency responses with  $50\Omega$  terminations at the ports are plotted in Figure 64 and the IL and Q values are listed in Table 5.



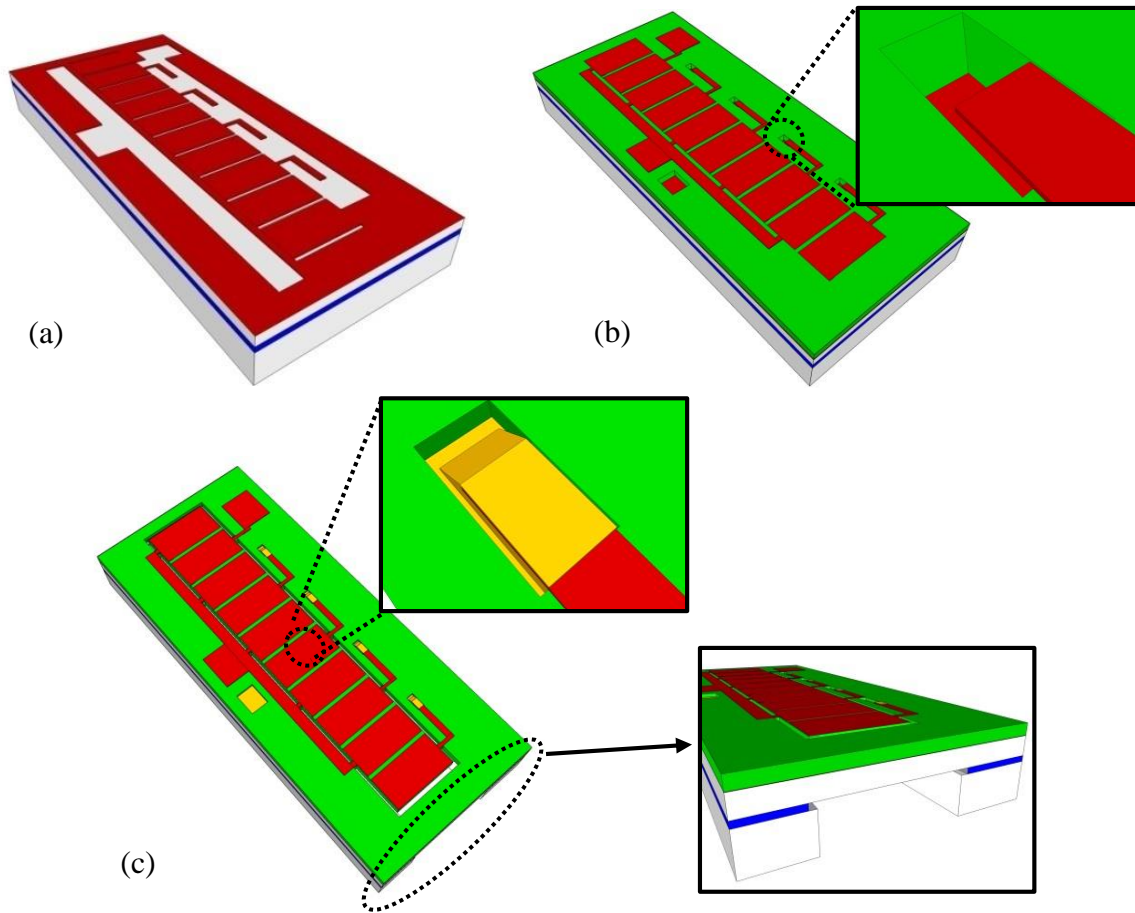


Figure 62: Fabrication process flow for the thin-film piezoelectric-on-substrate transformers. (a) patterning the bottom metal layer, (b) Etching AlN to access the bottom metal after the deposition of AlN/Mo stack and patterning the top metal, (c) Sputtering gold on the formed vias to make contact between the top and bottom metal layers, etching the device stack from the top and also the handle silicon from the backside followed by releasing the device by etching the oxide layer.

The motional resistance of the resonator is  $\sim 107\Omega$  while it is  $655\Omega$  for the transformer design. The output electromechanical coupling coefficient is the ratio of the output current to the velocity. By connecting the output finger capacitors in series, the total current pumped into the output port would be smaller resulting in a lower electromechanical coupling. The motional resistance of the lateral-extensional resonators is inversely proportional to the electromechanical coupling

coefficients and  $Q$  based on (1) where  $\eta$  is the electromechanical coupling [76], which explains the larger motional resistance for the transformer configuration.

$$R_m = \frac{n \pi A \sqrt{E \rho}}{2Q} \frac{1}{\eta_{in} \eta_{out}} \quad (33)$$

Table 5: Performance characteristics of the resonator and transformer when measured with  $50\Omega$  terminations.

Device	$f_c$ (MHz)	$IL$ (dB)	$Q_{unloaded}$
Resonator	32.38	6.3	2883
Transformer	32.38	17.6	1467

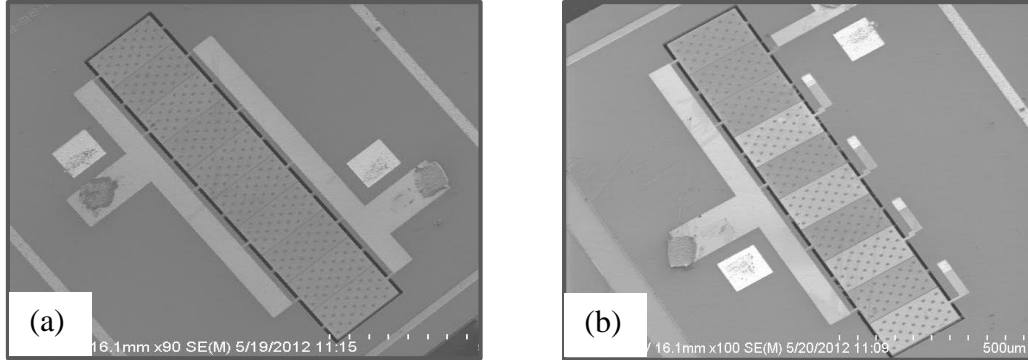


Figure 63: SEM showing 10<sup>th</sup> order TPoS (a) resonator and (b) transformer.

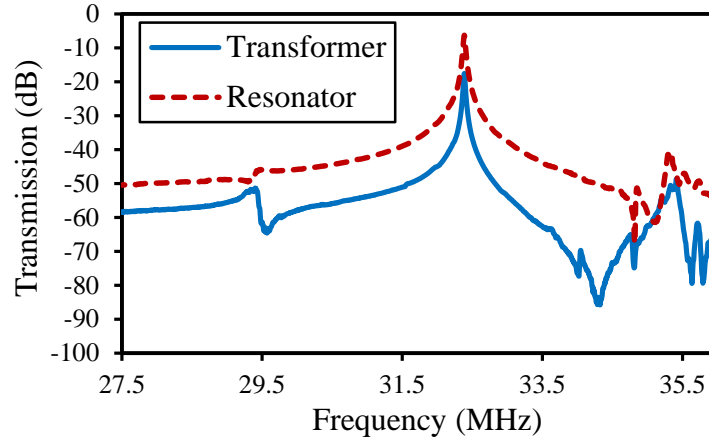


Figure 64: Transmission plots for the 10<sup>th</sup> order resonator and transformer measured with 50 $\Omega$  terminations.

The Z-parameters of both designs were extracted from the measured S-parameters, and  $Z_{11}$  and  $Z_{22}$  parameters are plotted in Figure 65:  $Z_{11}$  and  $Z_{22}$  parameters for the resonator (a) and transformer (b) designs. for comparison. As can be seen, for the resonator design the two impedances are perfectly matched whereas for the transformer design the output impedance is larger than the input in the entire frequency range, e.g. at the resonance frequency, it is  $\sim 19\times$  the impedance at the input. The 19:1 impedance transformation ratio is smaller than the expected value (25:1) which is believed to be due to the vias connecting the top metal to the bottom metal adding a considerable amount of resistance in series with the output parallel capacitance.

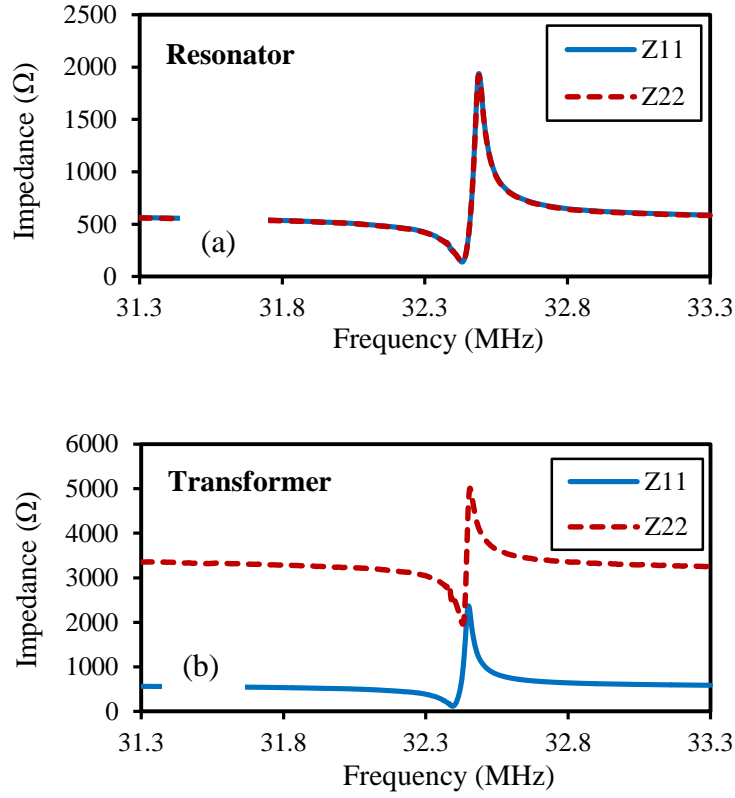


Figure 65:  $Z_{11}$  and  $Z_{22}$  parameters for the resonator (a) and transformer (b) designs.

Due to the larger impedance at the output port of the transformer, the termination load has to be increased accordingly for a fair comparison between the performance of the resonator and transformer designs. Hence, the  $50\Omega$  resistor was replaced with a  $950\Omega$  ( $19 \times 50$ ) at the output port while maintaining the  $50\Omega$  at the input and the frequency response was simulated in ADS and plotted in Figure 66. The insertion loss of the transformer with the proper terminations at the ports is 7dB which is very close to the insertion loss of the resonator with 1:1 termination resistances.

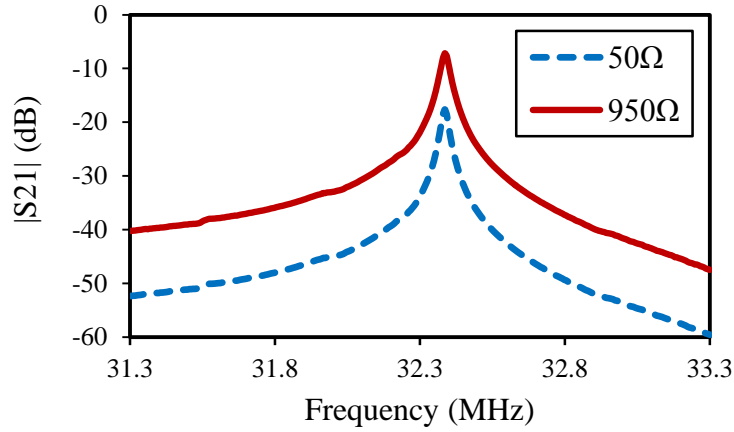


Figure 66: The transmission response of the transformer with different termination loads at the output.

In order to attain the highest voltage gain, the transformer was wire-bonded onto a PCB board and the output capacitance was canceled out by soldering a parallel inductor at the output port. A voltage gain of +10.4dB was achieved with a 2.3μH inductive load after fine tuning the inductor.

The input/output voltages were measured at the resonance frequency and the waveforms are depicted in Figure 67. The voltage step up ratio (~3x) is smaller than the expected value mainly because of the limitation imposed by the measurement system. A high frequency probe was used which has a 1pF capacitance at the oscilloscope terminal that is larger than the value of the shunt capacitor (0.23pF) at the output of the transformer reducing the output voltage.

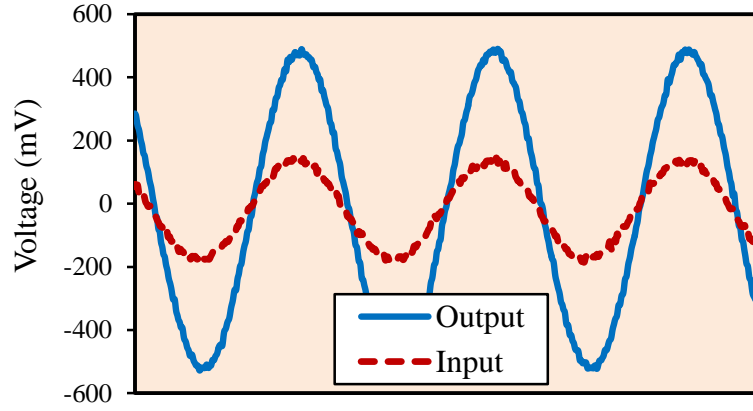


Figure 67: Input and output waveforms for the 10<sup>th</sup> order transformer at the resonance frequency with 2.3 $\mu$ H inductive termination at the output port.

## 6.5. Conclusion

For the first time, piezoelectric impedance transformers were demonstrated based on thin-film piezoelectric-on-substrate resonators in a small footprint of 0.294mm<sup>2</sup>. The proposed technique is to alter the input/output parallel capacitances to realize unequal impedances at the two ports in such resonators.

A 19:1 impedance transformation ratio was achieved for a 10<sup>th</sup> order resonator. A voltage step up ratio of at least 3 was also reported. The performance of the transformer is similar to that of the resonator if terminated with the proper load impedance. Also, a maximum voltage gain of +10.4dB is attained with an inductive termination.

## **CHAPTER SEVEN: LOW-NOISE OSCILLATOR USING A TPoS RESONATOR**

### **7.1. Introduction**

Reference oscillators are demanded in almost every electronic system for various applications. Some of these applications such as high speed data communication have very tight phase noise (PN) requirements which cannot be achieved using passive electrical components due to the low Q of the on-chip inductors [77]. Contrarily, quartz crystal resonators exhibit very high Q and have been utilized in oscillators with very low PN values and excellent temperature stability for high performance applications [1, and for a brief history refer to 78]. The drawback however is their relatively large size and the fact that their fabrication process is incompatible with the mature silicon micro-fabrication technology. MEMS resonators, on the other hand can potentially be integrated with CMOS and offer a competing alternative for the bulky quartz resonators in a wide variety of consumer electronics where size and cost are critical factors. In recent years, both piezoelectric and capacitive MEMS oscillators have been reported with excellent PN performance [79, 80].

The far-from-carrier phase noise in an oscillator is inversely proportional to the carrier power [81]. Thus, in applications with stringent requirement on stability, it is desired to operate the oscillator at high power levels or in other words, at large ac voltage amplitudes. However, the nonlinear terms in the resonator's equation of motion gradually become dominant and shift the resonance frequency at large applied powers (known as amplitude-frequency dependency). Further

increase in the applied power will push the resonator to the bifurcation point at which the transmission plot exhibits hysteresis [62]. Previously, it was presumed that at or beyond the bifurcation, the oscillator becomes unstable and its performance degrades. Recently, stable oscillators have been reported that are believed to drive the resonator into the nonlinear operation region and preliminary results show that the phase noise continues to improve even in this range [60, 61].

Piezoelectrically-transduced resonators offer larger electromechanical coupling coefficient relative to that of electrostatic resonators, which results in achieving lower motional resistance [9, 10]. Furthermore, the need for large polarization voltages is eliminated due to the self-generating property of piezoelectric transduction. TPoS resonators are a subcategory of piezoelectric resonators with superior power handling and high quality factors [15]. This makes TPoS technology a suitable candidate for implementing very stable oscillators operating at high vibration amplitudes.

The oscillator presented here comprises a two-port ~27MHz TPoS resonator with high Q in air and a commercially available wide bandwidth amplifier in an inverting configuration. The oscillation power is simply increased by incrementing the supply voltage of the circuit. It will be shown that the oscillator is most stable (exhibits lowest PN) when the resonator is operated at the bifurcation point. The reported close-to-carrier PN (@1kHz offset) is the lowest value reported to date in literature for MEMS oscillators.

Among works on nonlinear MEMS oscillators, a few have experimentally confirmed the nonlinear operation of the resonator in closed-loop [82, 83]. To examine the nonlinear operation



in closed-loop, the current through and the voltage across the port(s) of the device have to be measured simultaneously to collect the phase data at each operating frequency. Next, the admittance curve versus the oscillation frequency is generated. While previous works show the nonlinear operation of a one-port resonator in closed-loop, the effect of operation at or beyond bifurcation on the phase noise is not explicitly discussed. In this chapter, a simple practical method is presented to verify the operation at bifurcation in closed-loop and the corresponding effect on the PN is highlighted.

## 7.2. Resonator Characterization and Oscillator Design

The S-parameters of the resonator were measured using an Agilent E8358A PNA network analyzer, a pair of GSG probes, and an RF amplifier (Mini-Circuits® ZFL-2500VH). Prior to the measurements, short-open-load-thru (SOLT) calibration was carried out on a reference substrate to calibrate the measurement setup including the amplifier. All the measurements are performed at atmospheric pressure and ambient temperature.

The TPoS resonator of this work is a 5<sup>th</sup> order two-port design, fabricated on silicon substrate with unloaded  $Q > 10,000$  in air and a motional resistance of  $\sim 200$  at 27.7MHz. This resonator exhibits frequency softening as the applied power is increased. The transmission ( $S_{21}$ ) for different input powers is plotted in Figure 68.

To study the effect of self-heating on the nonlinear behavior of the resonator, the temperature increase in the resonator was estimated at bifurcation. First, the dissipated power ( $P_d$ ) in the resonator is determined at bifurcation to be 76mW [84]. Neglecting the convection and radiation,

the only source of heat loss in the body of the resonator is through the four tethers holding the device in place. Thus, the temperature increase in the resonator can be calculated using equation (2) where  $R_{th}$  is the thermal resistance of one tether.  $R_{th}$  is approximated by equation (3) where  $l$ ,  $w$ , and  $t$  are the length, width and the thickness respectively and  $k$  is the material thermal conductivity.

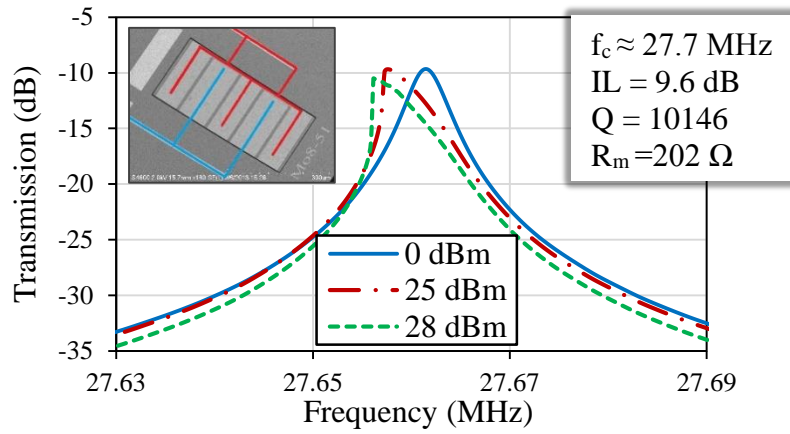


Figure 68: Frequency response of the TPoS resonator of this work at different applied powers. Inset: SEM of the resonator signifying the ports in colors.

$$\Delta T = P_d * R_{th} * \frac{1}{4} \quad (34)$$

$$R_{th} = \frac{l}{w * (t_{AlN} k_{AlN} + t_{Si} k_{Si})} \quad (35)$$

After substituting the values, the maximum temperature increase at bifurcation is slightly larger than 2°C which would be equivalent to less than  $-60ppm$  shift in the resonance frequency. Considering that the calculated temperature change is an overestimation when ignoring the convection, the measured  $-105ppm$  frequency shift at bifurcation indicates that the self-heating

is only partially responsible for the frequency shift at high powers and the elastic nonlinearities are the primary contributor.

The oscillator as pictured in Figure 69 incorporates a wide bandwidth amplifier (TI THS4211) in the inverting configuration. This amplifier can operate with supply voltages up to 15V ( $\pm 7.5V$ ). The loop gain is set to 10 by  $R_2$  and  $R_3$  and the resonator is placed in the feedback loop through its two ports. The three-fingered port (marked in red on the inset of Figure 68) is connected to the oscillator output and the two-fingered port (marked in blue) is connected to the input of the oscillator while the bottom metal plate is connected to the circuit ground.

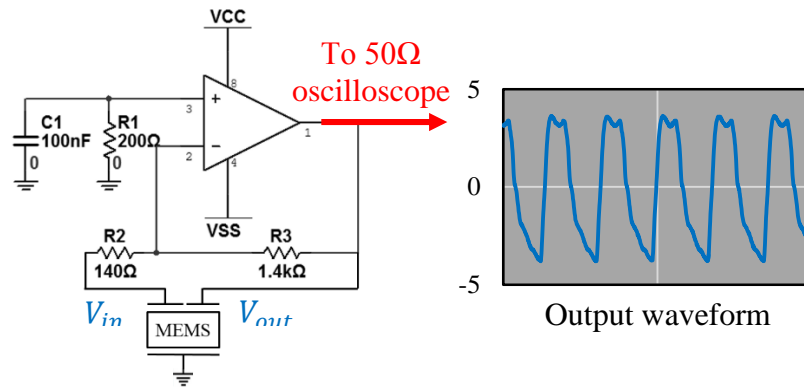


Figure 69: Schematic of the oscillator circuit. The inset on the right shows the output waveform with  $\pm 5.5$  supply voltage.

### 7.3. Oscillator Phase Noise

In order to drive the resonator into the nonlinear regime the supply voltage of the circuit and hence the oscillation voltage amplitude ( $V_{out}$ ) are increased gradually (Figure 70). Due to the asymmetry of the resonators' input and output ports and the impedances connected to them, this 5<sup>th</sup>-order resonator acts as a voltage step-up transformer as described in chapter 6. Hence, the

voltage on the two-fingered port ( $V_{in}$ ) is larger [85]. The oscillation frequency reduces as expected considering the observed frequency softening in the frequency response of the resonator (Figure 68). Both the oscillation frequency and PN are plotted versus the oscillation amplitude in Figure 71.

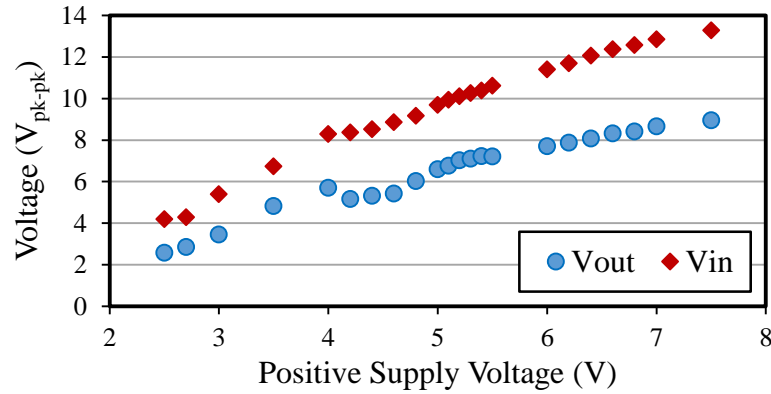


Figure 70: Voltages on the input and output ports of the resonator in closed-loop versus the positive supply voltage, showing a steady increase as the supply voltage is increased.

The impaired PN below  $6V_{pk-pk}$  ( $|V_{supply}| < 5V$ ) is believed to be due to the existence of subharmonic oscillation of the order of  $1/2$ , which is the result of asymmetrical nonlinearities of the system [86]. The subharmonic oscillation, disappears when the  $V_{supply}$  is increased beyond  $\pm 5V$ . After this point, the close- and far-from-carrier PN values improve until they reach their lowest values when the oscillation voltage is around  $7.2V_{pk-pk}$ . PN is plotted in Figure 72 for offset frequencies from 10Hz to 5MHz for  $|V_{supply}|$  greater than 4V. The increase in the PN at small offsets from the carrier (@10Hz) for oscillation amplitudes larger than  $\sim 7V_{pk-pk}$  is not well understood at this point and requires further investigation. It is speculated that it is either the result of external factors [83] with the most dominant one being the temperature fluctuations since the

uncompensated TPoS resonators such as the one used in this paper have relatively large temperature coefficient of frequency [34], or it is due to the resonator nonlinearities as is discussed for quartz resonators [87]. The lowest measured PN plot is illustrated in Figure 73 along with the equivalent PN normalized to 10MHz. RMS jitter was measured from 12kHz to 5MHz to be  $290\text{ fsec}$ .

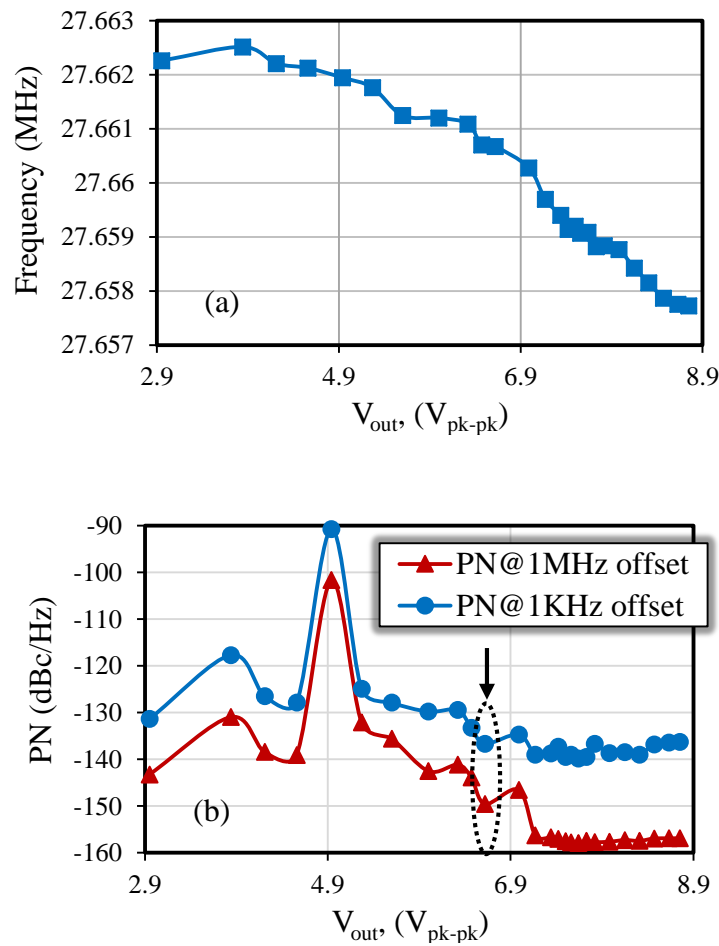


Figure 71: (a) Oscillation frequency and (b) Phase noise at 1KHz and 1MHz offset frequencies from the carrier versus the oscillator output voltage showing a noticeable drop at  $7.2V_{pk-pk}$ .

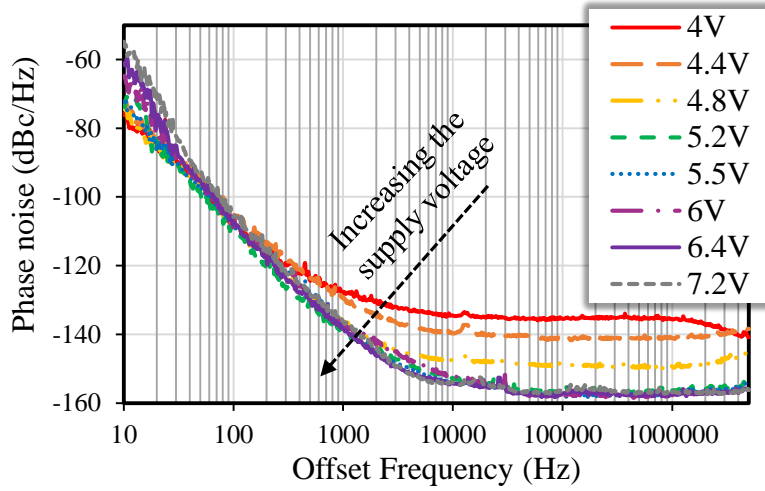


Figure 72: Phase noise plots for supply voltages greater than 4V showing a steady decrease as the voltage is increased.

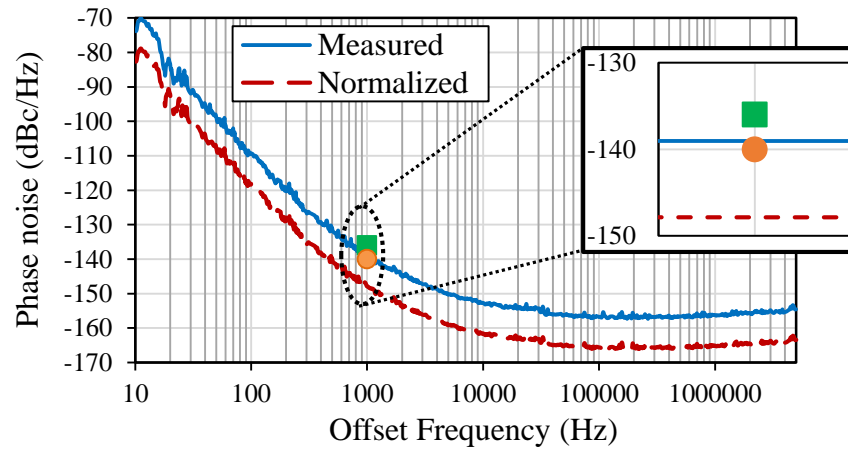


Figure 73: Measured and normalized (to 10MHz) phase noise plots of the oscillator with oscillation voltage of  $7.2V_{pk-pk}$ . The square and circle represent the best normalized phase noise values reported in literature for MEMS piezoelectric [79] and capacitive [80] oscillators respectively.

#### 7.4. Verification of the Nonlinear Operation in Closed-Loop

A new method is introduced to understand the closed-loop behavior of the resonator based on the correlation between the frequency shift and the applied power. First, the resonance frequency and the output voltage of the resonator were recorded for a wide range of applied power in an open loop configuration. Power was applied to the three-fingered port by the network analyzer and the output voltage was measured with a high frequency probe at the two-fingered port once with  $50\Omega$  and again with an open termination (Figure 74-a). The resonator was driven to the edge of bifurcation by increasing the applied power. The measured  $S_{11}$  data for both terminations is plotted in Figure 74-b. The slight frequency difference as indicated on the plot, is the result of altered stiffness of the piezoelectric film when terminated to different impedances [88]. The frequency softening starts at lower applied power for a larger termination due to the stronger induced electric field on the output port and thus the larger energy density stored in the resonator.

Next, to make a fair comparison between the open- and closed-loop measurements the normalized frequency shift ( $\frac{\Delta f}{f_0}$ ) is plotted versus the voltage on the two-fingered port (Figure 75). Just before the bifurcation point, the resonator exhibits  $\frac{\Delta f}{f_0}$  of  $-9 \times 10^{-5}$  with both  $50\Omega$  and open terminations. This value of the normalized frequency shift corresponds to a peak-to-peak oscillation voltage around  $7.2V$  for the closed-loop measurement, and that coincides with the PN reaching its minimum value after a significant drop as indicated by the arrow on Figure 71-b. This proves that the oscillator exhibits the lowest close-to-carrier PN at and beyond the bifurcation of the TPoS resonator.

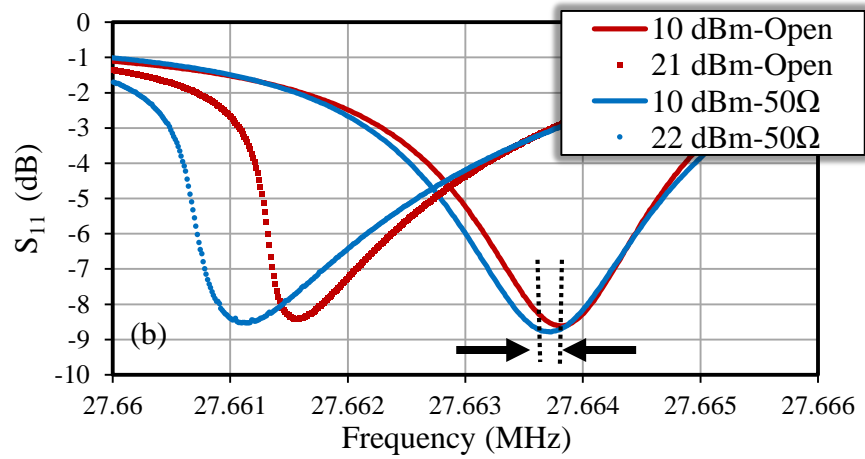
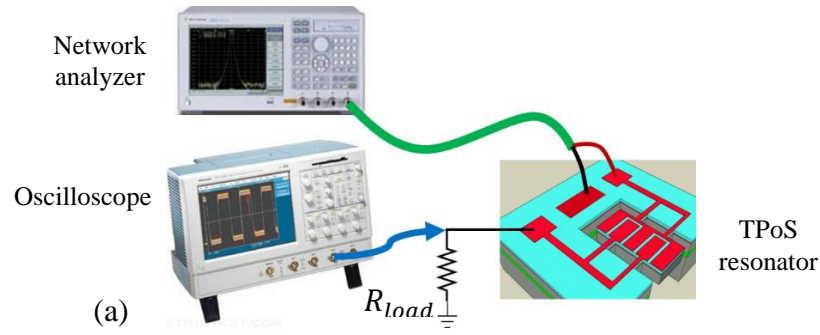


Figure 74: (a) Schematic of the one-port measurement setup. (b)  $S_{11}$  plots in linear region and at the edge of bifurcation measured with 50 $\Omega$  and open termination. Note the slight frequency difference between the two cases indicated at 10dBm input power.



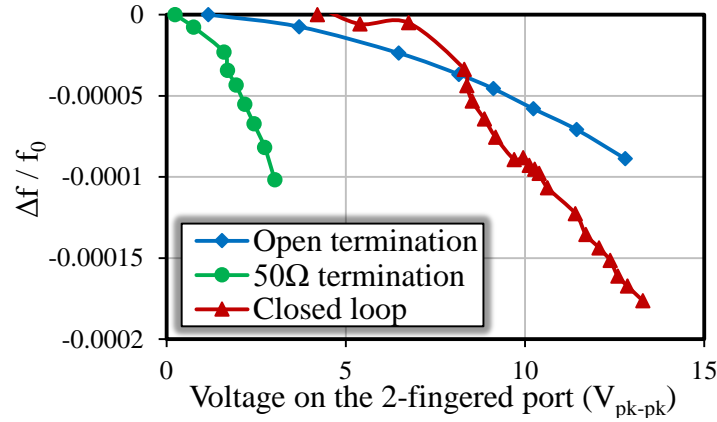


Figure 75: Normalized frequency shift ( $\frac{\Delta f}{f_0}$ ) vs. the output voltage (the voltage on the two-fingered port) of the resonator.

## 7.5. Conclusion

A 27MHz oscillator is built incorporating a thin-film piezoelectric-on-substrate MEMS resonator. The resonator is driven into the nonlinear region in closed-loop by increasing the supply voltage of the circuit. It is shown that the lowest phase noise is achieved when the resonator is operating at or beyond its bifurcation point. A phase noise of -139 dBc/Hz at 1kHz offset from the carrier is reported which is equivalent to -148 dBc/Hz when normalized to 10MHz and is the lowest value reported to date for MEMS resonators. The far-from-carrier phase noise is -157 dBc/Hz and the jitter is 290  $fsec$  measured from 12KHz to 5MHz.

## **CHAPTER EIGHT: PASSIVE WIRELESS TEMPERATURE SENSOR USING A TPoS RESONATOR**

### **8.1. Introduction**

Resonant sensors have become a common solution for sensing many physical parameters such as pressure, temperature, viscosity, mass, etc. The primary advantage of resonant sensors is that their output is a frequency or a phase change which can be directly fed into digital circuits unlike analogue sensors [89].

Wireless temperature sensors are growing in popularity in industrial, commercial, healthcare, and even residential settings [90]. Furthermore, there is a high demand for passive wireless temperature sensing in a variety of applications like inaccessible locations and hazardous environments where long lifetime is essential [91] or harsh environments where battery lifetime is excessively shortened. The first remote temperature sensors introduced by Bao *et al* in 1987, employed surface acoustic wave (SAW) devices [92]. Since then a variety of such devices have been developed and are widely used [91, 93, 94].

Conventionally, piezoelectric crystals such as  $\text{LiNbO}_3$  or quartz were exploited to fabricate resonant temperature sensors [95]. The high temperature sensitivity of specific crystalline cuts of quartz has enabled sensors with very high resolution ( $0.001^\circ\text{C}$ ) [96]. The drawback, however is their relatively large size and incompatibility of their fabrication process with the mature silicon micro-fabrication technology. In this sense, silicon micromachined sensors are of particular interest due to their small size and the potential for high-volume production at very low cost [97].

Temperature-dependent quartz, SAW, and MEMS resonators have all been incorporated in oscillator circuits to yield temperature sensors with very high resolution [96, 98, 99]. The drawback of an oscillator-based sensor is the relatively large power dissipated in the circuit compared to the power dissipated in the low-loss resonator [89]. On the other hand, the electronic circuitry may limit the performance of the sensor by increasing the noise floor.

In summary, the most important characteristics of a resonator that yields to an efficient passive wireless temperature sensor are as follows: (I) There is no need for bias voltages for operation of the resonator to simplify the passive operation, (II) the temperature-dependency of the resonant frequency has to be substantial to guarantee high resolution, (III) the motional resistance of the resonator has to be small in order to minimize the power loss in the resonator and consequently increase the sensing distance, (IV) the  $Q$  of the resonator should be high to improve the signal to noise ratio and therefore achieve a higher temperature resolution.

Piezoelectrically-transduced MEMS resonators do not require a bias voltage to operate and offer larger electromechanical coupling coefficient relative to that of electrostatic resonators, which ultimately results in a lower motional resistance [9, 10]. Thin-film piezoelectric-on-silicon (TPoS) resonators are a subcategory of piezoelectric resonators that exhibit high quality factors [15]. The resonant frequency of TPoS resonators is defined by the lateral dimensions of the resonator which enables fabrication of a wide frequency range on a single substrate. Furthermore, the TCF can be engineered by changing the orientation of the resonator or doping the silicon layer [34]. Correspondingly, TPoS technology is a suitable candidate for implementing passive wireless temperature sensors.

While thin-film piezoelectric MEMS resonators offer smaller size and lower manufacturing/packaging cost compared to their SAW counterparts, no sensor system has been reported that utilizes MEMS resonators in a passive or a wireless configuration. This work is the first to demonstrate a passive wireless temperature sensor using a 990MHz TPoS resonator.

The chapter is organized as the following. The next section will discuss the TPoS resonator and its frequency and temperature characteristics. The measurement setup and the sensor readout scheme will be explained afterwards followed by the experimental results. Discussion and conclusion will be in the succeeding sections.

## **8.2. TPoS Resonator**

The TPoS resonator comprises a thin piezoelectric film sandwiched between two metal layers stacked on top of a silicon film (Figure 76-a). Readers can refer to chapter 4 for the detailed fabrication process. The suspended resonator is anchored to the substrate by tethers placed at zero-displacement nodes. The top metal is patterned so that the top electrodes mimic the stress field in the structure at (Figure 76-b) a targeted resonant mode. The piezoelectric film is actuated by the electric field applied between the two metal layers and consequently an acoustic wave is launched in the bulk of the device.

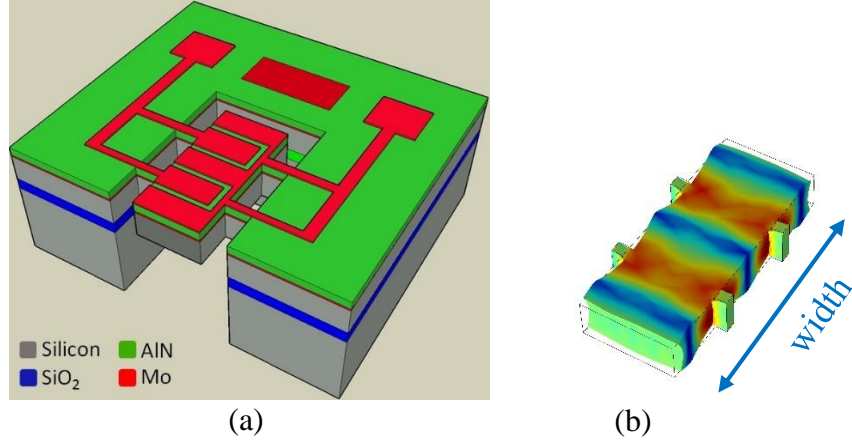


Figure 76: (a) The schematic of a 5<sup>th</sup> order TPoS resonator and (b) the stress profile of a silicon slab with two pairs of fixed tethers at the 5<sup>th</sup> order width-extensional mode.

TPoS resonators offer high  $Q$  and low motional resistance all in a very small footprint [94, 96]. These resonators can be designed in either one-port or two-port configuration. In a two-port design, the resonator is excited through one of the ports and the other port is used to sense the vibration. Whereas in a one-port configuration, both excitation and sensing are done through one of the ports while the second port can be exploited to tune the resonance frequency [88].

Figure 77 shows the frequency response of a 21<sup>st</sup> order resonator used in this work. This TPoS device which was fabricated on a silicon substrate exhibits  $Q$  of 2900 in air and motional resistance of  $147\Omega$  at 990MHz. The impulse response of a resonator decays exponentially ( $e^{-t/\tau}$ ) where the time constant  $\tau$  is equal to  $\frac{2Q}{\omega_0}$  by definition [100]. This implies that the envelope of the response decreases by 98% in  $4\tau$  seconds. The high  $Q$  of this resonator results in a relatively long decay time of  $4\mu\text{s}$ .

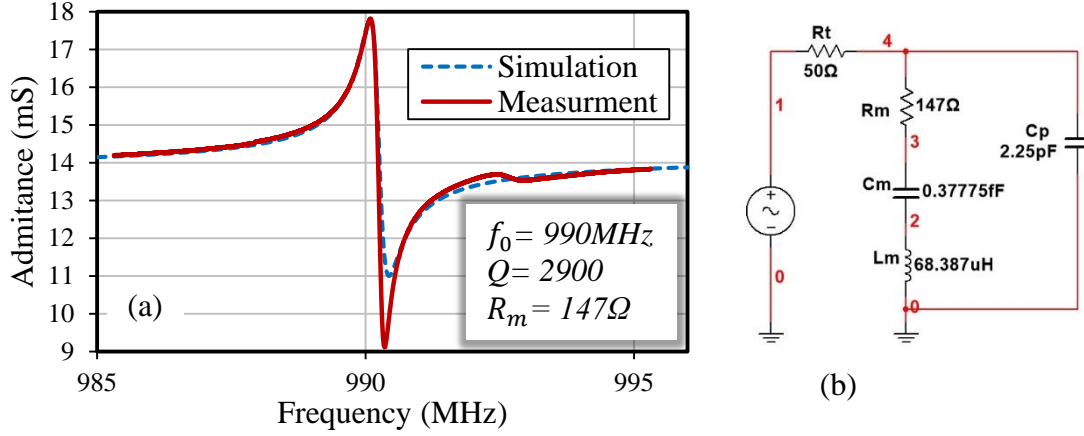


Figure 77: (a) Frequency characteristics and (b) the equivalent circuit model of the one-port TPoS resonator.

The sensitivity of the resonator to temperature is a function of device's TCF as follows:

$$f = (TCF \cdot \Delta T + 1) \cdot f_0 \quad (36)$$

which is in turn a function of the stack materials and could be approximated according to the below equation:

$$TCF_{total} = \frac{TCF_{Mo} \cdot t_{Mo} + TCF_{AlN} \cdot t_{AlN} + TCF_{Si} \cdot t_{Si}}{t_{Mo} + t_{AlN} + t_{Si}} \quad (37)$$

where  $t$  denotes the corresponding film thickness.

In order to realize a temperature sensor with high resolution, large TCF values are desirable. This is achieved by using an un-doped or very lightly-doped silicon as the starting substrate [97]. The resonator of this work is fabricated on a 5  $\mu\text{m}$  Boron-doped silicon substrate with fairly low resistivity of 1-20  $\Omega \cdot \text{cm}$ . To characterize the resonator's TCF, it was placed in a temperature-controlled chamber and heated up from room temperature to +85°C in 5°C increments while the

resonance frequency was recorded using a network analyzer (Rhode & Schwarz-ZNB8) in a one-port configuration. A linear TCF of  $-30 \text{ ppm}/^{\circ}\text{C}$  was measured for this temperature range.

### 8.3. Wireless Measurement Setup

To utilize a resonator as a wireless temperature sensor, the resonator is interrogated by a pulse-modulated sinusoidal signal which forces the resonator into oscillation. Next, the resonator decay response is captured and evaluated to determine the temperature.

A schematic view of the setup is shown in Figure 78. The RF signal generator transmits a pulse-modulated sine wave through a 3dBi antenna. The device under test (DUT) is interrogated during the pulse on-time and its response is analyzed during the off-time. The DUT, directly connected to a 5dBi antenna with no additional circuitry, is forced into oscillation upon receiving the interrogation signal. The interrogation period (on-time) is long enough for the resonator to reach its maximum oscillation amplitude. If the frequency of the sine wave is equal to the natural resonance frequency of the resonator, the amplitude of oscillations will be maximized. The frequency of the sine wave can be dynamically tuned during the interrogation to match the resonance frequency in order to maximize the amplitude of the resonator response and thus guarantee a larger signal to noise ratio. At the end of the pulse, the resonator's oscillation amplitude starts to decay over a period of  $4\tau$  as explained in the previous section. An oscilloscope with a high sampling rate (Rhode & Schwarz-RTO1024) is used to collect the signal in real time (see the signal received at the oscilloscope antenna in Figure 78). A 5dBi antenna is connected to the oscilloscope. Figure 79 exhibits the waveform received by the oscilloscope showing the

interrogation signal and the resonator response. Note that the much stronger interrogation signal is directly received from the RF generator during the on-time.

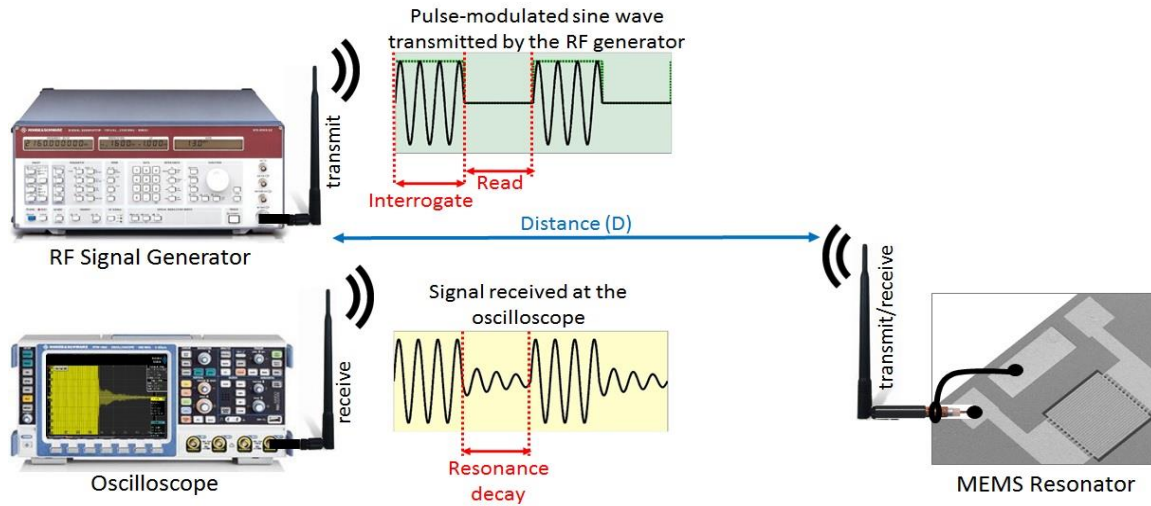


Figure 78: Measurement setup of the wireless temperature sensor. The MEMS resonator on the right is a 21<sup>st</sup> order multi-tether design and is directly connected to an antenna.

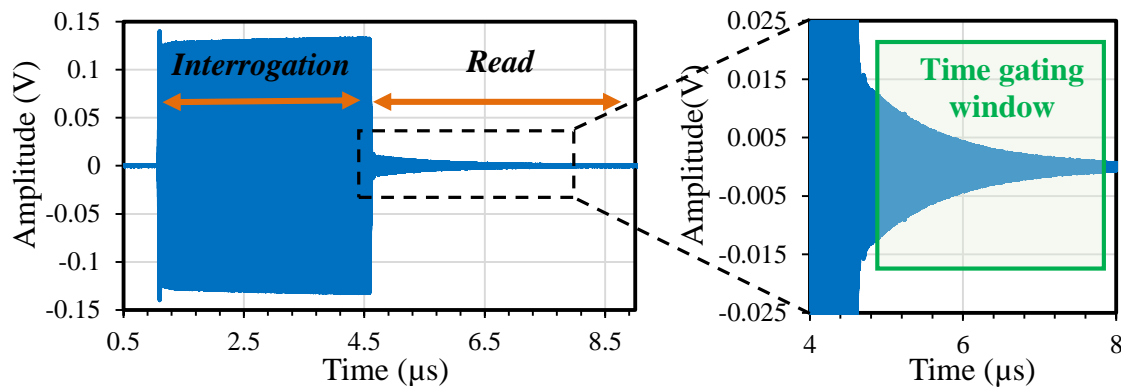


Figure 79: Waveform as received by the oscilloscope showing the interrogation signal and the resonator response. The measurement was performed at room temperature and transmit power of 0.5W at 10cm sensing distance. The inset shows the portion of the signal that is time gated for further processing.



In order to eliminate the interrogation signal at the receiver, the waveform is gated in time domain (Figure 79-b). An additional 200ns after the end of the interrogation pulse is ignored to account for the environmental echoes. A fast Fourier transform (FFT) is then taken on the signal using Labview software in order to extract the resonance frequency of the resonator (Figure 80). The temperature can then be calculated according to equation (5).

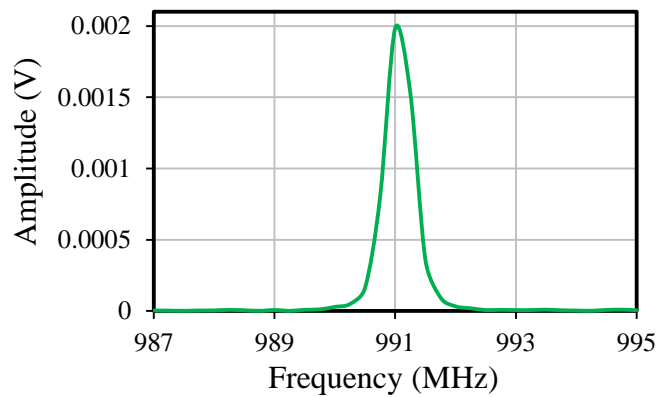


Figure 80: The spectral density of the resonator decay response after taking Fourier transform of the time-gated waveform of Figure 79-b.

#### 8.4. Experimental Results

In order to characterize the passive temperature sensor, the resonator is put into the temperature-controlled chamber and connected to an antenna on the outside. The wireless configuration described in section 8.3 is used to measure the frequency variations over the same temperature range as before. The interrogation signal power was set to 500mW and distance (D) set to 1m. Figure 81 compares the results of direct and wireless measurements.

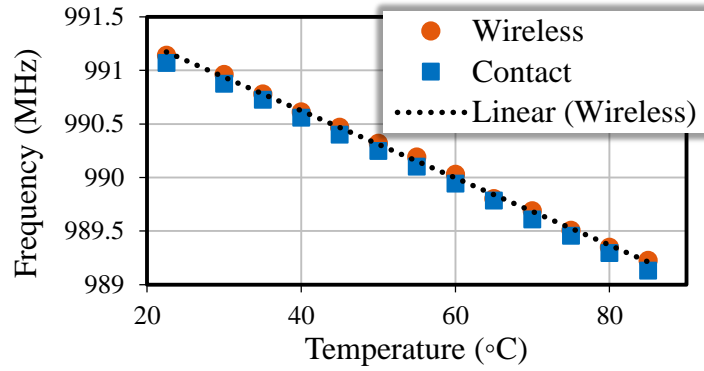


Figure 81: The resonance frequency vs. the resonator's temperature measured in direct and wireless configurations with TCF of  $-30\text{ppm}/^{\circ}\text{C}$ . The slight frequency shift between the two cases is due to different loading on the resonator.

The very short time required for each temperature reading ( $\sim 7\mu\text{s}$ ) enables collecting numerous samples in a very short period of time. Figure 81 shows the temperature histogram of 2000 samples with a mean value of  $22.27^{\circ}\text{C}$  and standard deviation (STD) of  $0.07^{\circ}\text{C}$  resulting in temperature resolution of less than  $0.1^{\circ}\text{C}$  which was also verified by experiment. In addition, a maximum D of 3m was achieved with 500mW power, though the resolution reduced to  $0.6^{\circ}\text{C}$ .

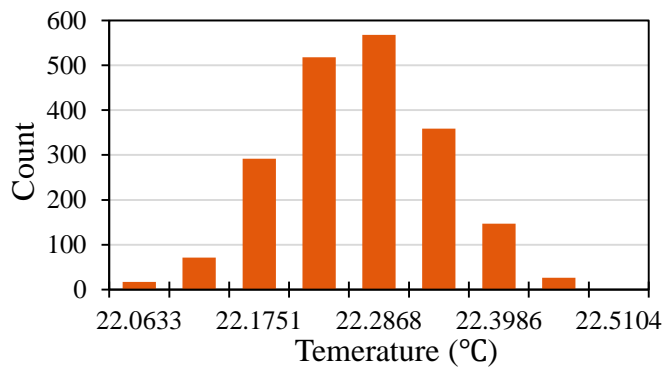


Figure 82: Histogram of 2000 temperature samples collected at room temperature.

## 8.5. Discussion

The temperature resolution is a function of signal to noise ratio at the receiving antenna (oscilloscope). Friis equation explains the dependency of the received signal power on different parameters [101]:

$$\frac{P_r}{P_t} = \frac{G_t^2 G_s^2 \lambda^4 \chi}{(4\pi D)^4} \quad (38)$$

where  $P_t$  and  $P_r$  are the power transmitted and received by the transceiver respectively.  $G_t$  and  $G_r$  are the gain of the interrogator and sensor antennas respectively,  $\lambda$  is the free-space wavelength, and  $\chi$  represents the mismatch losses. To further increase  $D$  without sacrificing the resolution, higher signal power could be used to interrogate the resonator. According to equation (7), the resolution achieved at 3m (0.6°C) can be maintained at twice the distance if the peak power is increased 16 times. However, the average power could easily be kept below a desired level by reducing the sampling rate.

## CHAPTER NINE: CONCLUSION

This last chapter is a brief conclusion of the work presented in this dissertation and also a short summary of the accomplishments. The last section is a survey about future research.

### 9.1. Accomplishments

This dissertation focused on performance optimization of lateral-mode thin-film piezoelectric-on-substrate (TPoS) resonators and filters. Both silicon and diamond are used as the substrate for fabrication of TPoS devices and their characteristics are compared. Ultrananocrystalline diamond (UNCD) was utilized as the substrate for fabricating TPoS devices in order to extend the resonance frequency beyond the limits achievable by silicon. The UNCD films were deposited using hot filament chemical vapor deposition method followed by two polishing steps in order to reduce the surface roughness to promote the growth of high quality aluminumnitride thin films. Three UNCD substrates with different Young's modulus were used to reach frequencies up to two times that of devices fabricated on silicon with the same geometries. The temperature coefficient of frequency for TPoS resonators fabricated on UNCD substrate is measured to be less than -10 ppm/°C which is much lower than the devices fabricated on silicon. Also, diamond devices are shown to have a better power handling capability and can withstand higher energy densities.

One of the main objectives was to improve the insertion loss and increase the bandwidth of the monolithic TPoS filters. A FEM model is employed to evaluate the effect of lateral dimensions and support configuration on the performance of the TPoS devices. Various TPoS filters were designed and fabricated with different lateral dimensions and number of tethers to evaluate the

accuracy of the FEM model and to optimize the performance. A monolithic lateral-mode filter is reported with a record low insertion loss of 2.6 dB at 900MHz and  $FBW_{3dB}$  of 0.09% when terminated with standard  $50\Omega$ . A novel filter design was presented with a relatively large fractional bandwidth of 1% in a small footprint.

TPoS resonators with high quality factor were employed to build a very low-noise oscillator. The high Q and large TCF of the TPoS resonators was also exploited in order to realize a passive wireless temperature sensor.

## 9.2. Future Research

TPoS resonators are demonstrated as suitable candidates for passive wireless sensing of temperature. The next step would be integration of TPoS resonators with antennas. The small size and low cost of TPoS resonators renders them applicable for disposable sensors which are highly desired in medical applications like monitoring the patient's vitals such as body temperature and blood pressure.

TPoS resonators can be configured to be sensitive to absolute pressure. One such design is presented in the schematic of Figure 83. Similar to the work in [102 and 103], the pressure sensor is composed of a free-standing silicon membrane with a stack of Mo/AlN/Mo on top to excite a bulk acoustic wave (BAW) in the membrane. The resonance frequency of the structure is essentially defined by the thickness of the AlN. Any deformation of the membrane due to external factors such as pressure would result in a change in the resonance frequency of the structure.

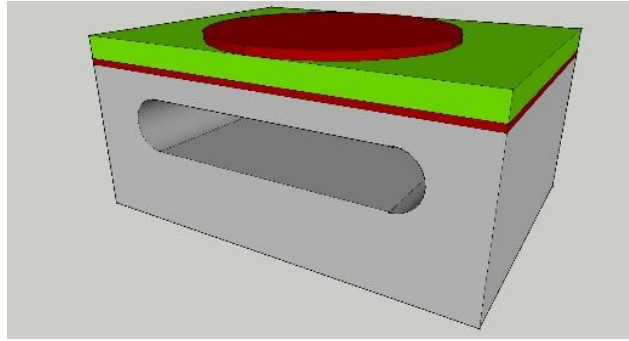


Figure 83: The cross-section of the proposed pressure sensor to measure the absolute value of the pressure. The resonant disk is suspended by forming a cavity in the substrate.

In order to measure the absolute value of the pressure, the pressure change has to be compared to a known pressure value. By using the Empty-Space-in-Silicon Formation Technique described in [104], silicon-on-nothing (SiON) structures can be formed. Since the process is done at a known pressure, the absolute value of the pressure can be calculated by measuring the frequency shift of the resonator.

Hence, a MEMS sensor platform is suggested that incorporates both TPoS temperature and pressure sensors. Figure 84 shows a schematic of such sensor platform. The proposed sensor platform is essentially based upon two key competencies. First, is our thin-film piezoelectric-on-substrate (TPoS) resonator technology and second is the capability of interrogating the resonator in a passive wireless configuration.

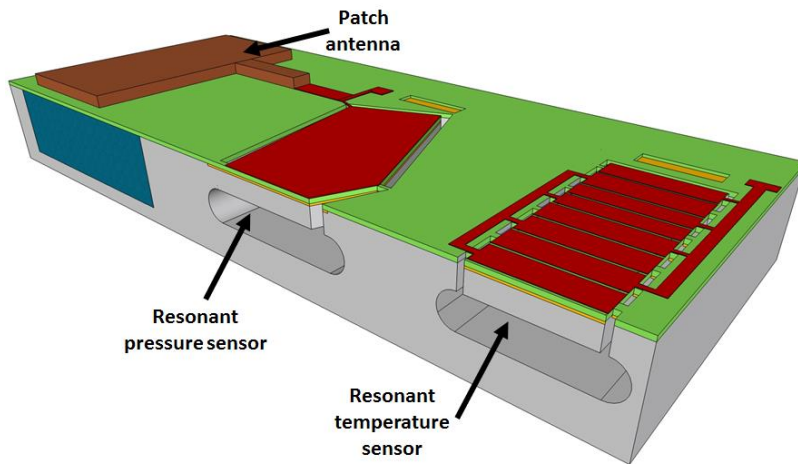


Figure 84: A proposed MEMS sensor platform with passive temperature and pressure sensors. Both sensors are directly connected to a patch antenna and send/receive the signal.

Another research opportunity is the hourglass filters. These filters with 1% fractional bandwidth demonstrates the potential of the TPoS technology for direct channel-select applications. A thorough understanding of the operation mechanism of such filters is required. Future work would focus on improving the insertion loss of these filters and possibly further increase the bandwidth.

In general, the lateral-mode piezoelectric resonators based on AlN have small coupling coefficient limiting the maximum achievable bandwidth. An alternative solution would be use of other piezoelectric materials, e.g. PZT with higher piezoelectric coefficient.

## LIST OF REFERENCES

- [1] T. McClelland, J. Zacharski, C. Szekely, E. Mauskop, D. Bogomolov; "Low phase noise quartz BAW oscillator for space applications," Joint Conference of the IEEE International Frequency Control and the European Frequency and Time Forum (FCS), pp.1-5, 2-5 May 2011.
- [2] M. E. Frerking; "Spurious Oscillation in Crystal Oscillators," *20th Annual Symposium on Frequency Control*. pp.501-516, 1966.
- [3] D. Kenny and R. Henry, "Comparative Analysis: MEMS vs. Traditional Quartz Oscillators," *Electronics Products Magazine*, April 2009.
- [4] C. T.-C. Nguyen; "MEMS technology for timing and frequency control," *IEEE Transactions on Ultrasonics, Ferroelectrics and Frequency Control*, vol.54, no.2, pp.251-270, Feb. 2007.
- [5] J. Wang, Z. Ren, and C. T.-C. Nguyen, "1.156-GHz self-aligned vibrating micromechanical disk resonator," *IEEE Transactions on Ultrasonics, Ferroelectrics, and Frequency Control*, vol. 51, no. 12, pp. 1607-1628, Dec. 2004.
- [6] J. R. Clark, H. Wan-Thai, and C. T.-C. Nguyen; "High-Q VHF micromechanical contour-mode disk resonators," *Technical Digest of Electron Devices Meeting (IEDM)*, pp.493-496, Dec. 2000.
- [7] L. Yu-Wei, L. Sheng-Shian, X. Yuan, R. Zeying, and C. T.-C. Nguyen; "Vibrating micromechanical resonators with solid dielectric capacitive transducer gaps," *Proceedings of IEEE International Frequency Control Symposium*, pp. 128-134, Aug. 2005.
- [8] S. Pourkamali, A. Hashimura, R. Abdolvand, G. K. Ho, A. Erbil, and F. Ayazi, "High-Q single-crystal silicon HARPSS capacitive beam resonators with self-aligned sub-100-nm transduction gaps," *J. Microelectromech. Syst.*, vol. 12, no. 4, pp. 487-496, Aug. 2003.



- 
- [9] R. Abdolvand, H. Lavasani, G. Ho, F. Ayazi; "Thin-film piezoelectric-on-silicon resonators for high-frequency reference oscillator applications," *IEEE Transactions on Ultrasonics, Ferroelectrics and Frequency Control*, vol.55, no.12, pp.2596-2606, Dec. 2008.
- [10] G. Piazza, P. J. Stephanou, and A. P. Pisano; "One and Two Port Piezoelectric Contour-Mode MEMS Resonators for Frequency Synthesis," *Proceeding of the 36th European Solid-State Device (ESSDERC 2006)*, pp.182-185, Sep. 2006.
- [11] H. Fatemi, B. P. Harrington, H. Zeng, J. Carlisle, and R. Abdolvand, "50 $\Omega$ -Terminated 900MHz Monolithic Lateral-Extensional Piezoelectric Filters on Ultrananocrystalline Diamond," in *Proceedings of IEEE International Conference on Micro Electro Mechanical Systems (MEMS 2011)*, 23-27 January 2011.
- [12] B.P. Harrington, M. Shahmohammadi, and R. Abdolvand; "Toward ultimate performance in GHZ MEMS resonators: Low impedance and high Q," *IEEE International Conference on Micro Electro Mechanical Systems (MEMS)*, pp.707-710, Jan. 2010.
- [13] G. Piazza, P. J. Stephanou, J. P. Black, R. M. White, and A. P. Pisano; "Single-chip multiple-frequency RF microresonators based on aluminum nitride contour-mode and FBAR technologies," *IEEE Ultrasonics Symposium*, vol.2, pp. 1187- 1190, Sep. 2005.
- [14] M. Rinaldi, C. Zuniga, Z. Chengjie, G. Piazza; "AlN contour-mode resonators for narrow-band filters above 3 GHz," *IEEE International Frequency Control Symposium Joint with the 22nd European Frequency and Time forum*, pp.70-74, Apr. 2009.
- [15] M. Shahmohammadi, B.P. Harrington, and R. Abdolvand, "Concurrent enhancement of Q and power handling in multi-tether high-order extensional resonators," *IEEE International Microwave Symposium*, pp. 1452-1455, May 2010.

- 
- [16] C. K. Campbell; "Applications of surface acoustic and shallow bulk acoustic wave devices," *Proceedings of the IEEE*, vol.77, no.10, pp.1453-1484, Oct 1989.
- [17] T. Matsuda, H. Uchishiba, O. Ikata, T. Nishihara, and V. Satoh; "L and S band low-loss filters using SAW resonators," *IEEE Ultrasonics Symposium Proceedings*, vol.1, pp.163-167, 1994.
- [18] F. S. Hickernell, and H. D. Knuth; "The use of design of experiments for the optimization of deposited glass on SAW filters," *Joint Meeting of the European Frequency and Time Forum and the IEEE International Frequency Control Symposium*, vol.2, pp.950-953, 1999.
- [19] A. L. de Escobar, W. C. McGinnis, M. J. Pulling, and H. J. Whitehouse; "SAW filters for Global Positioning Satellite (GPS) receivers," *IEEE Position Location and Navigation Symposium*, pp. 4-11, 2002.
- [20] R. Ruby, P. Bradley, J. Larson, Y. Oshmyansky, and D. Figueredo; "Ultra-miniature high-Q filters and duplexers using FBAR technology," *IEEE International Solid-State Circuits Conference (ISSCC)*, pp.120-121, 438, 2001.
- [21] D. Feld, K. Wang, P. Bradley, A. Barfknecht, B. Ly, and R. Ruby; "A high performance 3.0 mm  $\times$  3.0 mm  $\times$  1.1 mm FBAR full band Tx filter for U.S. PCS handsets," *IEEE Ultrasonics Symposium*, vol.1, pp. 913-918 2002.
- [22] R. Ruby, P. Bradley, D. Clark, D. Feld, T. Jamneala, and K. Wang; "Acoustic FBAR for filters, duplexers and front end modules," *IEEE Microwave Symposium Digest*, vol.2, pp. 931-934, 2004.
- [23] K. M. Lakin, J. R. Belsick, J. P. McDonald, K. T. McCarron, and C. W. Andrus, "Bulk acoustic wave resonators and filters for applications above 2 GHz," *Microwave Symposium Dig.*, vol. 3, pp. 1487-1490, 2002.

- 
- [24] M. Weinberg, R. Candler, S. Chandorkar, J. Varsanik, T. Kenny, and A. Duwel; "Energy loss in MEMS resonators and the impact on inertial and RF devices," *International Solid-State Sensors, Actuators and Microsystem (Transducers)*, pp.688-695, June 2009.
- [25] S. O. Reza Moheimani and Andrew J. Fleming, "Piezoelectric Transducers for Vibration Control and Damping," *Advances in Industrial Control*, Springer-Verlag London, 2006.
- [26] Q. Chen, and Q. M. Wang; "The effective electromechanical coupling coefficient of piezoelectric thin-film resonators," *Applied Physics Letters*, 86, 022904, 2005.
- [27] IEEE Standard on Piezoelectricity," *ANSI/IEEE Std 176-1987* , pp.0\_1, 1988.
- [28] M. Onoe, H. F. Tiersten, and A. H. Meitzler; "Shift in the Location of Resonant Frequencies Caused by Large Electromechanical Coupling in Thickness-Mode Resonators," *Journal of Acoustical Society of America*, vol. 35, pp. 36-42, 1963.
- [29] M. A. Dubois and P. Mural; "Properties of aluminum nitride thin films for piezoelectric transducers and microwave filter applications," *Applied Physics Letters*, 74(20), December 1998.
- [30] R. S. Naik, J. J. Lutsky, R. Reif, and C. G. Sodini; " Electromechanical coupling constant extraction of thin-film piezoelectric materials using a bulk acoustic wave resonator," *IEEE Transactions on Ultrasonics, Ferroelectrics and Frequency Control*, vol.45, no.1, pp.257-263, Jan. 1998.
- [31] K. S. Sharma, S. Enjamuri, and K. C. J. Raju; "Effect of change in piezoelectric layer thickness in high-overtone bulk acoustic resonator," *Emerging Research Areas and 2013 International Conference on Microelectronics, Communications and Renewable Energy (AICERA/ICMiCR)*, pp.1-4, June 2013.
- [32] S. Prabhakar and S. Vengallatore; "Theory of thermoelastic damping in micromechanical

---

resonators with two-dimensional heat conduction," *Journal of Microelectromechanical Systems*, vol.17, no.2, pp.494-502, April 2008.

[33] H. Fatemi, H. Zeng, J. Carlisle, and R. Abdolvand; "Very low-loss high frequency lateral-mode resonators on polished ultrananocrystalline diamond," *Joint Conference of the IEEE International Frequency Control and the European Frequency and Time Forum (FCS)*, pp.1-5, May 2011.

[34] M. Shahmohammadi, B. P. Harrington, and R. Abdolvand; "Turnover Temperature Point in Extensional-Mode Highly Doped Silicon Microresonators," *IEEE Transactions on Electron Devices*, vol. 60, no. 3, pp. 1213-1220, March 2013.

[35] V. Kaajakari, "Practical MEMS," *Small gear publishing* 2009.

[36] Ch. Liu, "Foundations of MEMS," *Illinois ECE Series*, 2006.

[37] S. Gong; N. Kuo; G. Piazza; "GHz AlN lateral overmoded bulk acoustic wave resonators with a f.Q of  $1.17 \times 10^{13}$ ," *Frequency Control and the European Frequency and Time Forum (FCS)*, pp. 1-5, 2011.

[38] C. T.-C. Nguyen, "Vibrating RF MEMS overview: applications to wireless communications," *Proceedings, Photonics West: MOEMS-MEMS*, Paper No. 5715-201, Jan. 2005.

[39] Sh. Li; Y.W. Lin; Z. Ren, and C. T.-C. Nguyen; "A Micromechanical Parallel-Class Disk-Array Filter," *Frequency Control Symposium, Joint with the 21<sup>st</sup> European Frequency and Time Forum. IEEE International* , pp.1356-1361, May 2007

[40] G. Piazza, P. J. Stephanou, and A. P. Pisano; "Single-Chip Multiple-Frequency ALN MEMS Filters Based on Contour-Mode Piezoelectric Resonators," *Journal of Microelectromechanical Systems*, vol.16, no.2, pp.319-328, 2007.

- 
- [41] C. Zuo; N. Sinha, M. B. Pisani, C. R. Perez, R. Mahameed, and G. Piazza; "12E-3 Channel-Select RF MEMS Filters Based on Self-Coupled AlN Contour-Mode Piezoelectric Resonators," *IEEE Ultrasonics Symposium*, pp.1156-1159, 2007.
- [42] C. Zuo, N. Sinha, and G. Piazza; "Very high frequency channel-select MEMS filters based on self-coupled piezoelectric AlN contour-mode resonators, " *Sensors and Actuators A: Physical*, vol. 160, issues 1–2, pp. 132-140, May 2010.
- [43] P.J. Stephanou, G. Piazza, C.D. White, M. B. J. Wijesundara, and A. P. Pisano; "Mechanically Coupled Contour Mode Piezoelectric Aluminum Nitride MEMS Filters," *19<sup>th</sup> IEEE International Conference on Micro Electro Mechanical Systems (MEMS)*, pp.906-909, 2006.
- [44] H. Chandralalim, S. A. Bhav, R. G. Polcawich, J. S. Pulskamp, D. Judy, R. Kaul, and M. Dubey; "Fully-differential mechanically-coupled PZT-on-silicon filters," *IEEE Ultrasonics Symposium (IUS)*, pp.713-716, 2008.
- [45] C. Zuo; N. Sinha, and G. Piazza; "Novel electrode configurations in dual-layer stacked and switchable AlN contour-mode resonators for low impedance filter termination and reduced insertion loss," *IEEE 23<sup>rd</sup> International Conference on Micro Electro Mechanical Systems (MEMS)*, pp.719-722, Jan. 2010.
- [46] M. Rinaldi, C. Zuniga, C. Zuo, and G. Piazza; "Ultra-thin Super High Frequency two-port AlN contour-mode resonators and filters," *International Solid-State Sensors, Actuators and Microsystems Conference (TRANSDUCERS)*, pp.577-580, June 2009.
- [47] W. D. Beaver; "Theory and Design of the Monolithic Crystal Filter," *21<sup>st</sup> Annual Symposium on Frequency Control*, pp.179-199, 1967.
- [48] W. D. Beaver; "Monolithic Piezoelectric Filter Having Mass Loaded Electrodes for

---

Resonance Regions Acoustically Coupled Together" U.S. Patent No. 3,564,463. 1971.

[49] M. Onoe, H. Jumonji, and N. Kobori; "High Frequency Crystal Filters Employing Multiple Mode Resonators Vibrating In Trapped Energy Modes," *20<sup>th</sup> Annual Symposium on Frequency Control*, pp.266-287, 1966.

[50] R. C. Smythe, W. H. Horton, and R. B. Angove; "A note on VHF acoustically coupled bandpass crystal filters," *Proceedings of the IEEE*, vol. 55, no. 3, pp.422-423, 1967.

[51] R. Abdolvand, and F. Ayazi; "Monolithic Thin-Film Piezoelectric-on-Substrate Filters," *IEEE/MTT-S International Microwave Symposium*, pp.509-512, 2007.

[52] R. Abdolvand and F. Ayazi; "High Frequency Monolithic Thin-Film Piezoelectric-on-Substrate Filters," *International Journal of Microwave and Wireless Technologies*, vol. 1, issue 01, pp. 29-35, 2009.

[53] G. Bu, D. Ciplis, M. Shur, L. J. Schowalter, S. Schujman, and R. Gaska; "Electromechanical coupling coefficient for surface acoustic waves in single-crystal bulk aluminum nitride," *Applied Physics Letters*, 84, 4611, 2004.

[54] O. Auciello, S. Pacheco, A. V. Sumant, C. Gudeman, S. Sampath, A. Datta, R. W. Carpick, V. P. Adiga, P. Zurcher, M. Zhenqiang, H. Yuan; J. Carlisle, B. Kabius, J. Hiller, and S. Srinivasan, "Are Diamonds a MEMS' Best Friend?," *IEEE Microwave Magazine*, vol.8, no.6, pp.61-75, Dec. 2007.

[55] R. Abdolvand, G. K. Ho, J. Butler, and F. Ayazi, "ZnO-on-nanocrystalline diamond lateral bulk acoustic resonators," *IEEE International Conference on Micro Electro Mechanical Systems (MEMS)*, pp.795-798, Jan. 2007.

[56] R. Abdolvand, Zhili Hao, and F. Ayazi, "A Temperature-Compensated ZnO-on-Diamond

---

Resonant Mass Sensor," *IEEE Conference on Sensors*, pp. 1297-1300, Oct. 2006.

[57] W. Jing, J. E. Butler, D.S.Y. Hsu, and T.-C. Nguyen; "CVD polycrystalline diamond high-Q micromechanical resonators," *IEEE International Conference on Micro Electro Mechanical Systems*, pp.657-660, 2002.

[58] J. G. Rodríguez-Madrid, G. F. Iriarte, J. Pedrós, O. A. Williams, D. Brink, and F. Calle; "Super-High-Frequency SAW Resonators on AlN/Diamond," *IEEE Electron Device Letters*, vol. PP, no.99, pp.1-3,.

[59] M. Akgul, R. Schneider, Z. Ren, G. Chandler, V. Yeh, C. T. Nguyen; "Hot filament CVD conductive microcrystalline diamond for high Q, high acoustic velocity micromechanical resonators," *IEEE International Frequency Control and the European Frequency and Time Forum*, pp.1-6, May 2011.

[60]H. K. Lee, P. A. Ward, A. E. Duwel, J. C. Salvia, Y. Q. Qu, R. Melamud, S. A. Chandorkar, M. A. Hopcroft, B. Kim, T. W. Kenny; "Verification of the phase-noise model for MEMS oscillators operating in the nonlinear regime," *TRANSDUCERS*, pp. 510-513, 2011.

[ 61 ] M. Shahmohammadi, M.J. Modarres-Zadeh, and R. Abdolvand, "Low jitter thin-film piezoelectric-on-substrate oscillators," *IEEE International Frequency Control Symposium (IFCS)*, pp.613-617, June 2010.[62] V. Kaajakari, T. Mattila, A. Oja, and H. Seppa; "Nonlinear limits for single-crystal silicon microresonators," *J. Microelectromech. Syst.*, vol.13, no.5, pp.715- 724, Oct. 2004.

[63] V. Kaajakari, T. Mattila, J. Kiihamaki, H. Kattelus, A. Oja, and H. Seppa; "Nonlinearities in single-crystal silicon micromechanical resonators," *TRANSDUCERS*, vol.2, pp. 1574- 1577, 2003.

[64] C. Zuo, M. Rinaldi, and G.Piazza; "Power handling and related frequency scaling advantages

- 
- in piezoelectric AlN contour-mode MEMS resonators," *Ultrasonics Symp.*, pp. 1187-1190, 2009.
- [65] H. Fatemi, H. Zeng, J. Carlisle, and R. Abdolvand; "High frequency thin-film AlN-on-diamond lateral-extensional resonators," *Journal of Microelectromechanical Systems*, vol.22, no.3, pp.678-686, Jun. 2013.
- [66] B. P. Harrington and R. Abdolvand, "In-plane acoustic reflectors for reducing effective anchor loss in lateral-extensional MEMS resonators," *Journal of Micromech. Microeng.* vol. 21, no. 8, 2011.
- [67] G. Piazza, P. J. Stephanou, and A. P. Pisano, "Piezoelectric Aluminum Nitride Vibrating Contour-Mode MEMS Resonators," *Journal of Microelectromechanical Systems*, vol.15, no.6, pp.1406-1418, Dec. 2006.
- [68] R. H. Tancrell and M. G. Holland; "Acoustic Surface Wave Filters," *Ultrasonics Symposium* , pp.48-64, 1970
- [69] D. Malocha; "Surface acoustic wave design fundamentals," *Electrical and Computer Engineering Department, University of Central Florida*.
- [70] C. Zuo, J. Van der Spiegel, and G. Piazza; "Dual-Mode Resonator and Switchless Reconfigurable Oscillator Based on Piezoelectric AlN MEMS Technology," *IEEE Transactions on Electron Devices*, vol.58, no.10, pp.3599-3603, Oct. 2011.
- [71] S. R. Gilbert, R. Parker, M. K. Small, U. B. Koelle, J. D. Larson, and R. C. Ruby; "An ultra-miniature, low cost single ended to differential filter for ISM band applications," *IEEE MTT-S International Microwave Symposium Digest*, pp.839-842, 15-20 June 2008.
- [72] R. H. Olsson, K. E. Wojciechowski, M. R. Tuck, and J. E. Stevens; "Microresonant impedance transformers," *IEEE International Ultrasonics Symposium (IUS)*, pp.2153-2157, Sep. 2009.



- 
- [73] S. S. Bedair, J. S. Pulskamp, B. Morgan, and R. G. Polcawich; "Performance Model of Electrode Tailored Thin Film Piezoelectric Transformers for High Frequency Switched Mode Power Supplies," *Power MEMS*, pp. 436-438, 2009.
- [74] S. S. Bedair, J. S. Pulskamp, R. G. Polcawich, D. Judy, A. Gillon, S. Bhawe, and B. Morgan; "Low loss micromachined lead zirconate titanate, contour mode resonator with 50 $\Omega$  termination," *IEEE 25<sup>th</sup> International Conference on Micro Electro Mechanical Systems (MEMS)*, pp.708-712, 2012.
- [75] K. M. Lakin; "Modeling of thin film resonators and filters," *IEEE MTT-S International Microwave Symposium Digest*, vol.1, pp.149-152, 1-5 Jun 1992.
- [76] G. K. Ho, R. Abdolvand, A. Sivapurapu, S. Humad, and F. Ayazi; "Piezoelectric-on-Silicon Lateral Bulk Acoustic Wave Micromechanical Resonators," *Journal of Microelectromechanical Systems*, vol.17, no.2, pp.512-520, April 2008.
- [77] C.T. Nguyen and R. T. Howe, "An integrated CMOS micromechanical resonator high-Q oscillator," *IEEE Journal of Solid-State Circuits*, vol. 34, no. 4, pp. 440-455, Apr. 1999.
- [78] M. E. Frerking; "Fifty years of progress in quartz crystal frequency standards," *IEEE International Frequency Control Symposium*, pp.33-46, Jun 1996.
- [79] J. Hu, L. Callaghan, R. Ruby, and B. Otis; "A 50ppm 600MHz frequency reference utilizing the series resonance of an FBAR," *IEEE Radio Frequency Integrated Circuits Symposium (RFIC)*, pp.325-328, May 2010.
- [80] V. Kaajakari, T. Mattila, A. Oja, J. Kiihamaki, and H. Seppa; "Square-extensional mode single-crystal silicon micromechanical resonator for low-phase-noise oscillator applications," *IEEE Electron Device Letters*, vol.25, no.4, pp.173-175, April 2004.

- 
- [81] A. Hajimiri and T. Lee, "A general theory of phase noise in electrical oscillators," *J. Solid-State Circuits*, vol. 33, no.2, pp.179-194, Feb. 1998.
- [82] D.T. Chang, H.P. Moyer, R.G. Nagele, R.L. Kubena, R.J. Joyce, D.J. Kirby, P.D. Brewer, H.D. Nguyen, and F.P. Stratton; "Nonlinear UHF quartz MEMS oscillator with phase noise reduction," *IEEE International Conference on Micro Electro Mechanical Systems*, pp.781-784, Jan. 2013.
- [83] H.K. Lee, R. Melamud, S. Chandorkar, J. Salvia, S. Yoneoka, and T.W. Kenny; "Stable Operation of MEMS Oscillators Far Above the Critical Vibration Amplitude in the Nonlinear Regime," *Journal of Microelectromechanical Systems*, , vol.20, no.6, pp.1228-1230, Dec. 2011.
- [84] H. Fatemi and Reza Abdolvand, "Fracture limit in thin-film piezoelectric-on-substrate resonators: Silicon VS. diamond," *Int'l Conference on MicroElectroMechanical Systems (MEMS)*, pp.461-464, Jan. 2013.
- [85] H. Fatemi and Reza Abdolvand; "High-frequency thin-film piezoelectric transformers," *IEEE International Frequency Control Symposium (FCS)*, pp.1-4, May 2012.
- [86] C. Hayashi, "Subharmonic oscillations in nonlinear systems, " *J. Applied Physics*, vol. 24, no. 5, pp. 521-529, May 1953.
- [87] J.J. Gagnepain, M. Oliver, F.L. Walls, "Excess Noise in Quartz Crystal Resonators," *37<sup>th</sup> Annual Symposium on Frequency Control*, pp. 218- 225, 1983.
- [88] M. Shahmohammadi, D. Dikbas, B. P. Harrington, and R. Abdolvand. "Passive tuning in lateral-mode thin-film piezoelectric oscillators," *Frequency Control and the European Frequency and Time Forum*, pp. 1-5, May 2011.
- [89] R. M. Langdon, "Resonator sensors-a review," *J. Physics E: Scientific Instruments*, vol. 18,

---

no.2, 1985.

[90] D. Stevens, J. C. Andle, S. Sabah, S. J. Jumani, B. W.A. Wall, M. Baier, T. Martens, and R. Gruenwald; "Applications of wireless temperature measurement using saw resonators," *Acoustic Wave Devices for Future Mobile Communications Systems Symp.*, 2010.

[91] L. Reindl, G. Scholl, T. Ostertag, H. Scherr, U. Wolff, and F. Schmidt; "Theory and application of passive SAW radio transponders as sensors," *Trans. Ultrasonics, Ferroelectrics, and Frequency Control*, vol. 45, no. 5, pp. 1281-1292, 1998.

[92] X. Q. Bao, W. Burkhard, V. V. Varadan, and V. K. Varadan; "SAW Temperature Sensor and Remote Reading System," *IEEE Ultrasonics Symp.*, pp.583-586, Oct. 1987.

[93] W. Buff, F. Plath, O. Schmeckeber, M. Rusko, T. Vandahl, H. Luck, F. Moller, and D. C. Malocha; "Remote sensor system using passive SAW sensors," *Ultrasonics Symp.*, pp.585-588, 1994.

[94] V. Kalinin, G. Bown, and A. Leigh; "Contactless Torque and Temperature Sensor Based on SAW Resonators," *Ultrasonics Symp.*, pp.1490-1493, 2006.

[95] Z. Xiangwen, W. Fei-Yue, and L. Li; "Optimal selection of piezoelectric substrates and crystal cuts for SAW-based pressure and temperature sensors," *Ultrasonics, Ferroelectrics, and Frequency Control*, vol.54, no.6, pp.1207-1216, June 2007.

[96] T. Ueda, K. Fusao, T. Iino, and D. Yamazaki; "Temperature Sensor Using Quartz Tuning Fork Resonator," *Frequency Control Symp.*, pp. 224-229, May 1986.

[97] C. M. Jha, G. Bahl, R. Melamud, S. A. Chandorkar, M. A. Hopcroft, B. Kim, M. Agarwal, J. Salvia, H. Mehta, and T. W. Kenny; "Cmos-Compatible Dual-Resonator MEMS Temperature Sensor with Milli-Degree Accuracy," *Solid-State Sensors, Actuators and Microsystems Conf.*,

---

pp.229-232, June 2007.

[98] F. J. Azcondo, and J. Peire; "Quartz crystal oscillator used as temperature sensor," *Industrial Electronics, Control and Instrumentation (IECON)*, pp.2580-2585 vol.3, Oct. 1991.

[ 99 ] T. M. Reeder and D. E. Cullen; "Surface-acoustic-wave pressure and temperature sensors," *Proceedings of the IEEE* , vol.64, no.5, pp.754-756, May 1976

[100] S. D. Senturia; "*Microsystem design*," vol. 3. Boston: Kluwer academic publishers, 2001.

[101] C. A. Balanis; "*Antenna theory: analysis and design*," John Wiley & Sons, 2012.

[102] Asadnia, M.; Kottapalli, A.G.P.; Shen, Z.; Miao, J.M.; Barbastathis, G.; Triantafyllou, M.S., "Flexible, zero powered, piezoelectric MEMS pressure sensor arrays for fish-like passive underwater sensing in marine vehicles," *IEEE Micro Electro Mechanical Systems (MEMS)*, pp. 126-129, Jan. 2013.

[103] Z. Wang, J. Miao, and W. Zhu; "Micromachined ultrasonic transducers and arrays based on piezoelectric thick film," *Applied Physics A*, vol. 91, no. 1, P. 107, 2008.

[104] Tsutomu Sato *et al.*, "Fabrication of Silicon-on-Nothing Structure by Substrate Engineering Using the Empty-Space-in-Silicon Formation Technique," *Japanese Journal of Applied Physics*, vol.43 12, Jan. 2004.